DEVELOPMENT OF ION MOBILITY-MASS SPECTROMETRY INSTRUMENTATION TO PROBE THE CONFORMATIONS AND CAPTURE THE SOLUTION TO GAS PHASE TRANSITION OF ELECTROSPRAYED BIOMOLECULES

A Dissertation

by

JOSHUA ADAM SILVEIRA

Submitted to the Office of Graduate and Professional Studies of
Texas A&M University
in partial fulfillment of the requirements for the degree of

DOCTOR OF PHILOSOPHY

Chair of Committee,	David H. Russell
Committee Members,	Emile A. Schweikert
	James D. Batteas
	Siegfried M. Musser
Head of Department,	David H. Russell

December 2013

Major Subject: Chemistry

ABSTRACT

Recent progress has been made developing ion mobility-mass spectrometry (IM-MS) instruments for biophysical studies; however, experimental techniques that can probe the structure and/or dynamics of biomolecules at intermediate extents of hydration are limited and little is known about the final stages of desolvation during electrospray ionization (ESI). Here, ion optical devices, analytical methodology, and instrument platforms are developed to study the conformations of structurally labile biomolecules (*i.e.*, peptides and proteins) produced upon ESI and provide new insight into their solution to gas phase evolution.

First, fundamental principles of periodic focusing ion mobility spectrometry are comprehensively discussed. Radial ion confinement is attributed to a collisionally dampened effective potential that ultimately results in high ion transmission. Detailed equations of motion are derived that culminate into useful methodology for accurate determination of peptide and protein collision cross section values via inclusion of a mobility dampening coefficient.

Second, evaporation of water from extensively hydrated protons and peptides formed by ESI is examined for the first time using a new cryogenic (80 K) IM-MS instrument platform. Key parameters that influence the cluster distributions are critically examined. In agreement with previous studies, the findings indicate that water evaporation is largely dependent upon the particular charge-carrying species within the cluster. IM-MS results for protonated water clusters suggest that the special stability of

the well-known $H^+(H_2O)_n$ (n = 21) "magic number" cluster is attributed to the presence of a compact clathrate cage isomer produced upon ESI. Peptide studies are also presented in which specific and nonspecific solvation is observed for gramicidin S [GS + 2H]$^{2+}$ $(H_2O)_n$ (n = 0 to ~26) and bradykinin [BK + 2H]$^{2+}$ $(H_2O)_n$ (n = 0 to ~73), respectively. However in the case of substance P, [SP + 3H]$^{3+}$, the results demonstrate that a compact dehydrated conformer population (resulting from the evaporative ESI process) can be kinetically trapped on the time scale of several milliseconds, even when an extended coil conformation is energetically favorable in the gas phase.

DEDICATION

for Franchesca

ACKNOWLEDGEMENTS

I would first like to thank my graduate research advisor, Professor David Russell for his guidance and support throughout the course of this research. Thank you to my entire research group, and those who I have worked with closely over the past five years (Dr. Chaminda Gamage, Kyle Fort, Junho Jeon, Ryan Blase, and Kelly Servage).

Thank you also to Dr. Jody May who designed and characterized the original variable temperature drift tube that I later modified and used in the evaporative studies described herein. Though we overlapped only briefly at Texas A&M, I learned an immense amount from Jody's graduate work.

I especially appreciate those who made this work possible including the Texas A&M machine shop staff (Will Seward, Carl Johnson, and Ron Page) and the LBMS electronics technician (Greg Matthijetz); I am also grateful for the financial support from The National Science Foundation—Major Research Instrumentation Program (DBI-0821700), the Department of Energy, Division of Chemical Sciences, (BES DE-FG02-04ER15520), and the Robert A. Welch Foundation (A-1176).

Thank you to my parents (Donna and Brian), grandparents (John, Lucille, and Rosalin), sister (Jordanne), close family (Rose Marie and Jane), and friends (too many to list here) for their love, support, and encouragement over the years. Lastly, thank you to my wife (Franchesca) for her endless love and patience through our memorable years spent in College Station.

NOMENCLATURE

ATD	arrival time distribution
BK	bradykinin
CID	collision-induced dissociation
DC	direct current
DC IG	direct current ion guide
CRM	charge residue model
ESI	electrospray ionization
GEMMA	gas-phase electrophoretic mobility molecular analyzer
GS	gramicidin S
HPLC	high performance liquid chromatography
IEM	ion evaporation model
IIMS	inverse ion mobility spectrometry
IM	ion mobility
IM-MS	ion mobility-mass spectrometry
IMS	ion mobility spectrometry
MS	mass spectrometry
FAIMS	high-field asymmetric waveform ion mobility spectrometry (also termed differential mobility spectrometry)
OMS	overtone mobility spectrometry
PA	proton affinity

PF IMS	periodic focusing ion mobility spectrometry
SP	substance P
TDC	time-to-digital converter
TIMS	trapped ion mobility spectrometry
TOF	time-of-flight
TW IMS	travelling wave ion mobility spectrometry
RF	radio frequency
RF IF	radio frequency ion funnel
UF IMS	uniform field ion mobility spectrometry
a	acceleration
a_r	radial acceleration
a_z	axial acceleration
D	diffusion coefficient
d	electrode inner diameter
F	force
$F_{Electric}$	force on the ion due to the electric field
$F_{Friction}$	force on the ion due to collisions with the neutral buffer gas
F_r	radial force
F_z	axial force
E	electric field
E_c	central or net electric field
E_{max}	maximum periodic focusing electric field

E_{min}	minimum periodic focusing electric field
$E_{0,r}$	radial electric field amplitude
$E_{0,z}$	axial electric field amplitude
E_z	axial electric field
$E_z(\vec{z})$	axial profile of the axial electric field
$E_z(\vec{r})$	radial profile of the axial electric field
E_r	radial electric field
$E_r(\vec{z})$	axial profile of the radial electric field
$E_r(\vec{r})$	radial profile of the radial electric field
E_x	x-component of the electric field in the Cartesian coordinate system
E_y	y-component of the electric field in the Cartesian coordinate system
E_z	z-component of the electric field in the Cartesian coordinate system
e	elementary charge ($1.602 \cdot 10^{-19}$ C)
K	ion mobility coefficient
K_0	reduced mobility coefficient
k_B	Boltzmann's constant ($1.381 \cdot 10^{-23}$ J $\cdot$ K^{-1})
L	axial length of drift tube
m	mass
M	mass of neutral
N	gas number density
N_0	gas number density at STP ($2.687 \cdot 10^{25}$ m^{-3})
n_z	number of ion-neutral collisions per unit $\vec{z}$-dimension

P	pressure
P_0	standard pressure (760 Torr)
p	momentum
q	charge of ion
R	resolving power
r	radial displacement
$\vec{r}$	radial direction
r_i	initial $\vec{r}$-position
$r_{v,i}$	initial $\vec{r}$-displacement in vacuum
s	electrode spacing
T	temperature
T_{eff}	effective ion temperature
T_0	standard temperature (273.15 K)
t	time
t_0	time spent by an ion outside the drift tube
t_d	drift time
Δt_d	full width of the drift time peak at half maximum height
V	voltage
$V_{p\text{-}p}$	peak-to-peak RF voltage
V^*	effective potential or pseudopotential
v	velocity
v_d	drift velocity

$v_{r,v}$	radial velocity in vacuum
$v_{r,v,i}$	initial radial velocity in vacuum
v_z	axial velocity
w	electrode width
z	charge state
$\vec{z}$	axial direction
α	mobility damping factor for PF IMS
β	a term that accounts for the ion-neutral interaction potential
ξ	a dimensionless term to account for the ion's fractional energy loss due to inelastic collisions
Ω	ion-neutral collision cross section
Ω_{He}	ion-helium collision cross section
Ω_{RF}	RF frequency
Ω_{eff}	effective RF frequency
μ	reduced mass
λ	wavelength
Δ	slope

TABLE OF CONTENTS

LIST OF FIGURES

LIST OF TABLES

Page

1. ION MOBILITY AND MASS SPECTROMETRY

1.1 Overview

Ion mobility spectrometry (IMS) involves the electrophoretic transport of gas-phase ions through a neutral buffer gas. Introduced as *plasma chromatography ca.* 1970, IMS was originally considered to have drift times that compared to chromatographic retention times. The association unfortunately hindered the progress of IMS as an analytical technique, as the peak capacity of IMS simply could not match that of high performance liquid chromatography (HPLC), and the resolution could not match that of mass spectrometry (MS). In the past few decades, interest in IMS has renewed as a variety of instrument modifications coupling IMS to MS have improved the resolution and versatility resulting in suitability for a wide range of biological and chemical applications. For example, several variations of the original uniform field IMS (UF IMS) technique have been developed including traveling wave IMS (TW IMS), periodic focusing IMS (PF IMS), high-field asymmetric IMS (FAIMS), overtone mobility spectrometry (OMS), trapped IMS (TIMS), inverse IMS (IIMS), and the gas-phase electrophoretic mobility molecular analyzer (GEMMA)—all of which have been coupled to MS. Together, ion mobility-mass spectrometry (IM-MS) affords several attractive analytical attributes including rapid (μs–ms) separations of complex mixtures, isobars, and isomers, reduction of chemical noise, and determination of ion size—all of which are difficult or impossible to achieve by IMS or MS alone. Moreover, IM-MS has the capability of differentiating ions belonging to chemical classes (*i.e.* carbohydrates,

lipids, nucleotides, peptides, and proteins) and charge states (*i.e.*, z = 1+, 2+, 3+…) along distinctive mobility-mass trendlines.[1-3] Although a relatively old technique, the aforementioned characteristics have allowed IMS and particularly, IM-MS to emerge as a powerful analytical tool with a broad range of applications including the study of atmospheric ions,[4] aerosol particles,[5] and ion cluster geometries,[6-9] detection of airborne chemical agents,[10-11] separation of conformational mass isomers of small molecules,[12-14] assignment of ground and excited electronic states in transition metals,[15] and characterization of hydrocarbons in crude oils.[16-17] Additionally, the separation speed and information-rich data have allowed for biological applications aimed at investigating molecular structure[18-19] and/or carrying out high-throughput separations of complex mixtures in the fields of proteomics,[3,20] glycomics,[21-22] and metabolomics.[23]

Owing to the versatility of IM-MS, the study of novel instrument design platforms and applications continues to be one of the most rapidly growing areas in the field. Moreover, several research groups have focused on achieving high resolution (R > 50) IMS separations as this factor primarily limits overall IM-MS peak capacity and the information content that can be experimentally derived.[24-26] The resolution of the ion mobility measurement is defined as the ratio between the average drift time (t_d) and the full width of the mobility peak at half-maximum height (Δt_d). Theoretically, resolution is limited by several factors, although for a sufficiently small packet of ions, the dominant contribution is axial ($\vec{z}$) diffusional broadening in the drift tube. A practical definition of diffusion-limited IMS resolution is given by,[27]

$$\boldsymbol{R} = \frac{t_d}{\Delta t_d} = \frac{1}{4}\left(\frac{qLE}{k_B T \ln 2}\right)^{\frac{1}{2}} \quad (1)$$

where T is the temperature, q is the ion charge, k_B is Boltzmann's constant, L is the length of the drift tube, E is the electric field, and the product LE translates into the overall voltage drop, V, across the drift tube. Jarrold *et al.* reported among the highest measured mobility resolution to date, R = 172, for singly charged fullerene radical cations using 10,000 V applied across a 63 cm drift tube maintained at a pressure of 500 Torr[24] while Clemmer *et al.* more recently achieved R = 345 for doubly charged substance P ions using a pulsed cyclic drift tube design.[28]

1.2 Principles of Uniform Field Ion Mobility Spectrometry

1.2.1 The Low-field Limit

UF IMS is the fundamental basis for all other ion mobility techniques since the transport theory has been mathematically described and the electric field that ion *see* contains only an axial ($\vec{z}$) component. Ion mobility in UF IMS occurs as ions traverse a drift tube containing an inert buffer gas under the influence of a low uniform electric field. The force exerted on the ion by the electric field is opposed by the frictional forces created by ion-neutral collisions, resulting in an average velocity for the ion, termed the drift velocity (v_d), as shown in Figure 1.

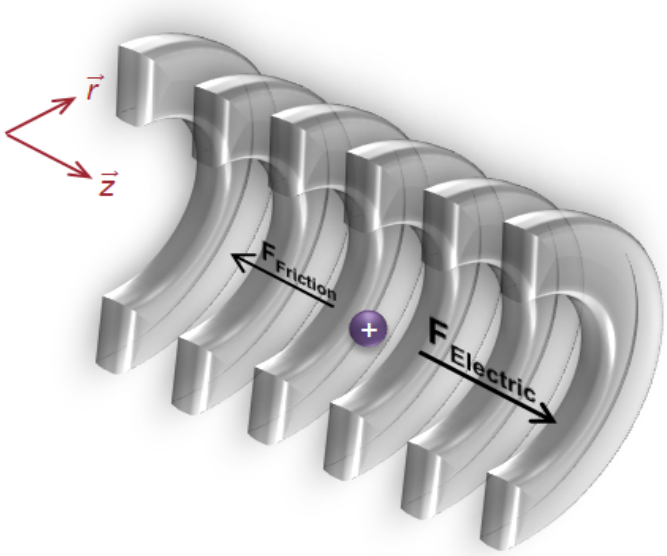

Figure 1. Forces exerted upon a representative singly charged cation (purple circle) in IMS. The force created by the electric field ($F_{Electric}$, (+) $\vec{\boldsymbol{z}}$-direction) is greater than the frictional forces ($F_{Friction}$, (-) $\vec{\boldsymbol{z}}$-direction) created by ion-neutral collisions resulting in net ion transport in the (+) $\vec{\boldsymbol{z}}$-direction. Below the low field limit, the magnitude of the drift velocity of the ion is comparable to the Maxwell-Boltzmann velocity distribution of the neutral gas resulting in ion trajectories that resemble directed diffusion.

The field strength is typically expressed in units of E/P having units of $V \cdot cm^{-1} \cdot Torr^{-1}$ or E/N measured in Townsend units ($1\ Td = 10^{-17}\ V \cdot cm^2$). The mobility constant (K) provides proportionality between the drift velocity and the electric field (E) and is given by,[29]

$$\boldsymbol{K = \frac{v_d}{E} = \frac{L}{t_d\, E}} \qquad (2)$$

where t_d is the drift time of the ion. K may also be expressed as the reduced ion mobility coefficient, K_0, obtained by standardizing K to standard temperature ($T_0 = 273.15$ K) and pressure ($P_0 = 760$ Torr),

$$\boldsymbol{K_0 = K\frac{P}{P_0}\frac{T_0}{T}} \quad (3)$$

where P is the drift gas pressure, and T is the drift gas temperature. Structural features may be deduced using the parameters K_0 and Ω expressed in the relationship,[29-30]

$$\boldsymbol{K_0 = \left(\frac{3q}{16N_0}\right)\left(\frac{2\pi}{\mu k_B T}\right)^{\frac{1}{2}}\left(\frac{1}{\Omega}\right)} \quad (4)$$

where,

$$\boldsymbol{\mu = \frac{mM}{m+M}} \quad (5).$$

The terms N_0, m, M, q, and μ represent the standard particle number density of the buffer gas, the mass of the ion, the mass of the buffer gas, the charge of the ion and the reduced mass, respectively. From eqs. (3), (4), and (5), Ω can be obtained from the expression,

$$\boldsymbol{\Omega = \left(\frac{3q}{16N_0}\right)\left(\frac{2\pi}{\mu k_B T}\right)^{\frac{1}{2}}\left(\frac{t_d E}{L}\right)\left(\frac{P_0 T}{P T_0}\right)} \quad (6).$$

It should be noted that eq. (6) is defined under conditions where the ion-neutral interaction potentials (*i.e.*, ion-induced dipole) and ion heating effects are assumed to be minimal. These assumptions are reasonable for typical operation of UF IMS devices with bath gasses of low polarizability at ambient temperature. Moreover, eq. (6) applies when the kinetic energy the ions gain in the electric field ($\frac{1}{2}mv_d^2$) is not significantly above the thermal energy (k_BT), defining a *low-field limit*.

1.2.2 Intermediate Electric Fields

Although it is generally assumed that IMS is carried out under the low-field limit, ions present in a drift tube can have a different temperature than the buffer gas owing to the electric field acting upon them.[29] The effective ion temperature (T_{eff}) is described by,

$$\frac{3}{2}k_B T_{eff} = \frac{3}{2}k_B T + \frac{1}{2}M v_d^2 (1 + \beta) \quad (7)$$

where β is a small correction term related to the interaction potential. When ions are molecular, rather than atomic, eq. (7) must be modified to account for inelastic collisions and anisotropic interaction potentials,[31]

$$\frac{3}{2}k_B T'_{eff} = \left[1 + \frac{M}{m}\xi\right]^{-1}\left[\frac{3}{2}k_B T + \frac{1}{2}M v_d^2 (1 + \beta')\right] \quad (8).$$

In this case, β' is a new correction term of similar magnitude to β, ξ is a dimensionless ratio which represents the fractional energy loss due to inelastic collisions, and T'_{eff} is a new effective ion temperature. However, when E/N is sufficiently small, $\xi \rightarrow 0$ and eq. (8) reduces to eq. (7).

Ion heating becomes significant for IMS measurements of macromolecules at reduced pressures (0.1-1 Torr) as well as high electric fields. Under these conditions, $T_{eff} > T$ because the field contribution to the ion kinetic energy is nonzero. That is, the translational kinetic energy gained by a macromolecule from the electric field between subsequent collisions cannot be completely quenched by a single collision with the buffer gas which allows for partial conservation of momentum (see Figure 2(d)). At sufficiently low field strength, K remains independent of E/N defining an intermediate-

field region where eq. (6) still applies.[32-33] However, if T_{eff} becomes sufficiently high, labile analytes can undergo structural rearrangement. If the structural change results in a difference in Ω, the transition will be reflected in K.

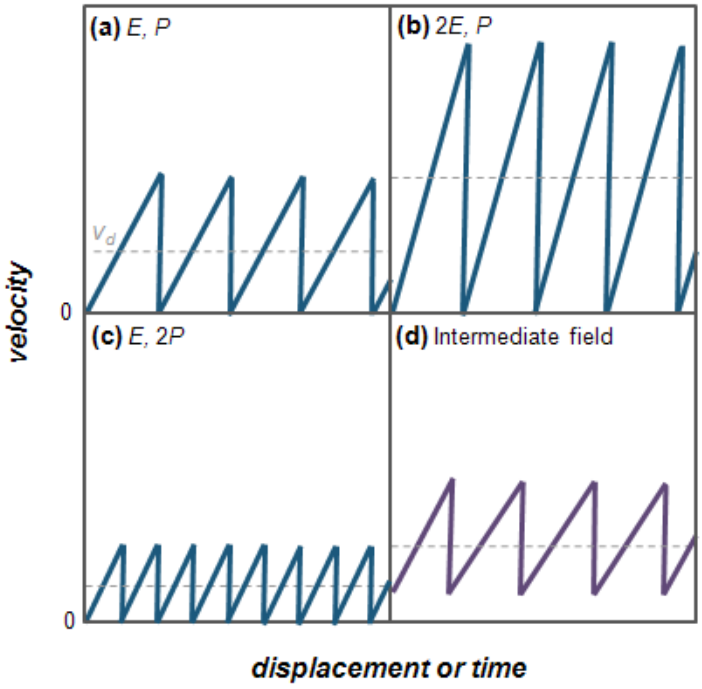

Figure 2. Microscopic ion velocity (solid blue trace) below the low field limit for a given E and P (a), $2E$ and P (b), and E and $2P$ (c). The drift velocity increases owing to the electric field acting upon the ion until subsequent collision with a neutral whereupon the ion velocity is completely quenched. In each case, the macroscopic drift velocity that is measured by IMS is represented by the dashed grey line. In the intermediate field (d), ion-neutral collisions do not completely quench the ion velocity (solid purple trace) allowing for partial momentum conservation—a critical outcome that forms the foundation for the theory derived in Sections 2-4.

1.2.3 Addressing the Limitations of the Uniform Field

Current IM-MS technology emerged from uniform field ion mobility spectrometry (UF IMS) measurements that employ a linear voltage gradient to facilitate

ion transport through a buffer gas. While fundamental gas phase ion transport is mathematically described for UF IMS[29,34-35] and measurement of analyte size (by eq. 6) is straightforward, radial ($\vec{r}$) diffusion poses significant limitations to the sensitivity (especially for ion mobility platforms coupled with MS) owing to the loss of radially-diffuse ions at conductance limiting apertures required for efficient integration of the relatively high pressure drift tube and the vacuum region of the mass analyzer.

Contemporary IM-MS instruments achieve high sensitivity by utilizing radial ion focusing devices. Although this strategy is effective, accurate determination of Ω requires additional consideration because ion transport contains additional modes—the extent of which depend entirely upon the specific technique employed and voltages applied. For example, the commercially available TW IMS (Synapt HD MS, G1 and G2, Waters Inc., Manchester, U.K.) superimposes RF voltage on the ring electrodes to radially confine ions during IMS analysis. TW IMS measurement also relies upon an electrodynamic potential waveform (T-wave) which traverses the drift tube to facilitate axial ion transport. While TW IMS has developed into a robust and sensitive method with an expanding user-base, TW IMS requires complex electronic design for the applied dynamic voltages that limit the overall drift length and subsequent IMS resolving power (typically $R \approx 40$). Moreover, determination of Ω by TW IMS deviates from the first-order UF IMS principles thereby demanding careful calibration methods because Ω is exponentially proportional to TW IMS drift time.[36] The calibration is further complicated by its dependency on the T-wave height, wave velocity, and the potential for significant ion heating inside the drift tube.[37] To obtain effective ion-helium

Ω values (Ω_{He}) using TW IMS, drift times measured in N_2 (g) are calibrated with ions whose Ω_{He} is known by UF IMS. Hence, a large effort in calibrating TW IMS measurements to yield Ω_{He} values remains the subject of current research for several groups because a robust method must account for all of the aforementioned variables. Giles *et al.* have demonstrated a relatively straightforward method for measurement of Ω_{He} in a TW IMS device, but these conditions do not yield optimal resolution and are only established for species with a single (or narrow) conformer distribution.[38]

Several other approaches have also been developed to improve dispersive IMS ion transport including the segmented quadrupole drift tube[39] and drift tube positioned in a strong magnetic field.[40] However, the most widely used approach involves the use of RF ion funnel (RF IF) region(s) in the middle and/or back of a UF IMS drift tube to compensate for radial diffusion. Schematically, the RF IF is a conical shaped ion guide that consists of a series of several closely spaced radially symmetric thin ring electrodes with an inner diameter that decreases in the axial dimension. Ions are focused in the *r*-dimension by an inhomogeneous RF field that contains a confining effective potential (or pseudopotential, *V**) barrier extending from the electrode edges while ions propagate in the $\vec{z}$-direction owing to the superimposed DC potential drop across the device. Although this approach is effective, Gillig *et al*. demonstrated an even simpler means for improving ion transmission by maintaining the inner diameter (*d*), width (*w*), and spacing (*s*) of UF IMS electrodes ~6 mm. These modifications altered the shape of the electric field and resulted in ion confinement along the central drift axis ($\vec{r} = 0$) without the use of electrodynamic voltages.[41-42] The new design yielded ion transmission

properties far superior to UF IMS, and the resolving power has exceeded >100 by simply increasing the length of the drift tube without affecting ion transmission.[42-43] Fundamental characterization of the new device, termed a periodic focusing ion mobility spectrometer, is the major focus of Sections 2 through 4.

2. PERIODIC FOCUSING ION MOBILITY SPECTROMETRY: AXIAL DRIFT AND EFFECTIVE RF MOTION*

2.1 General Features

PF IMS incorporates two major modifications to the UF IMS ring electrode geometry (shown in Figure 3) to achieve radial confinement of ions during the IMS separation: (1) a decrease in the inner diameter and (2) an increase in the width of the lens element with respect to the electrode spacing, while a linear axial voltage drop is maintained across the electrode stack.[42,44] The novel geometry takes advantage of the fringing electric fields created near the edges of thick electrodes that generate the periodic focusing phenomenon. As a result, PF IMS operates in the low pressure regime between 1-10 Torr to produce rapid IMS separations on the μs-ms timescale and allow for utilization of kHz electronic pulsing and/or various multiplexing strategies for ion injection into the drift tube.[45-46] Under these conditions, the signal-to-noise is greatly enhanced and the duty cycle of the IM-MS instrument can approach unity.

---

* Part of this chapter is reprinted with permission from "Gas-Phase Ion Dynamics in a Periodic-Focusing DC Ion Guide" by Joshua A. Silveira, Chaminda M. Gamage, Ryan C. Blase, and David H. Russell, 2010. Int. J. Mass Spectrom., 296, 36-42, Copyright [2010] by Elsevier and "Gas-Phase Ion Dynamics in a Periodic-Focusing DC Ion Guide (Part II): Discrete Transport Modes" by Chaminda M. Gamage, Joshua A. Silveira, Ryan C. Blase, and David H. Russell, 2011. Int. J. Mass Spectrom., 303, 154-163, Copyright [2010] by Elsevier.

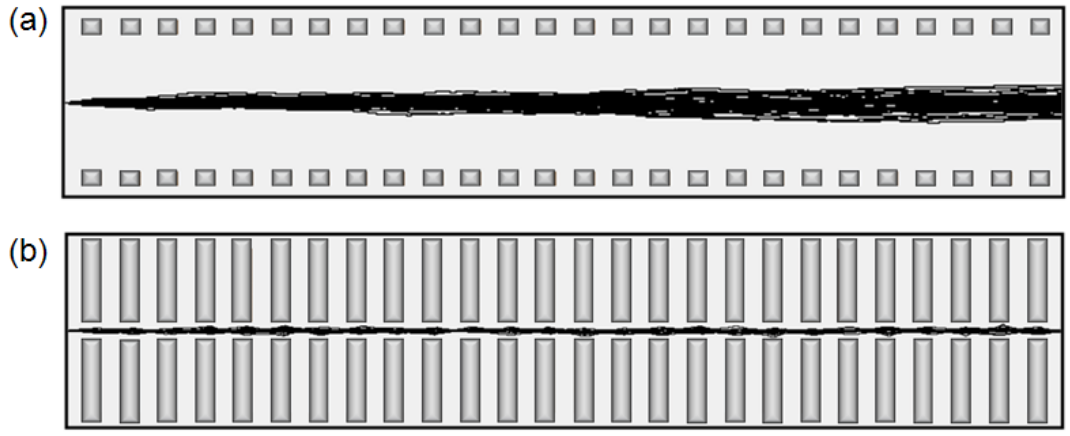

Figure 3. Longitudinal cross-sections of 32 cm UF (a) and PF (b) IMS drift tubes showing ion trajectories (flying left to right) in black. Ion transmission is increased in the PF IMS *via* the periodic focusing mechanism which confines ions near the central drift axis and maximizes ion transport through the exit of the drift tube.

2.2 Mathematical Description of the Effective RF

Figure 4 contains a schematic representation of two lens elements in PF IMS, including labels of the geometric variables and the cylindrical coordinate system referred to in this discussion.

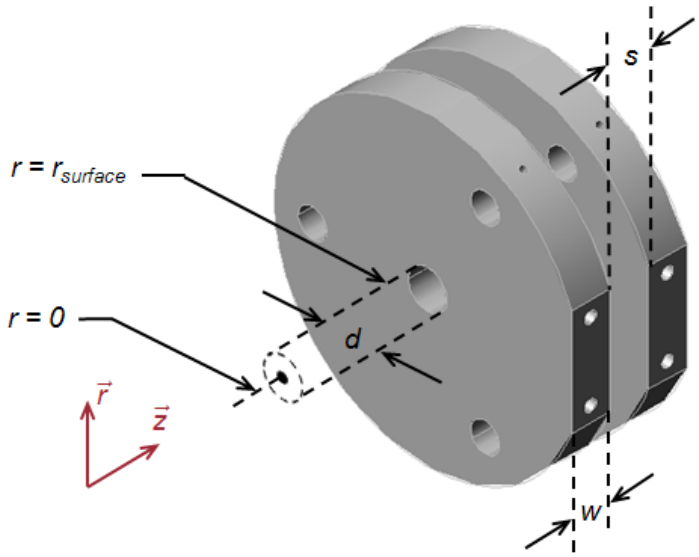

Figure 4. Two adjacent PF IMS electrodes showing the variables that define the aspect ratio (*s*:*w*:*d*) and the radial ($\vec{r}$) and axial ($\vec{z}$) dimensions. The location of electric field boundary conditions, $r = 0$ and $r = r_{surface}$, are also indicated.

In this section, a PF IMS design with an aspect ratio having s = 6 mm and w = 6 mm is considered for description of the electric fields as sinusoidal functions. This treatment is optimum at an $\vec{r}$-position < 0.25d where ions typically reside under stable operating conditions. Figure 5 shows the spatial oscillations along the $\vec{z}$-dimension for the axial electric field ($E_z(\vec{z})$) and radial electric field ($E_r(\vec{z})$) at discrete $\vec{r}$-positions for a single electrode subunit. It is important to note that $\left|E_z(\vec{z})\right|$ oscillations are dominant compared to $\left|E_r(\vec{z})\right|$–especially at small $\vec{r}$ values.

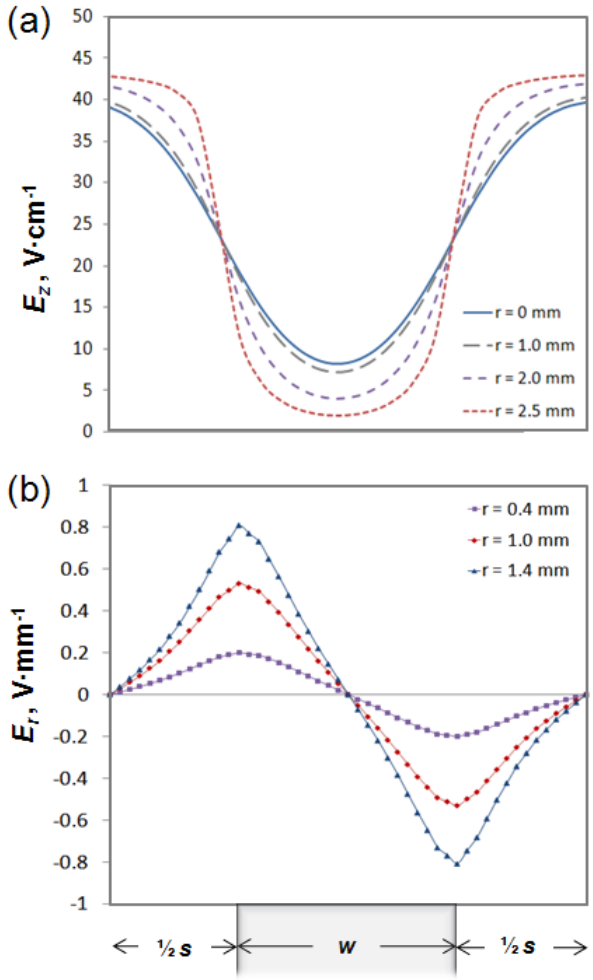

Figure 5. Electric fields as a function of the $\vec{z}$-dimension in a PF IMS drift tube: (a) axial electric field oscillations at varied $\vec{r}$-position and (b) radial electric field oscillations at varied $\vec{r}$-position shown for one electrode subunit. E_z directs axial ion drift while E_r generates an effective RF in the inertial frame for an ion with a given axial velocity. Analogous to RF devices, $|\boldsymbol{E_r}|$ increases as $\vec{r}$-position increases as illustrated in (b).

It is initially assumed that v_z is constant as changes in this variable will be considered later. For these parameters, $E_z(\vec{z})$ at constant $\vec{r}$ may be described by the time-dependent expression,

$$\boldsymbol{E_z(z) = E_{0,z} \cos\left(\Omega_{eff} t\right) + E_c} \qquad (9)$$

where $E_{0,z}$ is the axial electric field amplitude, Ω_{eff} is the effective RF frequency, and E_c is the central electric field. Similarly, E_r ($\vec{z}$) is 90° out-of-phase from the E_z ($\vec{z}$) waveform and may be approximated by the smooth curve given by,

$$\boldsymbol{E_r(z) = E_{0,r} \sin\left(\Omega_{eff} t\right)} \quad (10)$$

for variable radial positions with changing radial electric field amplitude, $E_{0,r}$. For the waveforms described by eq. (9) and (10), the wavelength (λ) is equivalent to,

$$\boldsymbol{\lambda = w + s} \quad (11)$$

Moreover, the effective RF is given by,

$$\boldsymbol{\Omega_{eff} = \frac{2\pi v_z}{\lambda}} \quad (12)$$

in radians.[47-48] The average effective RF ($\overline{\Omega}_{eff}$) may be calculated considering the ions depicted in Figure 3. At E/N = 75 Td the average axial ion velocity for $C_{60}^{+\bullet}$ in He is $\bar{v}_z$ ≈ 0.83 mm·μs^{-1} corresponding to an average drift time of 380 μs over a 32 cm drift length. For 26 electrodes of dimensions s = w = 6 mm (λ = 12 mm), $\overline{\Omega}_{eff}$ = 68 kHz. Thus, although not intuitively obvious, ions in PF IMS experience an effective RF with an average frequency in the kHz range comparable to conventional RF multipole ion guides and traps![49]

2.3 Equations of Radial Ion Motion

The radial electric force, F_r, generating the radial ripple can be derived considering a system with constant amplitude $E_{0,r}$ (fixed $\vec{r}$-position), and constant axial velocity ($\bar{v}_z$). Vacuum conditions are initially assumed since this is defined as one

boundary condition to describe the radial ion motion. Considering the harmonic field changes as a function in time,

$$\boldsymbol{F_r = ma_r = qE_r = q\,E_{0,r}\,\sin\left(\Omega_{eff}t\right)} \tag{13}$$

where a_r is the radial acceleration of the ion. Rearranging eq. (13) and substituting eq. (12), the radial acceleration of the ion becomes,

$$\boldsymbol{a_r = \frac{q}{m}E_{0,r}\,sin\left(\frac{2\pi v_z}{\lambda}t\right)} \tag{14}$$

Under vacuum conditions, the radial velocity component ($v_{r,v}$) due to the effective RF motion can be obtained by integrating eq. (14) with respect to *t* yielding,

$$\boldsymbol{V_{r,v} = -\frac{q}{m}E_{0,r}\left(\frac{\lambda}{2\pi v_z}\right)cos\left(\frac{2\pi v_z}{\lambda}t\right) + v_{r,v,i}} \tag{15}$$

where $v_{r,v,i}$ is the initial radial velocity in vacuum. Accordingly, displacement in the $\vec{r}$-direction for vacuum conditions is obtained *via* integration of eq. (15) with respect to *t* yielding,

$$\boldsymbol{r_v = -\frac{q}{m}E_{0,r}\left(\frac{\lambda}{2\pi v_z}\right)^2 sin\left(\frac{2\pi v_z}{\lambda}t\right) + v_{r,v,i}t + r_{v,i}} \tag{16}$$

where $r_{v,i}$ is the initial $\vec{r}$-displacement.

However, since stable operating conditions of PF IMS require the presence of collisional cooling, low-field IMS theory must also be considered. In this case, macroscopic radial drift is induced by microscopic collision events such that the radial velocity component is reset to $v_r = 0$ following each ion-neutral collision.[33] In this case, if a constant electric field is present, the net velocity (or drift velocity) that arises from the microscale events is constant while changes in the magnitude of the drift velocity are directly proportional to the changes in the magnitude of the electric field. Furthermore,

the drift velocity and electric field vectors are in the same direction for a positively charged ion. Mathematically, for the sinusoidally changing acceleration caused by the force of the electric field in eq. (13), the radial velocity (v_r) profile in the low-field collisional regime may be obtained by the drift velocity as,

$$\boldsymbol{v_r = KE_{0,r}\, sin\frac{2\pi v_z}{\lambda}t} \tag{17}$$

where K is the ion mobility coefficient. By integrating eq. (17) with respect to t, the radial displacement (r) can be obtained,

$$\boldsymbol{r = -KE_{0,r}\frac{\lambda}{2\pi v_z}cos\frac{2\pi v_z}{\lambda}t + r_i} \tag{18}$$

where r_i is the initial $\vec{r}$-position. It is important to note that eq. (18) describes the effective RF motion in the presence of ion-neutral collisions assuming constant $E_{0,r}$ and v_z. However, as $\vec{r}$-position increases, $E_{0,r}$ increases as shown in Figure 5. As $\vec{z}$-position increases, v_z oscillates according to E_z and the number of collisions experienced per unit z-dimension (n_z).[48] Each effect induces changes in both the amplitude and the frequency of the motion described by eq. (18). The amplitude changes may be considered symmetric in the (+) and (-) $\vec{r}$-segments of the radial ripple motion while the frequency changes are not observed in the final ion trajectory traces since they are displayed in the space domain with fixed λ.

More importantly, eq. (18) assumes that ion kinetic energy is reset to zero following subsequent collision events. In other words, the radial momentum of the ion is completely damped during the collisions. However, under stable operating conditions, ions in PF IMS maintain a fraction of their initial radial momentum after a collision

event with a neutral gas molecule which is consistent with IMS in an intermediate field. Thus, the results of the previous derivation, (eq. (16) and eq. (18)), represent the two boundary conditions for PF IMS and are depicted in Figure 6 (left panel). The inclusion of K in eq. (18) indicates that the amplitude of radial motion has a dependence on mobility and may contribute to defining a low-mobility limit for PF IMS.

During stable operation of PF IMS, maximum radial displacement (corresponding to the ion turnaround point) is dependent upon E/N, depicted by the simulations shown in Figure 6 (right panel) for several conditions obtained by varied pressure. Note that the left panel of Figure 6 shows boundary-condition ion motions in the upper half of PF IMS while the simulations in the right panel shows ion trajectories in the bottom half (inverted across the $\vec{r} = 0$ plane with respect to the former). Figure 6 shows that at higher E/N, ion turnaround point resembles the vacuum expression given by eq. (16) which predicts that the ion turnaround point occurs at the tailing edge of the electrode (plotted in Figure 6, left panel). Conversely, at lower E/N, the ion turnaround point occurs near the midpoint of the electrode, which is predicted by eq. (18). Thus, the simulations contained in the right panel of Figure 6 are in agreement with the concept that the radial ion motion predicted by eqs. (16) and (18) represent the two boundary conditions where the radial momentum of the ion is conserved (eq. (16)) and completely damped (eq. (18)).

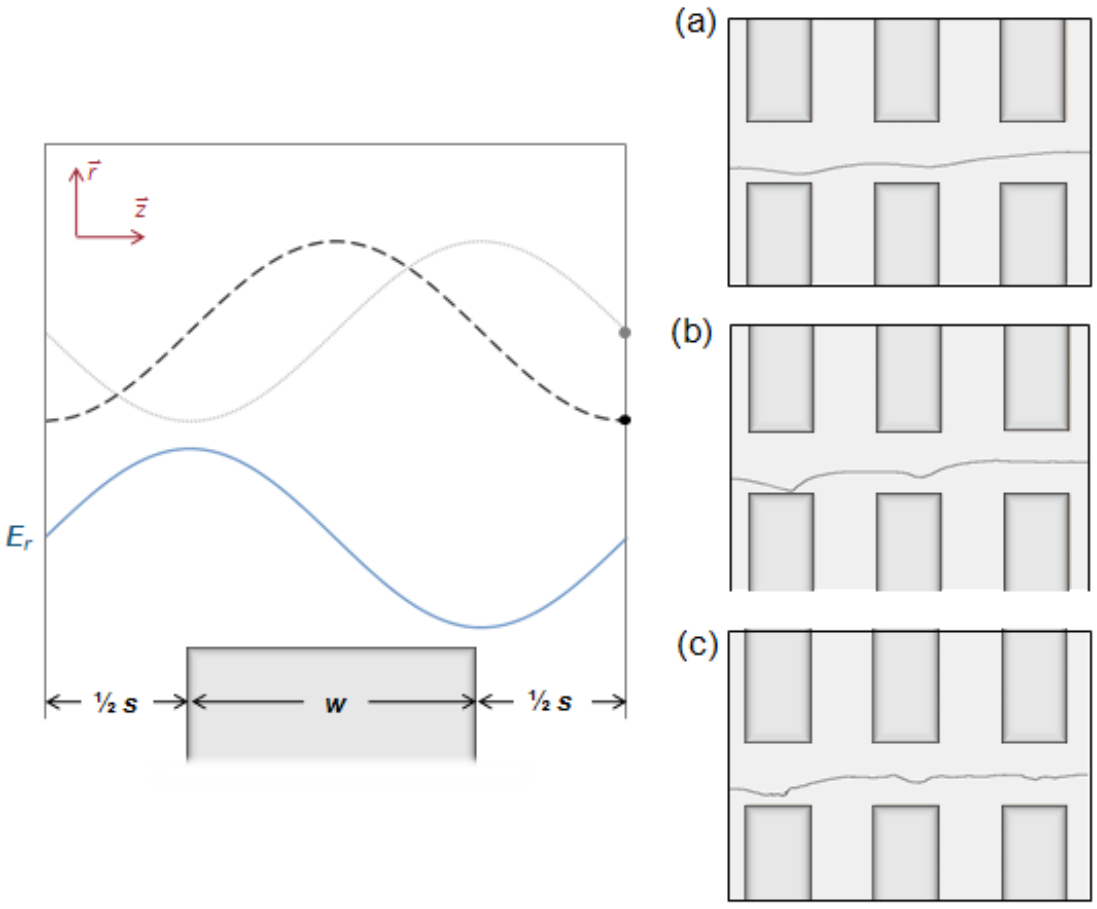

Figure 6. Left panel: Ion motion in the radial direction for vacuum (dotted grey line) and in the presence of thermalizing collisions (dashed black line) for one periodic focusing subunit as predicted by eq. (16) and eq. (18), respectively, for the static radial electric field represented below by the solid blue line. Motion due to initial radial velocity is neglected for the trajectory shown for vacuum conditions. The maximum ion displacement in the $\vec{r}$-dimension is shifted in phase by 90° between collisional and non-collisional boundary regimes. Right panel: Simulation of an ion trajectory starting at $\vec{r}$ = 1.5 mm at E_c/N 150 (a), 75 (b), and 37 (c) Td. In each case, three discrete transport modes are present. In each ease, maximum $\vec{r}$-displacement occurs between the midpoint inside of electrodes and the tailing electrode edge. As predicted by theory, the ion turnaround point shifts toward the midpoint of the electrodes at lower E/N values.

2.4 Axial Ion Transport (Ion Mobility)

Ion mobility in PF IMS is affected by two different phenomena: (1) periodic changes in the electric field and (2) periodic changes in n_z initiated by the electric field variations.[48] In this section, ion mobility separation in a periodic focusing electric field is discussed while the effect of n_z is addressed in Section 4.

It is important to realize that a potential drop across thick periodic focusing electrodes of aspect ratio *s*:*w*:*d* gives rise to a non-linear axial electric field. In this section, only the variations in the axial electric field in the axial direction ($E_z(\vec{z})$) and radial direction ($E_z(\vec{r})$) are considered. Let us also consider PF IMS designs with two different aspect ratios: PF $IMS_{1:1:1}$ ($s = w = d = 6$ mm) and PF $IMS_{3:3:4}$ ($s = w = 6$ mm, $d = 8$ mm). Figure 7(a) contains plots of ($E_z(\vec{z})$) at $\vec{r} = 0$ for both geometries normalized to the PF $IMS_{1:1:1}$. For each lens configuration $E_z(\vec{z})$ closely approximates a sinusoidal function. Thus, as ions traverse the device in the $\vec{z}$-direction at a constant $\vec{r}$-position, the electric field oscillates about a central electric field, E_c, where the amplitude of the sinusoidal function is denoted as E_0. The maximum $E_z(\vec{z})$ at $\vec{r} = 0$ (equivalent to $E_c + E_0$) is located at the midpoint between adjacent electrodes whereas the minimum $E_z(\vec{z})$ (equivalent to $E_c - E_0$) is located at the mid-point inside electrodes. The value of E_c may be obtained from,

$$\boldsymbol{E_c = \frac{1}{2}(E_{max} + E_{min})} \tag{19}$$

Figure 5(a) shows that in the (+) $\vec{r}$-direction, the shape of $E_z(\vec{z})$ deviates from the sinusoidal waveform observed at $\vec{r} = 0$, while the spatial periodicity (λ) and phase of the electric field remain constant. At the electrode inner surface ($r_{surface}$) $E_z(\vec{z})$ may be

approximated by a square wave, although variations are observed near the electrode inner edges. For the approximated $E_z(\vec{z})$ square waveform at $r_{surface}$, the maximum value is located in the gap between adjacent electrodes, which approximates the maximum electric field that exists between the walls of two adjacent electrodes beyond the central orifice ($r > r_{surface}$). However, for the approximated $E_z(\vec{z})$ square waveform at $r_{surface}$, the minimum value is located on the inner electrode surface and is always zero. These outcomes imply that $r_{surface}$ contains the boundary conditions for E_{max} and E_{min} values. Figure 5(a) also demonstrates that in the (+) $\vec{r}$-direction, E_{min} shifts toward the minimum boundary condition more rapidly than E_{max} shifts toward the maximum boundary condition. Mathematically, this outcome may be stated,

$$\left|\frac{d(E_{max})}{dr}\right| < \left|\frac{d(E_{min})}{dr}\right| \tag{20}$$

which is a consequence of the fact that while the boundary condition for E_{max} is determined only by the voltage difference between adjacent electrodes of spacing s, the boundary condition for E_{min} is always fixed at zero. As a result of eq. (20), E_c, decreases in the (+) $\vec{r}$-direction as reflected in Figure 7(b) for PF $IMS_{1:1:1}$ and PF $IMS_{3:3:4}$ configurations. The importance of $E_c(\vec{r})$ is considered in the following section in the context of diffusion-limited IMS expressions.

Nevertheless, in any IMS separation, if the required low or intermediate field conditions[29] are maintained, the changes in the electric field do not change K since the drift time in eq. (2) is inversely proportional to E. For PF IMS, the position-varying electric field conditions may also be represented by a net electric field ($\bar{E}$) obtained by integrating over the periodic axial electric field profile. That is, for a fixed $\vec{r}$-position, the

axial mobility separation can be described by replacing E in eqs. (2) and (6) with $\bar{E}$. In order to derive an expression for $\bar{E}$, let us consider an ion traveling in the (+) $\vec{z}$-direction at the $\vec{r}$ = 0 position. The spatial periodicity (wavelength) of the axial electric field is given by λ in eq. (11). The spatial variation of the axial electric field may be described by,

$$\boldsymbol{E_z(z) = E_0 \cos(\omega_z z) + E_c} \tag{21}$$

where,

$$\boldsymbol{\omega_z = \frac{2\pi}{\lambda}} \tag{22}$$

such that,

$$\boldsymbol{E_z(z) = E_0 cos\left(\frac{2\pi z}{\lambda}\right) + E_c} \tag{23}.$$

Owing to the periodicity of the $E_z(\vec{z})$ waveform, the net electric field resulting at $\vec{r}$ = 0 can be obtained by integrating over one wavelength,

$$\boldsymbol{\bar{E} = \int_0^{2\pi} \left[E_0 cos\left(\frac{2\pi z}{\lambda}\right) + E_c\right] dz} \tag{24}$$

yielding,

$$\boldsymbol{\bar{E} = E_c} \tag{25}.$$

Thus, for ions traveling in the (+) z-direction at constant $\vec{r}$-position, the net electric field that contributes to the overall mobility separation is identical to a uniform electric field with the magnitude E_c. In this case, the mobility coefficient and the resolving power in PF IMS are explained by eqs. (2) and (1) with E substituted by E_c as follows,

$$\boldsymbol{K_{PF\ IMS} = \frac{L}{t_d E_c}} \tag{26}$$

$$\boldsymbol{R_{PF\ IMS}} = \frac{\boldsymbol{t_d}}{\boldsymbol{\Delta t_d}} = \frac{\mathbf{1}}{\mathbf{4}}\left(\frac{\boldsymbol{qLE_c}}{\boldsymbol{K_B T \ln 2}}\right)^{\frac{\mathbf{1}}{\mathbf{2}}} \quad (27).$$

Eqs. (26) and (27) approximate the mobility coefficient and the diffusion-limited resolution for ions traveling along the $\vec{z}$-dimension at $\vec{r}$ = 0 position in PF IMS. However, ions traversing in the drift tube sample different radial positions (owing to radial ripple motion and diffusion) although they are periodically refocused toward the *r* = 0 position (by *V**). Hence, Section 4 considers more rigorous treatment of ion mobility in PF IMS for accurate determination of collision cross sections. Ion optics simulations[43,48] suggest that ions at initial $r \neq 0$ positions are focused to the $r = 0$ position after traversing a few electrodes (~1-4, depending on the initial ion position, *E*/*N,* and *w*:*s*:*d*), and that overall ion migration to $\vec{r}$-positions exceeding half the value of the radius ($r = 0.25d$) is extremely rare. For, both electrode configurations, at $r < 0.25d$, the deviation in E_c from E_c (r = 0) is minimal (< 2%), as shown in Figure 7(b). Thus, assuming E_c ($r < 0.25d$) ≈ E_c (r = 0), eqs. (26) and (27) can still provide a practical estimate of the overall theoretical (diffusion-limited) *K* and *R* in PF IMS. Moreover, Figure 7(b) shows that as *d* is increased, E_c (r = 0) increases which is accompanied by a decrease in the amplitude of the E_c waveform shown in Figure 7(a). In this case, the resulting electric field near the central $\vec{z}$-axis exhibits fewer $\vec{r}$ and $\vec{z}$ variation which ultimately increases the measurement resolution as observed in the experimental data discussed below. Finally, as *d* becomes sufficiently large, the electric field near the $\vec{z}$-axis approaches a uniform electric field with the magnitude of the applied electric field, *E*, as in UF IMS. In other words, for large *d* values, the amplitude term of the $E_z(\vec{z})$ at r

= 0 waveform approaches zero while E_c approaches E. Therefore, as d is increased, the resolving power of the IMS measurement increases; however, as detailed in references[48] the ion transmission through the device will decrease. Moreover, R in PF IMS can be increased without affecting ion transmission by simply increasing L while keeping the applied electric field constant according to eq. (27) and the data presented in references [43,50]. Thus, PF IMS not yields high ion transmission, but also provides high resolution gas phase separations that are based on first-order IMS principles.

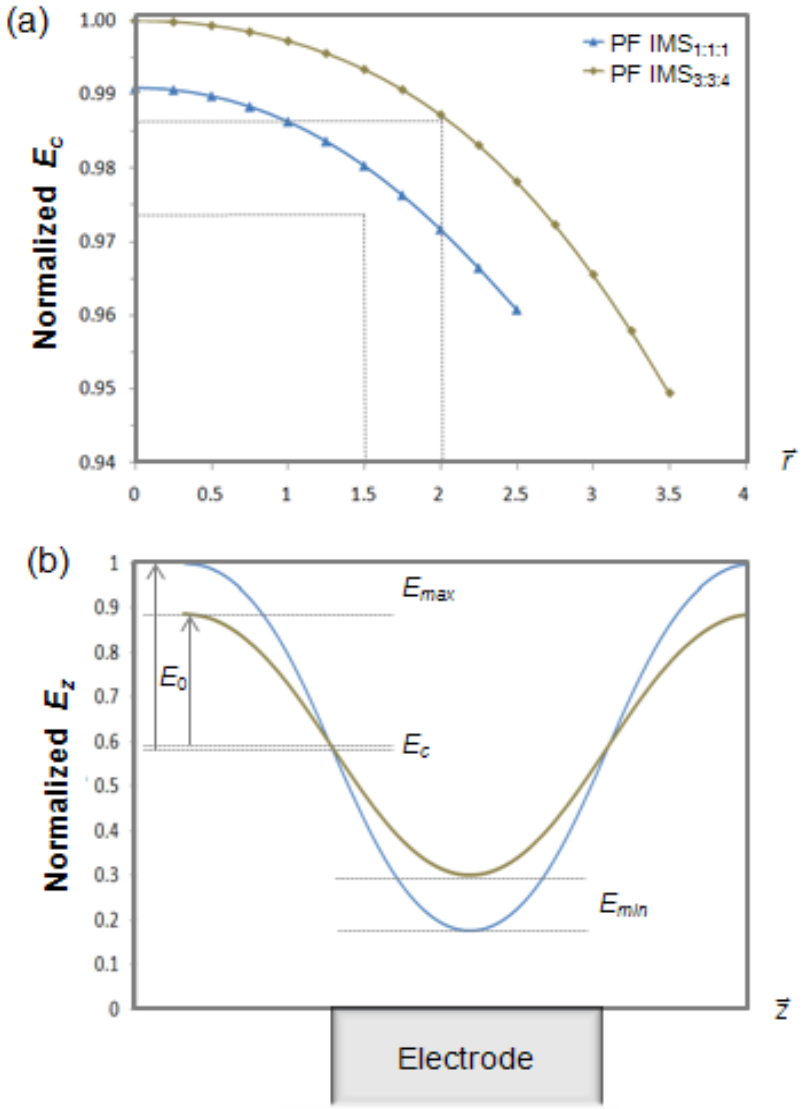

Figure 7. (a) Central electric field as a function of $\vec{r}$-position shown for both PF IMS$_{1:1:1}$ (blue ▲) and PF IMS$_{3:3:4}$ (tan ♦) geometries. Data is shown normalized to the PF IMS$_{3:3:4}$ E_c ($\vec{r}$ = 0) curve. The vertical dotted lines denote the *r*-position at half-radius ($\vec{r}$ = 0.25*d*) for both electrode configurations. In each case, E_c ($\vec{r}$ = 0.25*d*) corresponds to a < 2% decrease from E_c ($\vec{r}$ = 0) as indicated by the horizontal dotted lines. (b) Axial electric field at the $\vec{r}$ = 0 position for the PF IMS$_{1:1:1}$ (blue) and PF IMS$_{3:3:4}$ (tan) electrode configurations. The electric field is shown with respect to electrode position and normalized to the maximum value.

3. PERIODIC FOCUSING ION MOBILITY SPECTROMETRY: CENTRAL DRIFT MOTION AND THE EFFECTIVE POTENTIAL MODEL*

3.1 General Features

In contrast to uniform field IMS, PF IMS contains radial focusing properties analogous to the effective potentials found in a DC ion guide (DC IG) described by Guan and Marshall.[47] The effective potential concept, however, was originally derived to explain radial confinement of gas-phase ions moving relatively slowly (or at rest) with respect to an inhomogeneous RF (a time-varying waveform) electric field.[51] The effective potential (V^*) of a multipole ion guide with an applied RF voltage is described by the relationship,

$$\boldsymbol{V^* = \frac{q^2 E_0(\vec{r})^2}{4m(\Omega_{RF})^2}} \tag{28}$$

where $E_0(\vec{r})$ is the amplitude of the instantaneous electric field in the radial direction and Ω is the frequency of the applied RF voltage. While V^* is well established for a number of electrodynamic devices including RF ion guides and quadrupole ion traps[51], and RF ion funnels,[52] an analogous effect is achieved for an ion moving across alternating high and low electrostatic fields, as in the DC IG. In the DC IG, ions are radially focused as

---

* Part of this chapter is reprinted with permission from "Gas-Phase Ion Dynamics in a Periodic-Focusing DC Ion Guide" by Joshua A. Silveira, Chaminda M. Gamage, Ryan C. Blase, and David H. Russell, 2010. Int. J. Mass Spectrom., 296, 36-42, Copyright [2010] by Elsevier and "Gas-Phase Ion Dynamics in a Periodic-Focusing DC Ion Guide (Part II): Discrete transport Modes" by Chaminda M. Gamage, Joshua A. Silveira, Ryan C. Blase, and David H. Russell, 2011. Int. J. Mass Spectrom., 303, 154-163, Copyright [2010] by Elsevier.

they traverse thin electrodes that are alternately biased at positive and negative DC potentials. The electrostatic potentials create an effective RF potential (a position-varying waveform) in the inertial frame for an ion traveling with a given axial velocity, v_z. In a position-varying waveform, ion motion tracks with the effective RF frequency, that is dependent upon the axial velocity of the ion and the spatial periodicity of the axial electric field, as depicted in Figure 8. Substituting eq. (12) into eq. (19) and using the actual radial electric field, $E(\vec{r})$, to represent the radial electric field amplitude yields,

$$\boldsymbol{V^*(\vec{r}) = \frac{q^2 E(\vec{r})^2 \lambda^2}{16\pi^2 m v_z^2}} \quad (29).$$

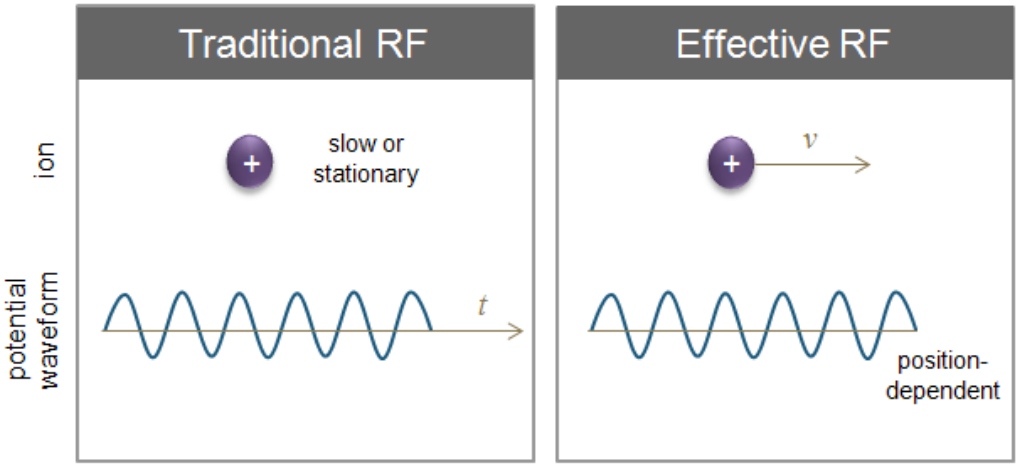

Figure 8. Schematic snapshot outlining the fundamental difference in ion dynamics for traditional and effective RF devices. In the case of traditional RF, slow ions encounter time-varying waveforms while in the case of an effective RF, fast ions sample static position-dependent waveforms. In both cases, ions experience an oscillatory force in the radial dimension, which gives rise to ion focusing.

Similarly, the axial voltage and electric field variations for a DC IG at a fixed $\vec{r}$-position are shown in Figure 9(b).[47] Although the electrostatic potentials are different in

the DC IG and PF IMS, both ultimately result in an oscillating electric field with a spatial periodicity that generates an effective RF for an ion moving with a given axial velocity. In the DC IG, two adjacent electrodes comprise a single effective RF spatial period (λ) while a single electrode and the spacing between the adjacent electrodes comprise one λ in PF IMS. Nevertheless, Ω_{eff} is remarkably similar as both devices operate in the kHz range. Moreover, the absence of a net electric field in the DC IG results in ion losses for ions without sufficient initial kinetic energy and for ions whose kinetic energy is quenched by thermalizing collisions. On the other hand, the net electric field in PF IMS oscillates about a central electric field (E_c) with an amplitude (E_0) as shown in Figure 9(a). Thus, initial ion kinetic energy is not critical in PF IMS, so long as it is not sufficiently high as to result in collision induced dissociation of labile macromolecules or structural rearrangement when determining Ω; instead, after equilibration, ion kinetic energy is governed by E/N as in conventional UF IMS. Simply stated, the presence of the net electric field in PF IMS allows for ion transport at elevated pressures and separation on the basis of Ω.

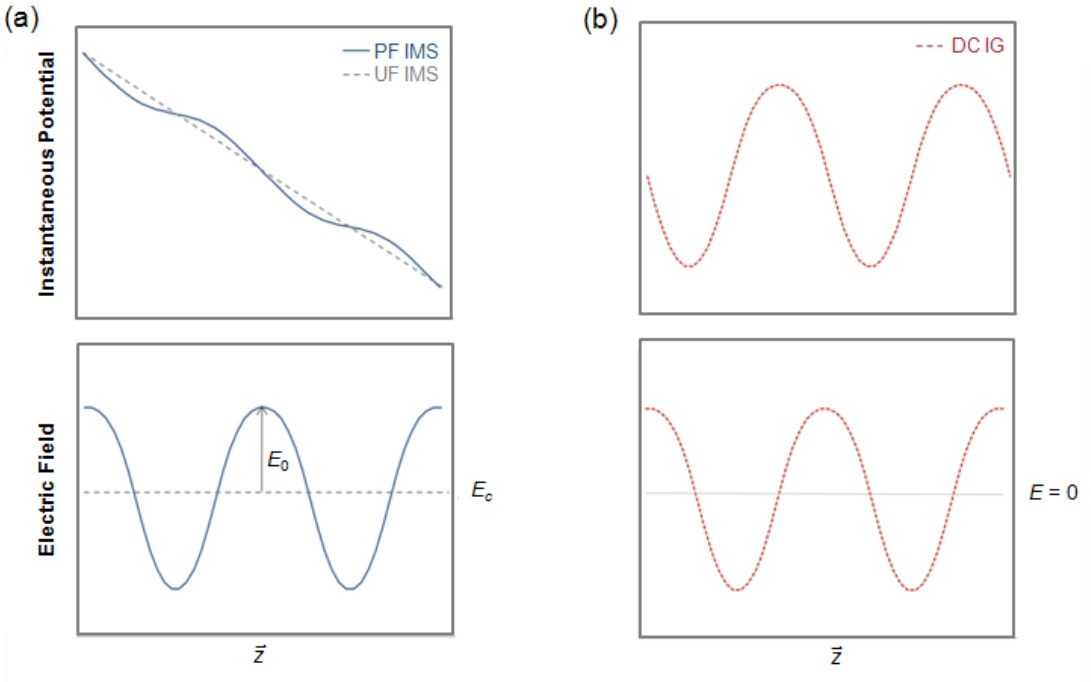

Figure 9. Axial variations of the instantaneous voltage and the electric field shown for PF IMS (solid blue lines) with respect to the uniform field (dashed grey lines) (a), and the DC IG (dotted red lines) (b) at fixed radial position. In both PF IMS and the DC IG, the axial voltage profile results in a sinusoidally oscillating electric field.

3.2 Determination of the Effective Potential

Analogous to the DC IG, the effective potentials in PF IMS are created by the radial variations in the electric field and are dependent upon the axial velocity of the ion. Here, the radial electric fields were determined using SIMION 8.0 (SIS, Ringoes, NJ). In SIMION, electrostatic potentials (and the electric fields) are determined by solving the Laplace equation in three dimensions,

$$\nabla^2 V = \nabla \cdot \boldsymbol{E} = \frac{\partial E_x}{\partial x} + \frac{\partial E_y}{\partial y} + \frac{\partial E_z}{\partial z} = \mathbf{0} \tag{30}$$

where the electric fields are described by Cartesian coordinates and the electrodes serve as the boundary conditions. It should be noted that the Laplace equation is not used to

treat space-charge effects that may contribute to electric field variations; in this work, the space-charge contributions are assumed to be minimal. Thus, to derive the effective potential profiles, a SIMION user program was used to calculate the radial variations in the electric field and measure the average axial ion velocity at 0.25 mm intervals along a periodic focusing drift tube (geometry: $s = w = d = 6$ mm). Since q, λ, and m are constants in eq. (20), the quotient, $E^2(r) / v_z^2$, is directly proportional to V^*. Although the axial ion velocity values derived represent a radial average, the standard deviation of these measurements was low ($\pm$ 0.07 mm·μs^{-1}). Thus, the radial variation of the axial velocity component is minimal.

The equipotential and effective potential contour profiles for a single electrode in PF IMS are depicted in Figure 10(a) and (b), respectively. When the axial ion velocity is considered constant, the effective potential contours appear symmetric.[53] The difference in axial velocity of the ions at the leading and tailing edge of the electrode contributes to the asymmetry of the effective potentials. That is, because ions are moving with relatively lower axial velocities as they approach the tailing edge of an electrode, the magnitude of the effective potential increases, as predicted by eq. (20). It is also important to note that the effective potentials, although asymmetric, are centered on the edges of each electrode and are relatively small in the regions where the radial electric field variations are minimal *viz.* the midpoints between and inside electrodes (see Figure 5(b)). The discontinuity in the effective potentials is a result of the thickness of the lens elements—since radial variations only occur near the electrode edges *via* fringing field effects—which has important consequences in terms of ion losses (discussed later in the

text, see Figure 11(b)). Furthermore, the effective potential profile at the edges of the electrode (without considering variations due to v_z) shows exponential decay with respect to radial position (V^* is proportional to e^r) as expected for V^* derived for a cylindrical potential profile.[47,51] It should be noted that an exponential decay profile contains larger space-charge capacity than RF multipole devices because it more closely approaches a particle in a box. That is, the radial field variations are minimal for ions on-axis while ions that deviate off-axis ($\vec{r} > 0$) are confined by a steep barrier. Because the radial V^* profile deviates from a cylindrical profile away from the electrode edges, the radial electric fields are more easily obtained using SIMION calculations as opposed to modification of analytical expressions derived for an ideal cylindrical potential profile.

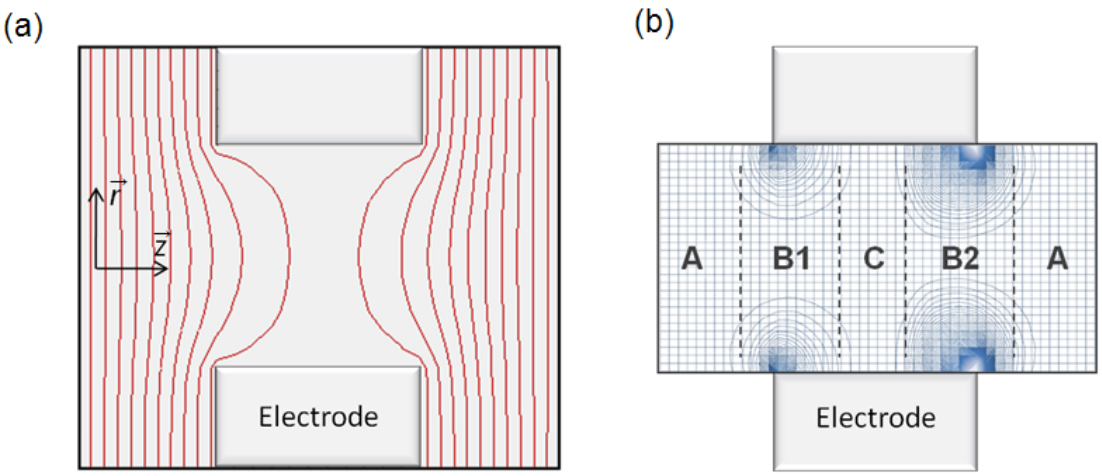

Figure 10. Equipotential lines shown in red (a) and contour plot of effective potentials shown in blue (b) projected from cylindrical coordinates onto the plane of the paper and plotted with respect to electrode position. The regions which are separated by dashed lines and labeled A-C are described in Section 3.3.

To qualitatively describe the ion dynamics in PF IMS, a subunit in the drift region has been divided into four sections labeled A, B1, C, and B2, as shown in Figure 10. In region A, the axial electric field is relatively high owing to the electrostatic potential drop from one electrode to the next. In this region, ion mobility occurs on the basis of a positionally dependent oscillating electric field where the amplitude of the axial profile of the electric field exceeds the central field ($E_c + E_0$). As ions enter an electrode (region B1) their velocity decreases as a result of the dampened electric field and ion-neutral collisions. In region C, the axial electric field amplitude defines an electric field lower than the central electric field ($E_c - E_0$), thus, ion velocities continue to decrease. It is important to note that region C does not contain strong effective potentials. Thus, if the electrode thickness is increased significantly, or if the overall applied electric field is decreased beyond a lower limit, region C approaches a field-free region where diffusion will dominate. For example, the overall average E/N is decreased from 75 to 37 Td in the simulation shown in Figure 11(b) to achieve low local field conditions in region C (E/N_{min}~12 Td V·cm^{-1}·torr^{-1}, corresponding to $E_c - E_0$), while still maintaining sufficiently high field strengths for mobility separation in region A (E/N_{max} ~62 Td, corresponding to $E_c + E_0$)**.** In this case, thermalization begins to dominate for ions in region C owing to very low acceleration from the local electric fields and increased collisional cooling, resulting in random diffusion behavior. Under these conditions some radially diffusing ions may not have sufficient axial kinetic energy to traverse region C and/or overcome the effective potential barrier extending from the back edge of the electrode. Thus, these ions are neutralized at the electrode surface as

illustrated by the ion denoted † in Figure 11(b). These results suggest that the electric field strength is critical in PF IMS due to the existence of low local electric fields inside the electrodes. However, as long as the applied E/N is sufficiently large (>~47 Td), the ion trajectory simulations suggest that PF IMS transmits nearly all ions (m/z = 720) across the device.

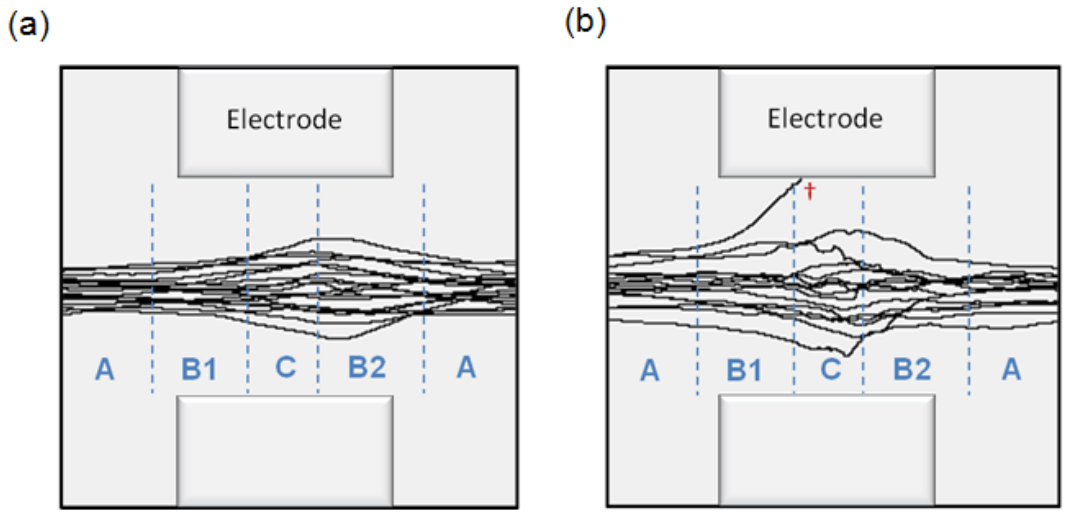

Figure 11. Ion trajectories showing periodic-focusing subunits at varied field strength: E_c/N 75 Td (a) and 37 Td (b). In (b), the radially-diffuse ion labeled † is thermalized owing to the locally dampened electric field in region C.

3.3 Theoretical Limits: Adiabaticity and Energy Conservation

Although the radial ripple motion is clear from Figure 6, slow central drift about $\vec{r}$ = 0 is slightly less obvious in a single periodic focusing subunit, though easily observed after several effective RF cycles. The central drift motion is attributed to effective potentials created by the electric field variations and collisional cooling. The theoretical basis for the estimation of effective potentials is provided by the presence of

fast (kHz) and continuous effective RF with increasing amplitude in the (+) $\vec{r}$-direction as shown in Figure 5(b).

The conservation of the radial momentum, at least to some extent, is vital for the effective potential concept. Let us first consider an undamped effective potential model as represented by eq. (20). While the mathematical treatment for the undamped effective potential model is well established, a qualitative physical description of the origin of effective potentials in PF IMS (considering no damping) may be presented contemplating the conserved momentum of a positively charged ion. Consider an ion initially residing at a certain $\vec{r}$-position and travelling in the $\vec{z}$-direction. During its $\vec{z}$ motion, the ion is subjected to different phases of the $E_r(\vec{z})$ waveforms, *i.e.* the ion *sees* an effective RF. When the phase is (+), the ion is subjected to a force in the (+) $\vec{r}$-direction (away from $\vec{r}$ = 0, (+) force), while the (-) phase applies a force in the (-) $\vec{r}$-direction (towards $\vec{r}$= 0, (-) force). Consider an ion moving in the (+) $\vec{r}$-direction under the influence of a (+) phase. Consequently, the ion is subjected to waveforms having higher amplitudes that impart progressively higher (+) force. After the ion reaches the $\vec{z}$ position where the waveforms switch to (-) phase, a (-) force is exerted on the ion. However, at the transition point, the ion has already acquired a momentum in the (+) $\vec{r}$-direction and thus the ion has to be decelerated by the (-) force before it turns around. Thus, a certain turnaround time results in the ion travelling an additional distance in (+) $\vec{r}$-direction from the time it is subjected to the waveform phase change. Let us term this extra displacement in the $\vec{r}$-direction the turnaround displacement. After turning around, the ion travels in the (-) $\vec{r}$-direction and is subjected to (-) phase waveforms that apply

progressively lower (-) force due to decreasing amplitudes. Subsequently, the ion reaches the $\vec{z}$-position where the waveforms change phase to (+) again, applying a (+) force on the ion. By this time, the ion has acquired momentum in the (-) $\vec{r}$-direction. However, unlike in the previous turnaround event, the waveforms have lower amplitudes and do not apply a force as high as the previous scenario prior to deceleration. This causes the ion to have a longer turnaround displacement in the (-) $\vec{r}$-direction than in the previous scenario. Due to this, the ion also displaces in the (-) $\vec{r}$-direction beyond the initial $\vec{r}$-position. Over several RF cycles, the net effect of this displacement is seen as an apparent drift towards the $r = 0$ position, which is suggested as the physical origin of the effective potentials herein.

Since the effective RF motion of the ions under stable operating parameters in PF IMS represents an intermediate situation between the completely conserved radial momentum (eq. (16)) and completely damped radial momentum (eq. (18)), the central drift motion may be explained using a damped effective potential model. To a first approximation, the damping of V^* with respect to eq. (20) may considered to be by a uniform factor throughout the device since the number density of the buffer gas, N, is uniform under constant static pressure conditions. In other words, although a finite portion of the ion radial momentum is damped, an undamped portion remains conserved, defining an adiabatic total energy. This may give rise to effective potentials damped by a factor with respect to the magnitudes predicted by eq. (20). According to this approximation, the relative magnitudes of the effective potential profiles remain the same as presented in reference [48] with relatively higher magnitudes towards the tailing

edge of the electrode as a result of the low axial ion velocities in that region. Accordingly, Figure 12 contains a flowchart of the proposed PF IMS focusing mechanism on the basis of a damped *V**. The bottom panel of Figure 12 contains a three dimensional profile of effective potentials that result in the radial ion confinement.

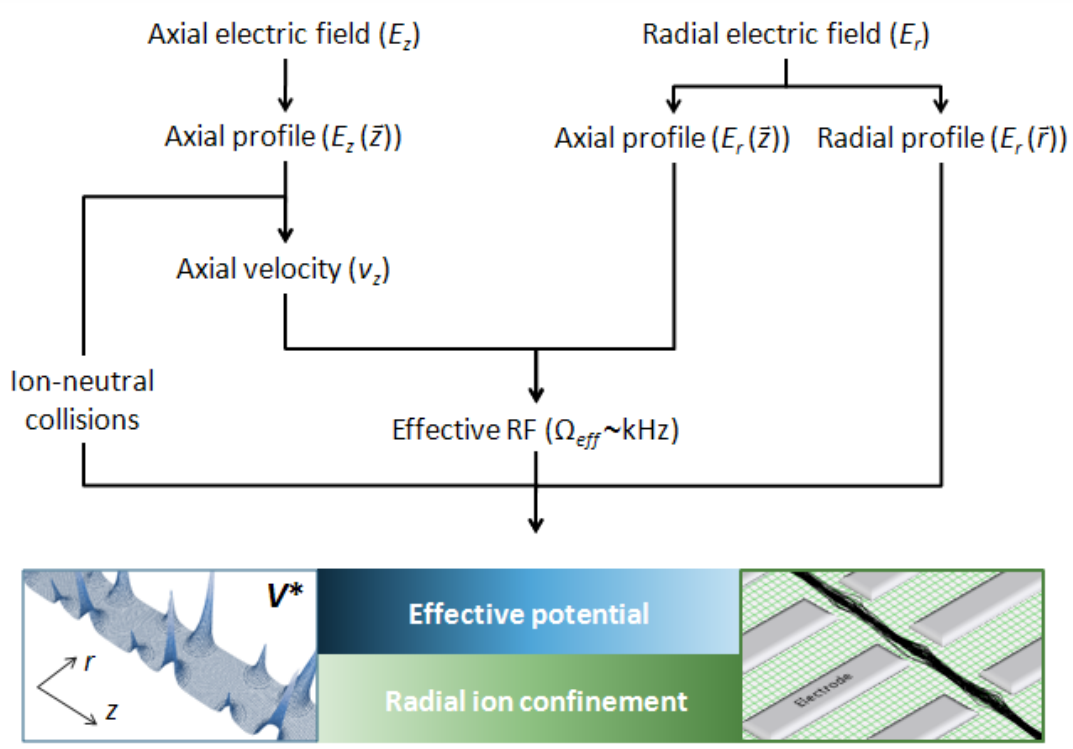

Figure 12. Flowchart diagram of the proposed radial focusing mechanism in PF IMS. See text for details.

Although the ion-neutral collisions damp the effective potentials, the presence of collisions is vital for the focusing mechanism to take effect. This is illustrated by the fact that the radial ripple and central drift motion are largely absent under vacuum conditions (simulation not shown) or dominant axial electric field conditions in the presence of

collisions *i.e.* the gap between adjacent electrodes. The latter is demonstrated by the fact that detailed motion due to the radial electric field is not observed in Figure 6 (right panel) near the leading and tailing edges of the electrodes and in the spacing between the electrodes because the axial electric field is dominant in these regions. Under these conditions, the ions are mainly influenced by the larger axial fields acquiring a relatively large v_z. In this case, ions do not spend sufficient time inside the electrodes to follow a well-defined radial ripple motion under the influence of the radial fields. More specifically, an increase in the axial ion velocity increases Ω_{eff} causing an instantaneous decrease in the amplitude of the radial ripple motion (eqs. (16) and (18). In the presence of collisions, ion momentum is dampened such that ion axial velocity decreases inside the electrodes and ion motion may be influenced by the relatively weak radial electric fields to follow the radial effective RF motion, giving rise to damped effective potentials. In other words, collisional damping is vital in radial focusing. Our simulations also indicated a low molecular weight inert gas such as He produces smoother effective RF trajectories in contrast to higher molecular weight gases such as nitrogen that cause scattering. This phenomenon is similar to the trapping of ions by means of smooth secular motion in a quadrupolar ion trap where the optimum performance in terms of resolution is obtained when He is used for collisional damping.[54]

It should be noted that the term $E_{0,r}(\vec{r})$ in eq. (20) is replaced with E_r when obtaining the V^* contours for PF IMS. Although the $E_r(\vec{z})$ waveforms can be considered as continuous sinusoidal functions, in this representation, the waveforms encountered by

the ion at each $\vec{z}$-position is considered to have different instantaneous amplitudes that are represented by E_r. This representation is adopted since unlike in traditional RF devices, V^* profiles are composed of a combination of multipole terms that are different for each $\vec{z}$-position. The exponentially decaying V^* ($\vec{r}$) profile expected for a thin ring electrode is observed only at the edges of the electrodes [48] while the fringing fields create different combinations of multipole V^* ($\vec{r}$) profiles at other $\vec{z}$-positions. These variations are linked to the $\vec{z}$-variations of the E_r ($\vec{r}$) profiles. The $1/\Omega_{eff}$ term signifies the amount of time the ion spends at each $\vec{z}$-position. For example, the middle of the electrode (region C, as denoted in Figure 11) contains very small E_r ($\vec{r}$) variations while the $1/\Omega_{eff}$ term is relatively large. These conditions create a region where the effective potentials are minimal or absent. We previously showed that for relatively low E/N conditions (<37 Td for C_{60} radial cations), ion losses may occur in the middle of each electrode, supporting the adopted V^* representation. In this region, V^* creates a potential well in the axial dimension (Figure 12, bottom panel) and ions without sufficient axial velocity may be lost towards the electrode walls by either diffusion or radial electric fields. Increasing w beyond a certain limit will convert this region to a field-free diffusing region. Similar potential wells have been reported by Giles *et al.* for a traveling wave ion mobility spectrometer (TW IMS) with an RF applied 180° out-of-phase to adjacent electrodes and a superimposed DC pulse that travels in the $\vec{z}$-dimension.[55]

The fast effective RF motion can be decoupled from the slower central drift motion as shown in the simulations, suggesting that the first order adiabatic

approximation[51] used in deriving these expressions may still be used for the estimation of V^*. Additionally, the fact that the magnitude of radial electric field variations during one effective RF cycle is small compared to the magnitude of the radial electric field provides justification for the use of an adiabatic approximation. However, the presence of collisional damping and the $\vec{z}$-dependence of the $V^*(\vec{r})$ profiles complicate a quantitative calculation or validation of the effective potentials for PF IMS. In other words, the use of adiabatic approximations to validate a V^* model damped with respect to eq. (20) or a model that incorporates the $\vec{z}$-dependence of $V^*(\vec{r})$ is beyond the scope of the current study. The model is presented in order to provide a semi-quantitative understanding of the effective potentials in PF IMS and an exact mathematical treatment of V^* is not intended.

4. PERIODIC FOCUSING ION MOBILITY SPECTROMETRY: DETERMINATION OF ION-NEUTRAL COLLISION CROSS SECTIONS*

4.1 Background

The basic principles of operation for the periodic focusing ion mobility spectrometer have been described in detail in Section 1 through 3. Functionally, PF IMS has three major ion transport modes: (1) axial drift, which gives rise to ion mobility, (2) *radial ripple* motion owing to the existence of an *effective RF*, and (3) *central drift* motion that causes the ions to be radially focused toward the central drift axis ($\vec{r}$= 0).[50,56] In principle, PF IMS is analogous to the RF-confining drift tube recently implemented into a Synapt G1 platform by Bush *et al.* for determination of Ω_{He} reference values for TW IMS calibration.[57] A major difference, however, is that RF voltages are not used in PF IMS, but ion transport through the PF IMS drift tube is identical to an inhomogeneous RF field. This outcome is achieved because PF IMS supplants the velocity of the ion in position-dependent DC electric fields for the time-dependent voltage utilized in RF devices. The result is that ions are confined by a collisionally-damped effective potential that arises from an effective RF experienced by relatively fast ions traversing electrostatic waveforms. These results demonstrated that ion mobility in PF IMS may be described by the same principles as UF IMS (even in the presence of

* Part of this chapter is reprinted with permission from "Damping Factor Links Periodic Focusing and Uniform Field Ion Mobility for Accurate Determination of Collision Cross Sections" by Joshua A. Silveira, Junho Jeon, Chaminda M. Gamage, Pei J. Pai, Kyle L. Fort, and David H. Russell, 2012. Anal. Chem., 84, 2818-2824, Copyright [2012] by The American Chemical Society.

position-dependent DC electric fields); however, the measured drift time in PF IMS is relatively longer owing to the radial ripple and the central drift motion that do not exist in UF IMS. Hence, we introduce a *mobility damping factor* (α) to account for the increase in drift time. In the current work, we present a quantitative treatment of α to develop the fundamental methodology for direct and accurate measurement of peptide and protein Ω values using PF IMS.

4.2 Experimental Methods

Bradykinin, angiotensin II, melittin, ubiquitin (bovine) and cytochrome c (equine) were purchased from Sigma-Aldrich (St. Louis, MO). ESI solutions were prepared at concentrations between ~5 - 50 μM in H_2O (0.01% formic acid) for ubiquitin and 50:50% CH_3OH:H_2O (0.1% formic acid) for all other compounds.

A detailed description of the home-built IM-MS instrumentation used in this study is found in reference.[58] Briefly, sample solutions were directly infused at 0.5 $\mu L \cdot min^{-1}$ from a pulled-tip nano-ESI emitter into a heated capillary maintained at 343 K with a ~2.5-3.0 kV potential drop. Ions are focused through a 2.0 mm aperture with a RF IF operating at 700 kHz and 75 V_{p-p} at a pressure ~0.75 Torr. The drift tube consists of a 58 cm periodic-focusing ion mobility spectrometer with an electrode width (*w*) and spacing (*s*) of 6.35 mm and an inner diameter (*d*) of 8 mm. Ions are pulsed into the drift tube maintained at 1.00 ± 0.01 Torr He (g) with a gating frequency of 200 Hz. The typical resolving power for a single conformer in the drift tube is ~50. Ions exiting the PF IMS drift tube are accelerated orthogonally into a time-of-flight (TOF) mass

spectrometer and detected by a dual microchannel plate detector. The mobility spectra were recorded by pulsed synchronization of the mobility gate and TOF extraction source using custom 2D acquisition software provided by Ionwerks (Houston, TX).

For each analyte, the arrival time distribution (ATD) was plotted against $1/V$ to determine the time spent outside the drift tube (t_0) that is subtracted from the ATD to yield the drift time (t_d). Data were recorded at 300 K ± 1K for three to five different drift voltages; a minimum of five measurements were collected at each voltage setting. Thus, each experimentally reported Ω value represents the average of fifteen to twenty five measurements.

The average drift times of peptide ions through 10 cm PF IMS ($s = w = 6.25$ mm, $d = 8$ mm) and UF IMS ($s = w = 6.25$ mm, $d = 42$ mm) drift tubes were calculated using the *collision_hs1.lua* program provided with SIMION 8.0. Ion-neutral collisional dynamics were simulated for elastic collisions between He (g) and peptide ions at 300 K. Theoretical α values were calculated by simulating ion trajectories for known analytes using Ω values measured by UF IMS.[59-60]

4.3 Transport Theory

Section 1 contains a detailed discussion of UF IMS theory. In PF IMS, the mobility damping coefficient (α) is introduced to account for the differences between the apparent mobility in PF IMS ($K_{PF\ IMS}$) and the mobility expected in a UF IMS ($K_{UF\ IMS} = K$), which is defined as,[56]

$$\boldsymbol{\alpha = \frac{K_{PF\ IMS}}{K_{UF\ IMS}} = \frac{K_{0,PF\ IMS}}{K_{0,UF\ IMS}}} \qquad (31)$$

Alternatively, α may also be derived from the respective slope (Δ) of the t_d vs. $1/V$ plot for UF IMS and PF IMS measurements (see Figure 13) given by,

$$\boldsymbol{\alpha} = \frac{\Delta_{UF\ IMS}}{\Delta_{PF\ IMS}} \tag{32}$$

In either case, eqs. (2) and (6) can be rewritten for PF IMS such that,[56]

$$\boldsymbol{K} = \frac{\boldsymbol{L}}{\boldsymbol{\alpha t_d\, E}} \tag{33}$$

and

$$\boldsymbol{\Omega} = \left(\frac{\boldsymbol{3q}}{\boldsymbol{16N_0}}\right)\left(\frac{\boldsymbol{2\pi}}{\boldsymbol{\mu k_B T}}\right)^{\frac{1}{2}}\left(\frac{\boldsymbol{\alpha t_d E}}{\boldsymbol{L}}\right)\left(\frac{\boldsymbol{P_0 T}}{\boldsymbol{P T_0}}\right) \tag{34}$$

The following discussion is focused upon validation of this theory from both a fundamental as well as an analytical perspective.

4.4 Quantitative Description of Ion Mobility

Figure 13(a) shows representative ion trajectories for UF IMS and PF IMS drift tubes, along with the coordinate system referred to in the discussion. Owing to radial ripple and central drift motion observed in PF IMS, drift times are longer than UF IMS measurements—all other parameters being equal. These differences can be seen in the drift time versus inverse voltage plot for bradykinin $[M + 2H]^{2+}$ obtained by SIMION simulation shown in Figure 13(b). In this approach, the ratio of slopes given by eq. (23) provides the quantitative theoretical α value of 0.79.

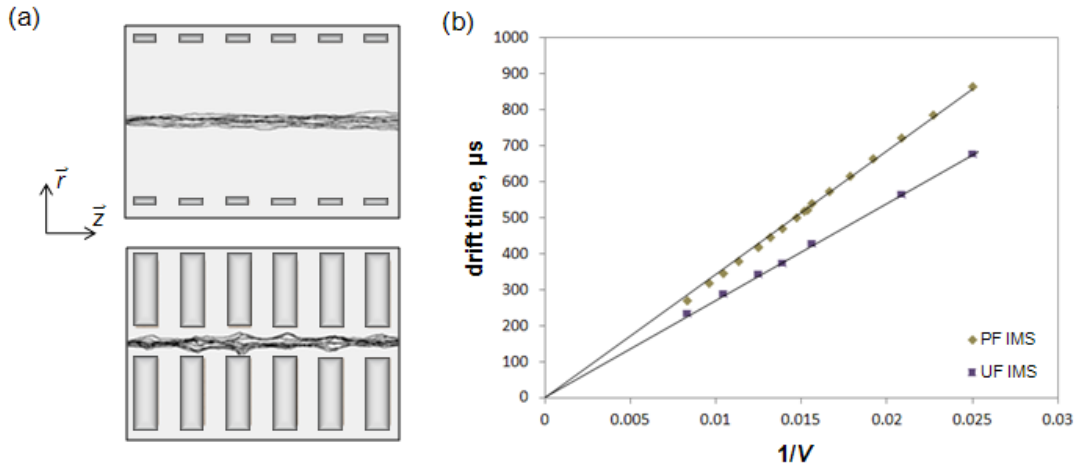

Figure 13. Representative bradykinin $[M + 2H]^{2+}$ (531.3 *m*/*z*, Ω = 242 Å^2, [60]) ion trajectories in UF IMS (a, top panel) and PF IMS (a, bottom panel) at 1.00 Torr and ambient temperature (300 K). In PF IMS, ions drift axially (as in UF IMS) but also undergo radial ripple and central drift motion that maintains ion trajectories near $\vec{r} = 0$. When the observed drift times over L = 10 cm are plotted as a function of $1/V$ (b), the apparent mobility of the ions in PF IMS is smaller by a factor of α, owing to the additional transport modes. The correlation coefficients are R^2 (UF IMS) = 0.99995 and R^2 (PF IMS) = 0.99768.

Note that the correlation coefficients for the linear trendlines are high, despite slight deviation at higher V where drift times were measured above the approximate low field limit described by,[34]

$$\frac{E}{N} < \left(\frac{m}{m+M}\right)^{\frac{1}{2}} \frac{d^2}{z} \qquad (35).$$

where d is the diameter of the ion approximating its Ω using a hard sphere. For bradykinin $[M + 2H]^{2+}$ of d = 8.74 Å,[29] the semi-quantitative expression predicts that the low field limit extends to values ≲ 38.1 Td (≲ 12.3 V·cm^{-1}·Torr^{-1}). However, optimal operation of PF IMS, requires intermediate fields where a fraction of the radial momentum is conserved thereby allowing for energy exchange among the modes of

transport.[51,56] The deviation observed from inclusion of intermediate field drift time measurements is small and only contributes to 1% error in the SIMION-based measurement (*viz.* $\alpha = 0.78$ when calculated using only data recorded ≤ 64 V).

The deviation is not observed experimentally because polyatomic ions have degrees of freedom that are unaccounted for in the hard sphere approximation utilized in eq. (11) and SIMION-based measurements. Figure 14(a) shows a representative ATD for bradykinin at 54.4 Td—the highest field strength utilized. Under the conditions employed, the bradykinin spectrum is dominated by the relatively broad $[M + 2H]^{2+}$ peak. Although FAIMS studies have shown evidence for six $[M + 2H]^{2+}$ conformations,[61] these results are consistent with UF IMS studies by Pierson *et al.*, which contain two partially resolved ATDs.[62] Figure 14(b) shows the experimental PF IMS ATD of bradykinin $[M + 2H]^{2+}$ plotted against $1/V$ in both the low and intermediate field regime (32.3 - 54.4 Td or 10.4 - 17.5 $V \cdot cm^{-1} \cdot Torr^{-1}$). The high correlation coefficient ($R^2_{PF\ IMS} = 0.9998$) confirms that the dependence of K upon E/N is for the field strengths employed is negligible, and low field IMS expressions may still be used to describe macroscopic ion drift.

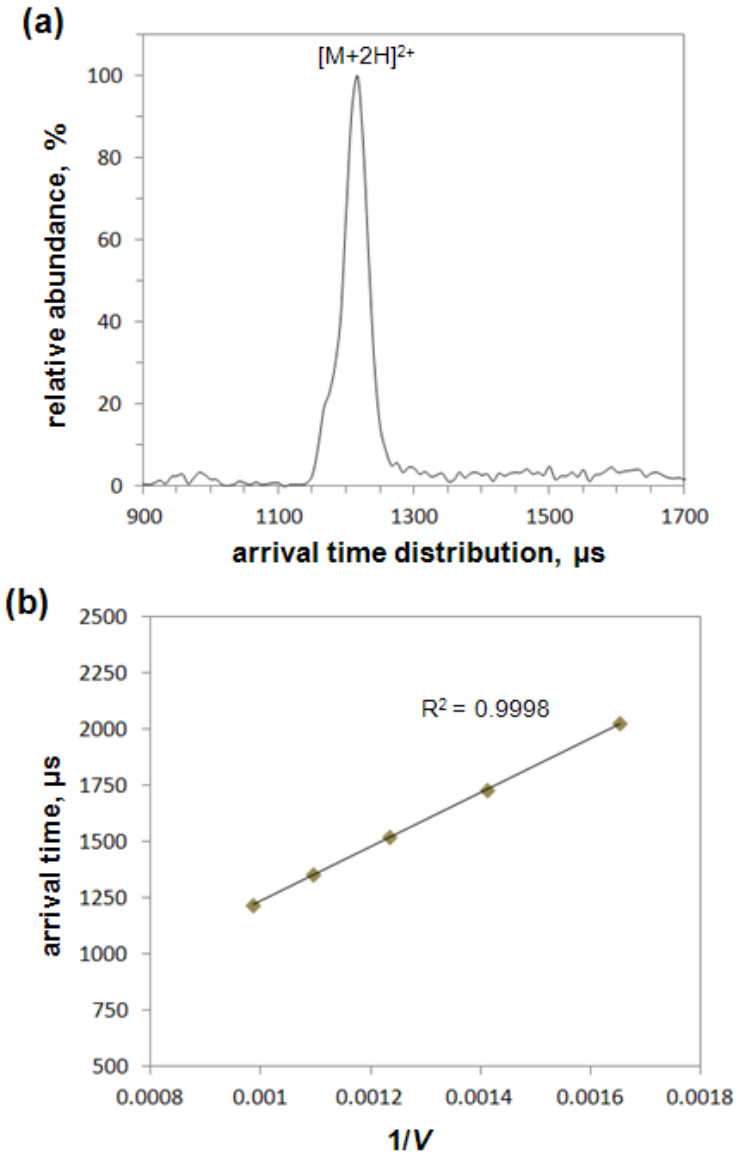

Figure 14. Arrival time distribution (a) and arrival time vs. 1/*V* plot (b) for bradykinin. The spectrum shown in (a) was collected at 54.4 Td (17.5 V · cm^{-1} · $Torr^{-1}$). In (b), the electric field strengths range from 10.4 - 17.5 V · cm^{-1} across the 58 cm PF IMS drift tube. The high correlation coefficient suggests that although experimental measurements are made in both low and intermediate field regimes according to eq. (26), the higher order tems are negligible and low field experssions may be used to describe ion drift observed in PF IMS for the field strengths employed. The data in (b) corresponds to the main peak centroid observed at longer arrival times.

4.5 Origins of α

Qualitatively, α is a measure of the extent to which the mobility in PF IMS deviates from UF IMS for equivalent operating conditions. It should be noted that the quantity α is defined under conditions where the ion-neutral interaction potentials and ion heating effects are assumed to be minimal. These assumptions are reasonable for typical operation of PF IMS devices with He (g) and ambient temperature. By definition, α is mathematically limited to values $0 \leq \alpha \leq 1$. For the case of $\alpha = 1$, PF IMS drift motion is identical to UF IMS—a theoretical boundary condition approached in Figure 13(b) where the trendlines converge at high *V*. For practical operating conditions in low and intermediate fields, $\alpha < 1$ as a result of mobility damping. The two main parameters that contribute to the existence of mobility damping have been introduced in our previous work[56]: (1) the increase in number of ion-neutral collisions per unit $\vec{z}$-displacement (n_z) and (2) the decrease in the applied net electric field (E_c) at larger $\vec{r}$-positions; however, the contribution of the later effect to the net electric field is $\lesssim$2% leaving variation in n_z as the dominant effect. Mobility damping is directly proportional to n_z and inversely proportional to α. Expressed mathematically, the end result yields,

$$\boldsymbol{\alpha} \approx \frac{\mathbf{1}/\boldsymbol{n_{z,PF\ IMS}}}{\mathbf{1}/\boldsymbol{n_{z,UF\ IMS}}} \qquad (36).$$

Although *N* is constant in PF IMS, the relative increase in n_z compared to UF IMS is attributed to radial ripple and central drift, which influence ion motion and serve to increase the effective path length traveled by the ion. The overall effect is that ions experience more collisions in PF IMS compared to UF IMS at identical *N*, thus the PF IMS mobility constant (described by eq. (24)) is smaller by a factor of α. For example,

Figure 15 contains simulations for $1/n_z$ as a function of E/N for equivalent UF IMS and PF IMS conditions. In both cases, the plot may be described by a linear function at low E/N that deviates at high E/N. Independent of the field strength, the value for $1/n_z$ is relatively smaller in PF IMS, which implies that ions undergo more collisions (compared to UF IMS) for equivalent operating conditions. At high E/N ($\gtrsim$ 70 Td), n_z values begin to converge, which suggests that under high field conditions, N is not sufficient for adequate collisional dampening and ion motion is not influenced by the weak radial electric fields (and thus, V^*) resulting in loss of radial ripple motion in PF IMS. That is, ion motion in PF IMS at extremely high E/N is comparable to UF IMS, although high field strengths are not typically employed. Moreover, using eq. (27), α may be approximated in the linear portion of the curve yielding, $\alpha \approx 0.80$ (as compared to $\alpha = 0.79$ derived above). This outcome is remarkably consistent with the fact that the major contribution of mobility dampening is attributed to a relative increase in n_z, whereas the additional ($\lesssim$2%) of mobility dampening is attributed to ions sampling $\vec{r}$-positions away from the central drift axis where $E_c < E$ (see Figure 7).

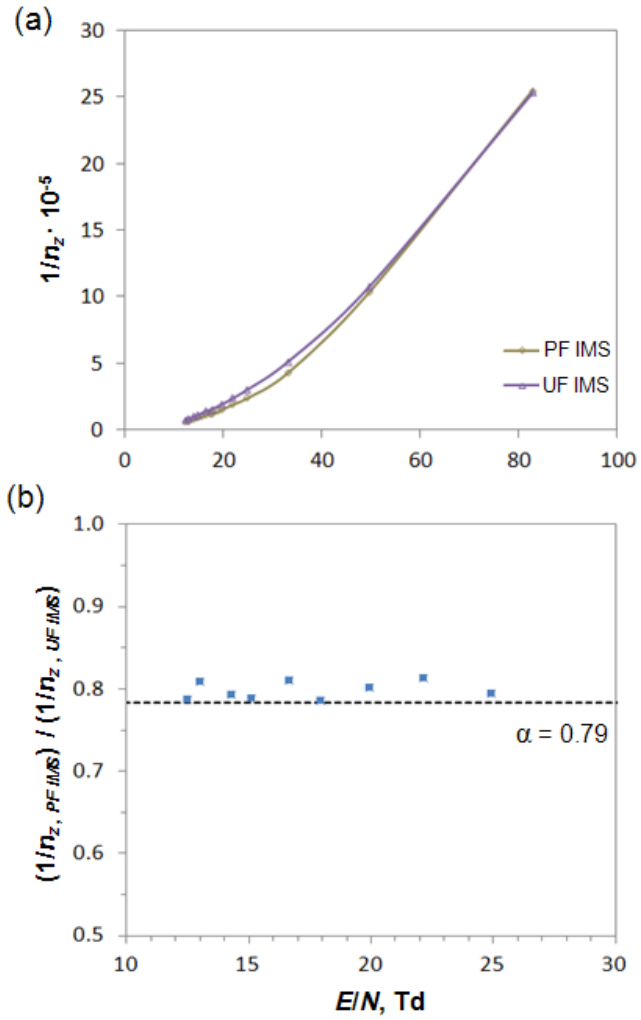

Figure 15. The origin of α: $1/n_z$ for bradykinin $[M + 2H]^{2+}$ at 8 V·cm^{-1} is simulated at varied P and plotted as a function of E/N for PF IMS (♦) and UF IMS (▲) conditions (a). In part (b), the data in the low E/N region is converted to $(1/n_{z,\ PF\ IMS}) / (1/n_{z,\ UF\ IMS})$ on the y-axis which approximates $\alpha \approx 0.80$ by eq. (36). For reference, the value $\alpha = 0.79$ determined from previous simulation results is shown with a dashed line.

4.6 Determination of Ω

The ion optics simulation results discussed thus far provide a strong fundamental basis to define and characterize α for PF IMS. From prior studies, we have determined that α is dependent upon the electrode geometry and pressure.[43,56] Because these

variables must be fixed for measurement of Ω, the remaining discussion focuses on empirical validation of the concept. The experimental data is limited to measurements performed at 1.00 Torr and ambient temperature to highlight the analyte-dependent parameters that influence α and consequently accurate Ω measurements.

Table 1 lists the model peptides and proteins used in these experiments. These analytes were selected because multiple Ω values have been reported in the literature from UF IMS measurements. The analytes represent a broad range of mass (~1050 to 12,400 Da), charge (2+ to 19+), and collision cross section (~240 to 2900 $Å^2$). Using the theoretical value $\alpha = 0.79$ derived from SIMION in eq. (10), Ω values were calculated for each analyte and compared to UF IMS literature measurements. The percent difference for these measurements is shown in Figure 16(a) as a function of charge state. Overall, the Ω measurements are in good agreement (< ±8% difference), however, careful inspection of the data indicates that the predicted Ω values for lower charge states ($\lesssim$ 10+) are generally larger than reported UF IMS values whereas Ω values for higher charge states ($\gtrsim$10+) are generally smaller. The relatively small charge state dependence may be accounted for by replacing α with a charge state-dependent value, $\alpha(z)$. The reasoning for this approach is discussed in the following section. Using this approach, Ω values were determined by the same procedure and compared to literature values; the percent difference analysis is shown in Figure 16(b). Comparison of Figure 4(a) and (b) indicates that utilizing $\alpha(z)$ instead of α decreases the magnitude of the percent difference (< ±4%) and randomizes the experimental differences about zero. Ω values derived from the later approach are listed in Table 1 for all charge states

observed. For reference purposes, the empirically determined charge state-dependent α(z) values used to calculate Ω are listed in Table 2.

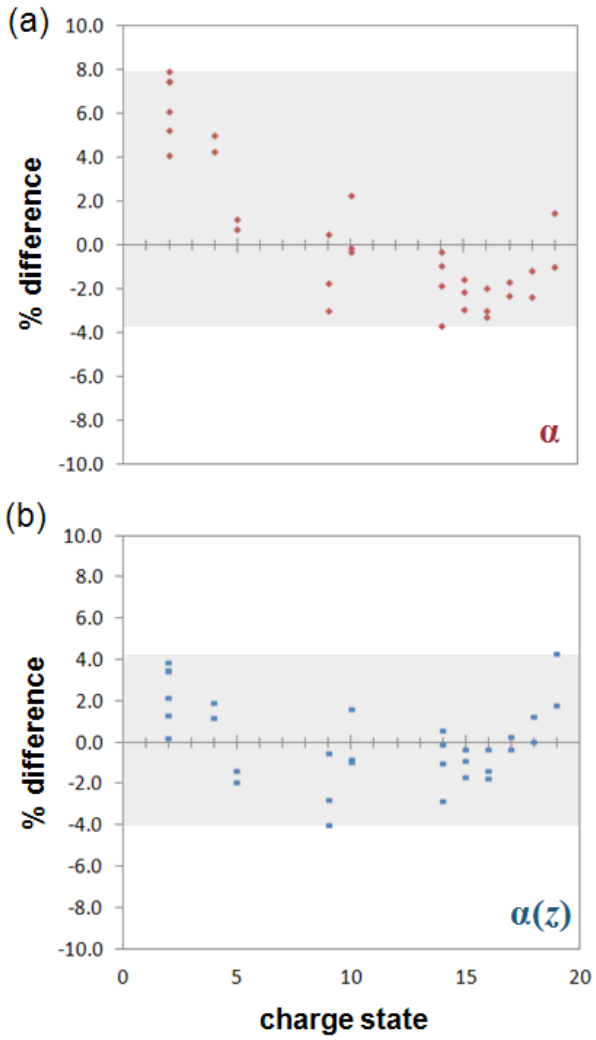

Figure 16. Percent difference in peptide and protein Ω measurements using PF IMS compared to UF IMS literature values (see Table 1) using α = 0.79 (a) and a charge state-dependent α(z) value listed in Table 2 (b). The data indicates that when a single α value is employed in eq. (10), a small systematic error is present owing to the charge state dependence, which is not considered. Utilizing α(z) to calculate Ω decreases the magnitude of the percent difference and randomizes the percent differences about zero.

analyte	z	$\Omega_{experiment}$, Å^2	$\Omega_{literature}$, Å^2	ref.	% difference
bradykinin	2	245 [a]	240	[63]	+2.1
			236	[64]	+3.9
			242 [b]	[60]	+1.3
			237 [c]	[57]	+3.4
angiotensin II	2	254	253	[65]	+0.2
			245 [c]	[57]	+3.5
melittin	4	583	572	[66]	+1.9
			576	[66]	+1.2
	5	593	602	[66]	-1.4
			605	[66]	-1.9
ubiquitin	9	1603	1649	[59]	-2.8
			1612	[64]	-0.5
			1670 [c]	[57]	-4.0
	10	1716	1733	[59]	-1.0
			1689	[64]	+1.6
			1730 [c]	[57]	-0.8
cytochrome c	14	2448	2473	[59]	-1.0
			2435	[64]	+0.6
			2451 [b]	[60]	-0.1
			2520 [c]	[57]	-2.8
	15	2555	2579	[59]	-0.9
			2564 [b]	[60]	-0.3
			2600 [c]	[57]	-1.7
	16	2633	2679	[59]	-1.7
			2642 [b]	[60]	-0.3
			2670 [c]	[57]	-1.4
	17	2731	2723	[59]	+0.3
			2740 [c]	[57]	-0.3
	18	2800	2766	[59]	+1.2
			2800 [c]	[57]	-0.013
	19	2921	2800	[59]	+4.3
			2870 [c]	[57]	+1.8

Table 1. Experimentally measured Ω values using PF IMS in He (g) for peptides and proteins at 300 K. The experimental Ω values were calculated using the charge state-dependent α function described in the text and given by Table 2. [a] Ω calculated from the centroid of the main peak corresponding to the longer arrival time (see Figure 14(a)). [b] Ω value measured in an Ionwerks drift tube which employs electrostatic high and low fields similar to PF IMS. [c] Ω value measured in an Syanpt G1 with a modified drift tube which employs UF IMS conditions with a superimposed RF-confining potential.

z	$\alpha(z)$
1	0.760
2	0.763
3	0.766
4	0.769
5	0.772
6	0.775
7	0.778
8	0.781
9	0.784
10	0.787
11	0.790
12	0.793
13	0.796
14	0.799
15	0.802
16	0.805
17	0.808
18	0.811
19	0.814
20	0.817

Table 2. Reference table for charge state-dependent α values given by the empirically derived expression $\alpha(z) = 3.03 \cdot 10^{-3} \cdot z + 0.757$.

Figure 17 contains a plot of literature Ω values (from Table 1) versus Ω values calculated herein using α(*z*) (from eq. (25)). The value for the slope of the linear regression trendline (1.00002) indicates that systematic errors are not present when α(*z*) values are employed. Note that the intercept (~4.5) is an indication of the error in $Å^2$. The high correlation coefficient (R^2 = 0.99881) across the wide range of data confirms general agreement of the dataset. Collectively, Figure 17 indicates that the charge state-dependent α values listed in Table 2 produce accurate Ω values across for peptides and proteins.

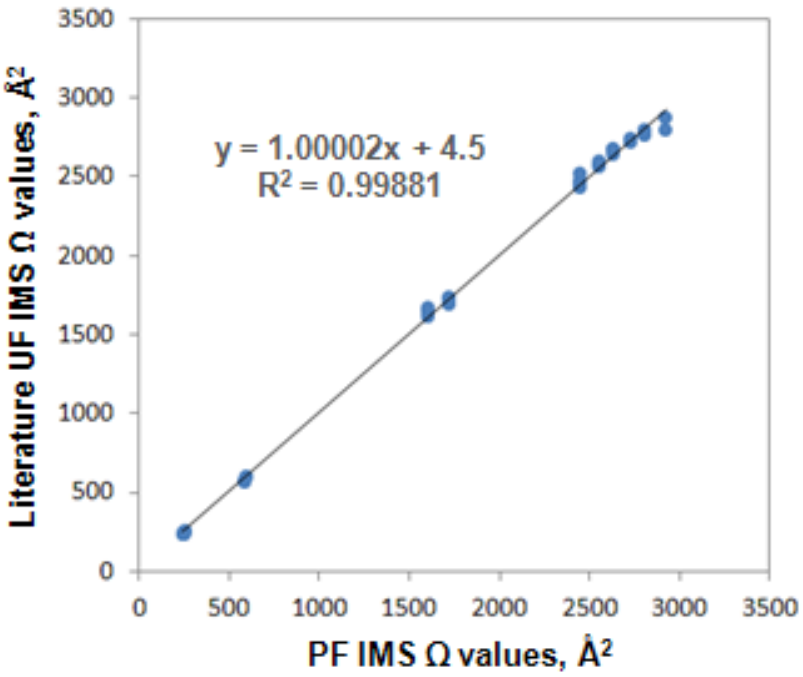

Figure 17. Calibration curve of literature Ω values versus Ω values measured by PF IMS.

4.7 Charge-state Dependence of α

The inclusion of α(z) in eq. (25) is justified by considering the difference in the amplitude of radial motion for ions with different charge states in an identical periodic focusing electric field. Although both species undergo axial as well as radial transport, the magnitude of the axial electric field is more than two orders of magnitude larger than the radial electric field.[56] Because the force exerted on the ion is proportional to charge ($F = q \cdot E$), more highly charged ions experience a relatively greater force in the axial dimension compared to the radial direction. This effect enhances the axial momentum ($p = m \cdot v$) of the more highly charged ion such that its amplitude of radial motion is decreased. Moreover, in the context of IMS, the drift velocity (see eq. (2)) is proportional to the acceleration of the ion between subsequent collisions ($a = q \cdot E / m$). Substituting ($q \cdot E / m$) for v into the momentum expression above yields a result that suggests momentum is directly proportional to the charge of the ion, because the periodic focusing electric field is equivalent and mass effects cancel.

Owing to the relatively higher magnitude of the axial force on ions carrying more charge, the axial momentum of the ion suppresses the radial ripple motion and more highly charged ions experience less mobility dampening, meaning that they have slightly larger α values, which is in fact, the observed experimental trend. These differences are small as the charge state-dependent α function has a slope that is two orders of magnitude smaller than the actual α value (see Table 2). Therefore, reasonable agreement for proteins and peptides may be obtained using only α, but better agreement is obtained using charge correction of the mobility damping factor.

A separate factor that may contribute to the charge state dependence of α is the fact that the magnitude of the effective potential is analyte-dependent and increases as a function of charge state. For example, neglecting collisional dampening effects, V^* for the 17+ charge state of cytochrome c is approximately 10-fold greater in magnitude as compared to the 2+ charge state of bradykinin. Owing to the relative extent of ion confinement along the central drift axis, this effect would also result in bradykinin $[M + 2H]^{2+}$ encountering more collisions per unit $\vec{z}$-displacement relative to cytochrome c $[M + 17H]^{17+}$, and thus, a smaller α value. However, central drift motion induced by the effective potential is a small effect (compared to the radial ripple motion), and its contribution to α is likely negligible.

4.8 Comparison to the RF-Confining Drift Tube

The determination of Ω using PF IMS is analogous to the RF-confining drift tube recently implemented into a Synapt G1 by Bush *et al.*, which superimposed RF voltage on a drift tube device.[57] A schematic diagram of the device is shown in Figure 18. Although this drift tube design offers independent control of the magnitude of the RF and DC potentials, PF IMS does not as the effective RF is generated in the inertial frame of the ion with a given axial velocity traversing a position-dependent radial electric field. The authors noted that Ω values obtained using the RF-confining drift tube were slightly larger (0.3 ± 1.4%) than literature values obtained by UF IMS but were within the experimental error. Moreover, drift times measured at lower drift voltages deviated toward longer drift times—a result that has also been observed in a RF IF positioned at

the exit of a long UF IMS drift tube.[26] On the basis of the work described herein, we can conclude that under low (axial) field conditions, the RF-confining drift tube and RF IF also contain a mobility damping factor (α) that originates from radial ripple motion and causes an increase in n_z relative to UF IMS conditions. At higher drift voltages, this deviation is not observed, which is also consistent with our results. Hence, sufficient electric field-driven momentum gains in the axial direction can suppress radial ripple motion for an ion in an electrodynamic or electrostatic system.

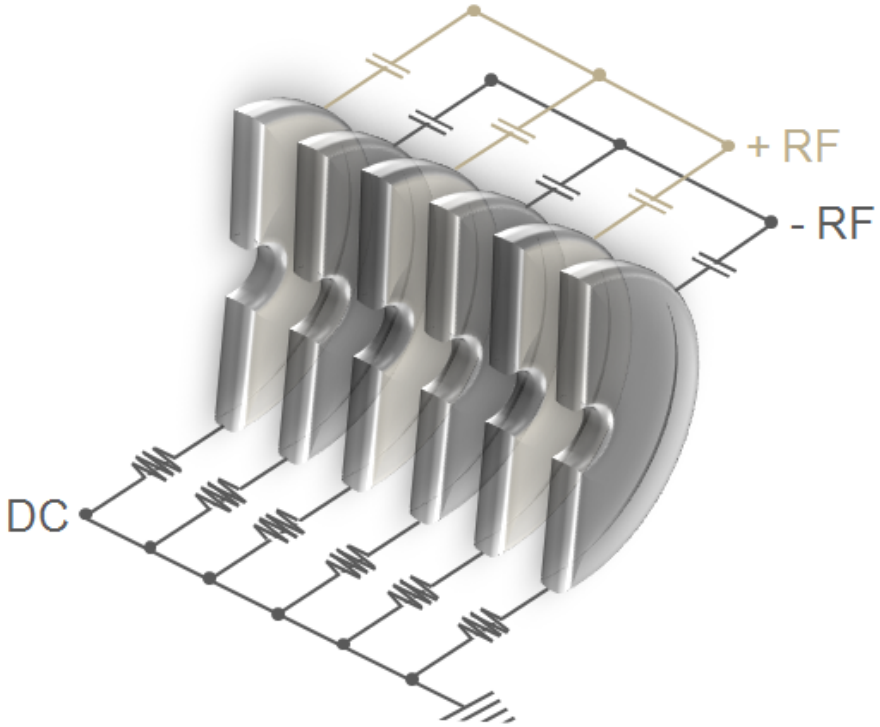

Figure 18. Schematic diagram of the RF-confining drift tube. The 2.7 MHz RF frequency (200 V_{p-p}) is applied to adjacent electrodes out-of-phase. A linear DC voltage gradient facilitates ion transport through the 18 cm drift tube. The electrode dimensions are as follows: d = 7 mm, w = 0.5 mm, and s = 1.5 mm.

4.9 Conclusions

The methodology for obtaining accurate Ω values for proteins and peptides using PF IMS (s = w = 6 mm, d = 8 mm) operating at 1.00 Torr and ambient temperature (300 K) is described. By quantifying the extent of mobility dampening with respect to UF IMS measurements, accurate Ω values for bradykinin, angiotensin II, melittin, ubiquitin, and cytochrome c were obtained with excellent agreement compared to UF IMS measurements. The results validate that the relatively weak position-dependent radial electric fields in PF IMS induces oscillatory motion (a radial ripple effect caused by an effective RF) as ions traverse the device. Unlike TW IMS, careful selection of calibrant ions and instrument operating conditions is not critical (*viz.* calibration of PF IMS drift tubes does not require native calibrants whose Ω brackets the Ω of the analyte, optimization of T-wave velocity, measurement at several T-wave velocities, and evaluation of the calibrant ion dependence on T-wave velocity) because Ω is directly proportional to αt_d in PF IMS. Instead, reasonable Ω values may be obtained *via* direct measurement of the PF IMS drift time by simply incorporating $\alpha \approx 0.79$ into UF IMS expressions (eq. (25)), while optimal calibration ($\leq$ 4% difference) may be achieved through charge state correction of the mobility damping factor ($\alpha(z)$). The results presented herein suggest that charge state-dependence is an important consideration for calibration of PF IMS drift tubes as well as any IMS device that utilizes radial ion focusing strategies.

5. TEMPERATURE EFFECTS IN ION MOBILITY SPECTROMETRY

5.1 Effective Ion Temperatures in Periodic Focusing Devices

Since optimal operation of PF IMS requires intermediate electric fields (see Sections 1.2.2 and 4.4), the variable T_{eff} becomes increasingly important. Moreover, the PF IMS ion dynamics described in Sections 1 through 3 are reinforced by studying T_{eff}. The effective ion temperature was determined for fullerene following a semi-quantitative procedure previously demonstrated by Fernandez-Lima *et al*.[67] Figure 19 illustrates T_{eff} and the number of ion-neutral collisions per unit $\vec{z}$-dimension, with respect to three representative electrode subunits. The observed variation in T_{eff} is a result of changes in ion velocity (or kinetic energy) initiated by the periodicity of the electric fields (Figure 5) and enhanced by subsequent collisional cooling at low axial velocities. T_{eff} reaches a minimum in region B2 and a maximum in region A, and demonstrates the periodic ion heating and cooling phenomenon inherent in the device. Figure 19 also illustrates the inverse relationship between T_{eff} and the ion-neutral collision frequency. Although our simulations suggest that local effective ion temperatures can be high, the average T_{eff} in PF IMS oscillates above and below ~421 K at E_c/N 75 Td. It should also be noted that for reference purposes, we also investigated the effective ion temperature in a 32 cm uniform field IMS drift tube at the same field strength, which yielded a similar average $T_{eff} \approx 438$ K.

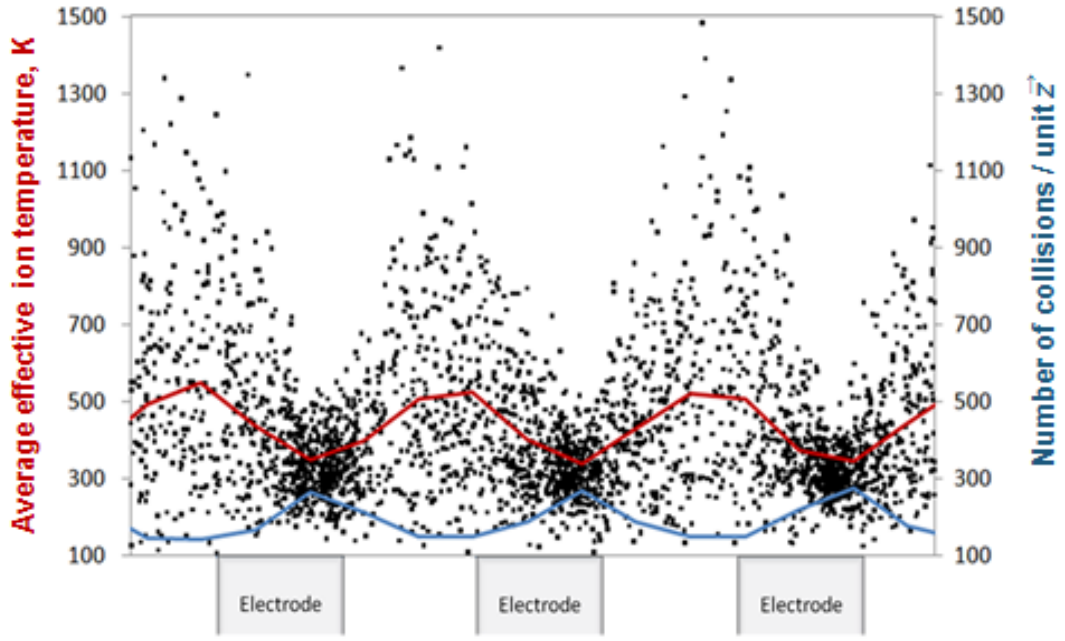

Figure 19. Effective ion temperature of a single fullerene ion (represented with black dots) and the average of several ion trajectories (shown in red, top trace). The number of ion-neutral collisions in 0.25 mm bins is shown in blue (bottom trace) across three representative electrodes.

T_{eff} is expectedly greater than T (298 K) because in this field, the translational kinetic energy of $C_{60}^{\bullet+}$ cannot be entirely quenched by a single collision with a helium atom at intermediate field strengths. Moreover, as expected from uniform field IMS in the intermediate field, as E/N decreases, T_{eff} decreases proportionally, owing to a decrease in acceleration between subsequent collisions, ultimately leveling off as T_{eff} approaches T. The low to intermediate field transition occurs ~25 Td as shown in Figure 20.

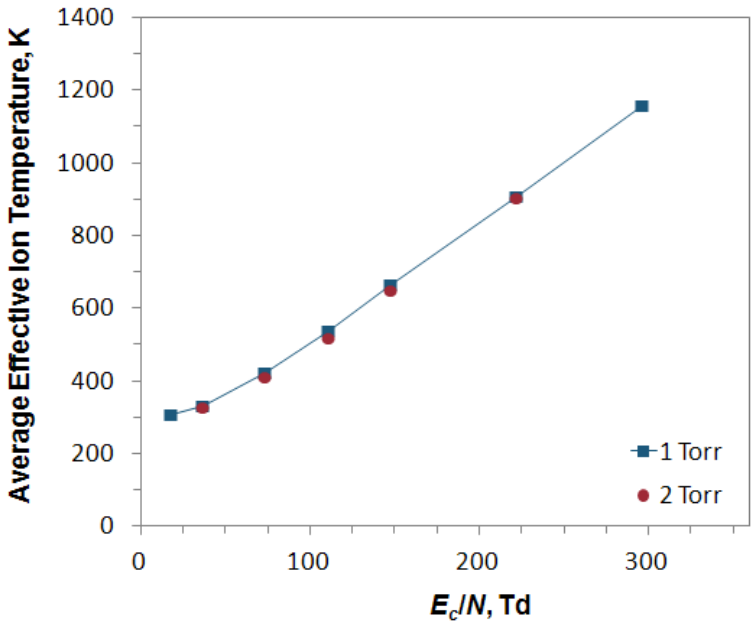

Figure 20. Average effective ion temperature of fullerene in a periodic focusing ion mobility spectrometer as a function of field strength. The data is shown at 1.0 (blue squares) and 2.0 (red circles) Torr.

Section 4 confirmed the presence of mobility dampening in PF IMS. A consequence of $n_{z,PF\ IMS} > n_{z,UF\ IMS}$ is that the macroscopic drift velocity is relatively smaller in PF IMS. Hence, all factors related to the drift velocity, including the field contribution to the average effective ion temperature ($\bar{T}_{eff}$), are reduced accordingly. However, similar to TW IMS, T_{eff} in PF IMS oscillates above and below $\bar{T}_{eff}$ as a function of $\vec{z}$-position as demonstrated in Figure 19.[50] Previous results for fullerene confirmed that average ion temperatures in PF IMS are comparable, yet slightly lower compared to UF IMS for equivalent operating conditions. Using the semi-quantitative approach outlined above, $\bar{T}_{eff}$ for bradykinin $[M + 2H]^{2+}$ at 25 Td (below the approximate low field limit given by eq. (26) in PF IMS is ~315 K as compared to ~318

K for UF IMS. At 50 Td (intermediate field strength), $\overline{T}_{eff}$ estimates for PF IMS and UF IMS yield ~364 K and ~366 K, respectively. It should be noted that depending upon the analyte-specific potential energy landscape, an increase in T_{eff} can alter the geometry and thus Ω. However, to date, we see no direct evidence for structural rearrangement for any of the model peptide and protein systems that have been presented in Section 4. Furthermore, the measured Ω values are in excellent agreement with previously reported values (see Figure 17). This may be attributed to the fact that in an intermediate periodic-focusing field where $\overline{T}_{eff} > T$, ions are periodically thermalized while drifting inside the electrodes, thereby inhibiting structural rearrangement between collisional cooling cycles. This result is also consistent with the fact that the RF-confining drift tube (discussed in the following section) and RF IF (which also imparts some internal energy into the analyte) positioned at the front and/or middle of UF IMS drift tube segments have no adverse effects to the measured Ω values.[68] Moreover, at near-thermal temperatures and bath gases having low polarizability (such as helium used exclusively herein), the dependence of Ω on temperature is minimal.[69]

5.2 Analytical Utility of Low Temperature IMS Measurements

While nearly all IMS measurements are performed at ambient temperature, tremendous analytical utility lies in reduced temperature measurements. First, eq. (1) shows that diffusion-limited resolving power is proportional to $(1/T)^{1/2}$. Hence, low temperature IMS measurements increase R owing to a decrease in drift gas speed and narrowing of the Maxwell-Boltzmann distribution. Second, diffusional broadening of the

ion swarm is inhibited at sub-ambient temperatures, which yields increased ion transmission through the conductance limiting aperture at the back of the drift tube. Third, when helium is used as the drift gas, reducing the temperature of the drift gas to 80 K results in condensation of typical gas impurities below their boiling point (see Table 3 and Figure 21), which decreases the probability of unwanted reaction chemistry inside the drift tube and increases the accuracy of Ω measurements. Finally, in the case of structurally labile biomolecules that possess potential energy surfaces with shallow wells, low temperature measurements can slow the rates of conformational interconversion such that individual conformational states can be resolved. These, and other aspects of reduced temperature IMS measurements are explored in Chapters 6 and 7.

Species	Phase Transition Temperature, K	Molecular Mass
H_2	20.35	2.02
N_2	77.3	28.01
CO	81.6	28.01
O_2	90.2	32.00
CH_4	111.6	16.04
C_2H_6	184.5	30.07
CO_2	216.6	44.01
C_3H_8	231.1	44.10
H_2O	273.2	18.02

Table 3. Phase condensation temperature for several common drift gas impurities.[15]

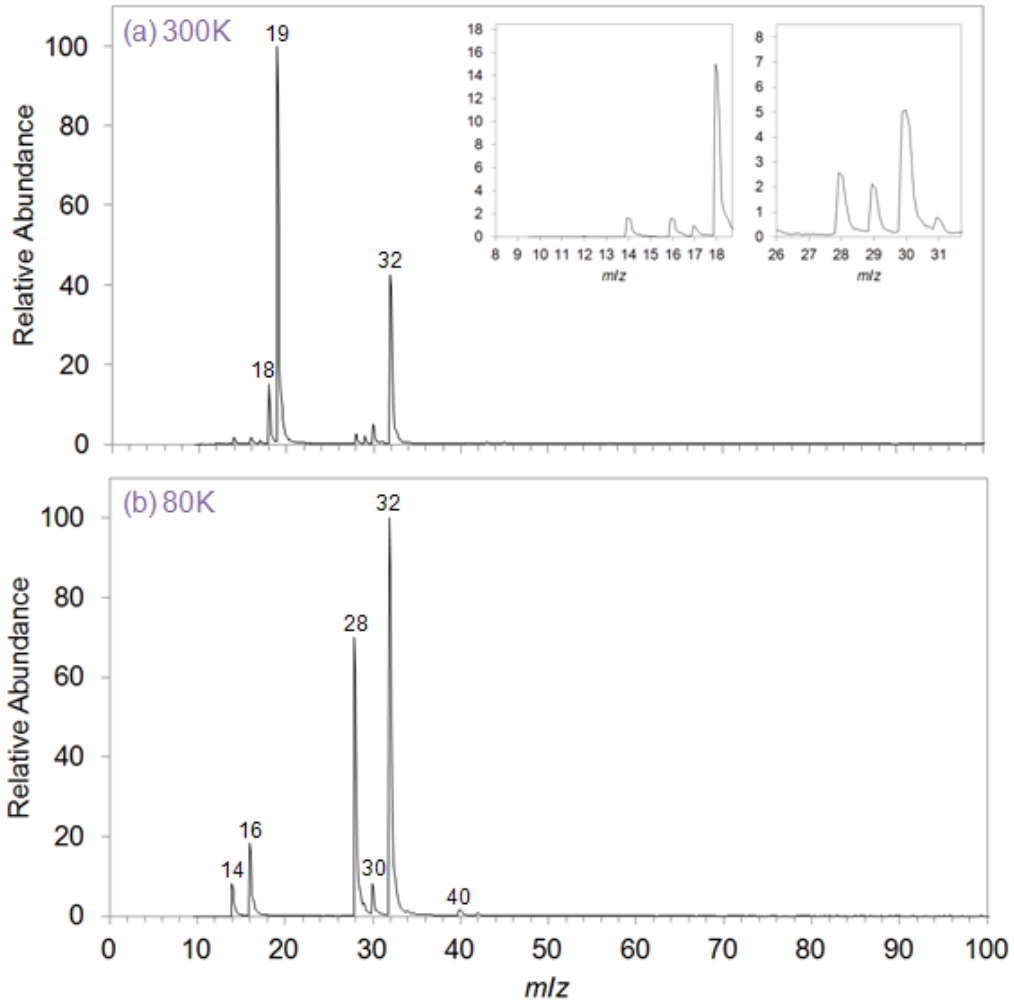

Figure 21. Mass spectrum obtained by increasing the pressure of the He (g) inside the drift tube (described in Chapter 6) above the breakdown Paschen limit. MS analysis of the cations contained in the plasma reveals the composition of contaminant species present at ambient (300 K, (a)) and cryogenic (80 K, (b)) temperature. At 300 K, the spectrum contains primarily $H_2O^{\cdot+}$ (*m*/*z* 18), $H_3O^{\cdot+}$ (*m*/*z* 19), and $O_2^{\cdot+}$ (*m*/*z* 32). At 80 K, residual water is condensed, however, the spectrum reveals that $N^{\cdot+}$ (*m*/*z* 14), $O^{\cdot+}$ (*m*/*z* 16), $N_2^{\cdot+}$ (*m*/*z* 28), and $O_2^{\cdot+}$ (*m*/*z* 32) are still present. Note that *m*/*z* 16 and *m*/*z* 28 may also arise from CH_4 and CO contaminants, respectively.

6. CRYOGENIC ION MOBILITY-MASS SPECTROMETRY CAPTURES HYDRATED IONS PRODUCED DURING ELECTROSPRAY IONIZATION*

6.1 Background

ESI characteristically generates ions that are depleted of solvent; however, numerous recent IMS and MS studies suggest that gas-phase peptide,[66,68] protein,[70] and multiprotein complex[71-72] ions formed by ESI can retain solution-phase features. Implicated in the preservation of the folded state are the relative stability of the native fold and electrostatic interactions that stabilize the desolvated ions on the analysis timescale (μs-ms).[59,73-76] IM-MS studies of native states require gentle instrument conditions that minimize ion temperatures (typically achieved *via* nano-ESI, high background gas pressures, low electric fields, *etc*.) such that weak non-covalent interactions and overall topology are preserved.[77] Unfortunately, the gentle instrument conditions needed for studies of native states come at the expense of ion transmission, IM resolution, and oftentimes require extended data acquisition times. Cryogenic IM-MS provides one possible route to circumventing these limitations.

Hydrated gas-phase ions represent a form of matter that is intermediate between gaseous and condensed states. Studies involving sequential hydration of biomolecules under equilibrium conditions,[78-82] observation of specific binding geometries from

* Part of this chapter is reprinted with permission from "Cryogenic Ion Mobility-Mass Spectrometry Captures Hydrated Ions Produced During Electrospray Ionization" by Joshua A. Silveira, Kelly A. Servage, Chaminda M. Gamage, and David H. Russell, 2013. J. Phys. Chem. A., 117, 953-961, Copyright [2013] by The American Chemical Society.

electrosprayed peptide ions,[83-84] as well as gas-phase spectroscopic analysis of small model systems[85-92] have provided insight into the kinetics, thermodynamics, and structure of hydrated biomolecules. However, IM-MS analysis of intact hydrated analytes produced from ESI has proven elusive, particularly because the weakly bound species are short-lived with respect to ion drift time and do not survive under typical operating conditions (300 K) owing to their relatively low stability.[93]

Previous studies have demonstrated several important advantages for cryogenic temperature IM including: (1) increased sensitivity and resolution through reduction in diffusional broadening of the ion swarm,[13] (2) increased drift gas purity,[14] and (3) the ability to "freeze-out" or kinetically trap inter-converting conformers on the timescale of the measurement.[94] To our knowledge, this is the first low temperature (~80 K) drift tube apparatus designed specifically for studies of non-covalent complexes and weakly bound cluster ions. In the present work, ion temperature effects on the distribution of protonated water clusters, $H^+(H_2O)_n$ (n = 2 to ~51), are examined using a novel cryogenic IM-MS apparatus. In this particular size range, the distribution contains species with enhanced stability, referred to as "magic number" clusters. The results for protonated water clusters provide a basis for interpreting similar distributions of hydrated peptides.

6.2 Experimental Methods

6.2.1 Sample Preparation

Protonated water clusters were generated by ESI from deionized water (18 MΩ) that was acidified with HCl (pH 3). For peptide studies, 50 μM solutions of bradykinin (Arg-Pro-Pro-Gly-Phe-Ser-Pro-Phe-Arg, Sigma Aldrich, St. Louis, MO) and gramicidin S (cyclo(-Pro-Val-Orn-Leu-DPhe-)$_2$, MoCell, Shanghai, China) were prepared in deionized water containing 0.1 % formic acid. All samples were directly infused at 400 nL min^{-1} from a pulled tip ESI emitter (50 μm initial internal diameter) into a stainless steel heated capillary maintained between 340 and 391 K. The potential difference between the emitter and capillary was maintained at 3.0 kV to generate protonated water clusters and 1.9 kV to generate hydrated peptides.

6.2.2 Instrumentation

A schematic representation of the home-built instrument is shown in Figure 22. A comprehensive list of all operating parameters is listed in Table 4 and 5. Ions formed by ESI are electro-pneumatically focused through a skimmer cone and transferred into the variable temperature drift tube using an electrostatic ion guide.[47,50] The ion guide is composed of 43 identical lenses (Kimball Physics Inc., Wilton, NH). The width and spacing of the focusing lenses in the ion guide is 1.27 mm and the inner diameter is 6.35 mm. The potential of adjacent lens elements alternates by ~40 V and the resulting oscillatory radial electric field focuses ions into a pulsed-gate electrode that is used to modulate the ions entering the IM drift tube. During IM-MS data collection, the gate

electrode is briefly pulsed from 388 V (ion deflection mode) to 320 V (ion transmission mode) for 12 μs at a frequency of 900 Hz.

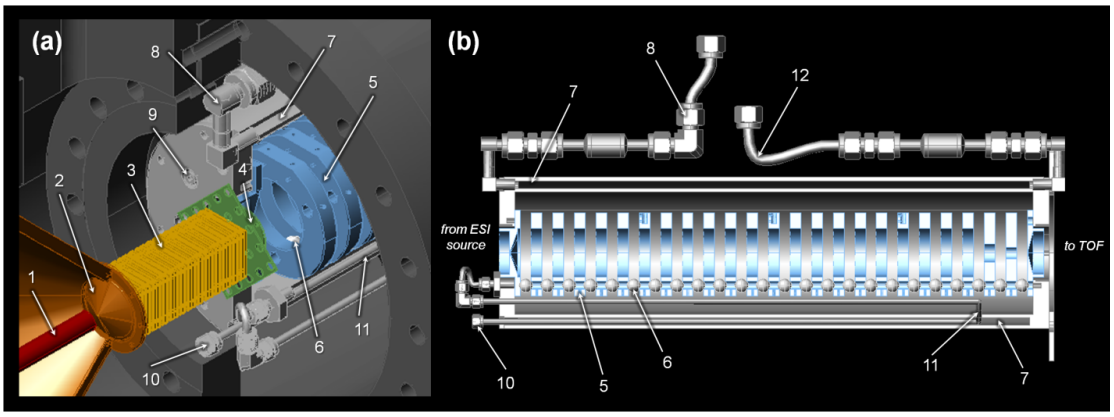

Figure 22. Cutaway view of the source (a) and drift tube region (b) of the instrument. Labels are as follows: 1-heated capillary, 2-skimmer cone, 3-DC ion guide , 4-IM gate, 5-IM ring electrode, 6-ceramic spacer, 7-cryogenic Dewar jacket, 8-cryogen inlet line, 9-electrical feedthrough, 10-helium gas inlet port, 11-drift gas pre-cooling line, and 12-cryogen outlet line. The inlet of the heated capillary (11.4 cm in length, ~400 μm internal diameter) is at ambient pressure whereas the pressure between the back of the capillary and the skimmer cone is typically between 1.0 and 1.5 Torr (depending upon the temperature of the capillary). The pressure in the DC ion guide and Dewar region is differentially pumped to ~$5x10^{-4}$ Torr to prevent ice buildup. Under typical tuning conditions, the potential difference from the skimmer cone to the front of the drift tube is ~50 V. Components shown in grey are at ground potential whereas all lens elements in color may be varied with a power supply. The source region of the instrument (shown here) is biased to positive potentials whereas the TOF region (not shown) is grounded.

The overall drift tube design was adapted from a previous hybrid IM-MS instrument described by May and Russell.[13-14] Briefly, the variable temperature IM drift tube is composed of 25 lens elements that are encased inside a cryogenic Dewar. This region can be maintained at temperatures ranging from 80 to 400 K. The thickness and spacing of all drift tube lens elements is 6.35 mm. The first 22 lenses have an inner diameter of 28.6 mm to provide a uniform electric field. The inner diameter of the last

two lens elements is tapered to achieve periodic focusing,[50,56,95] which increases ion transmission through the 800 μm exit aperture.[96] All electrodes are connected through a series of 1 MΩ resistors and are spaced by non-porous precision ceramic balls. A thin vespel insulating spacer isolates the first and last electrode from the Dewar. The entire drift tube assembly is held in place by compression onto indium wire seals that are fitted to the Dewar endcaps.

All measurements reported herein were collected during low temperature operation of the drift tube (83 ± 3 K), unless otherwise noted. The electric field inside the drift tube was maintained between 9.12 and 15.1 V cm^{-1}. Stable pressure was achieved using a flow controller (Type 640, MKS, Andover, MA) located near the gas inlet into the instrument. Using the calibration previously described by May and Russell, the pressure inside the drift tube was 1.6 Torr yielding field strengths between *E*/*N* 4.8 and 8.2 Td.[13] Ultra high purity helium (99.999%) was introduced into the drift tube through 3.175 mm stainless steel tubing. The helium gas was pre-cooled by introducing liquid nitrogen into the Dewar jacket. The temperature of the gas was measured using ceramic-encased platinum resistive temperature detectors (PT-100, Omega Engineering Inc., Stamford, CT) positioned inside the drift tube. The entire assembly is mounted inside the vacuum housing of the instrument and maintained at ~$5x10^{-4}$ Torr to minimize ice buildup. Upon an initial cooling cycle, plasma discharge of the helium gas inside the drift tube can initiate ion transmission via removal of condensed species deposited on the electrode surfaces.

Ions exiting the drift tube are pulsed orthogonally (12-15 kHz) into a time-of-flight (TOF) mass spectrometer maintained at ~$1x10^{-7}$ Torr via differential pumping. A description of the TOF has been reported elsewhere.[97] Ions are detected using an 18 mm dual microchannel plate assembly (MCP, Photonis, Sturbridge, MA). IM-MS spectra were recorded by pulsed synchronization of the gate electrode and TOF extraction source using custom 2D acquisition software provided by Ionwerks (Houston, TX).

Lens	**Voltage, V**
ESI emitter	~2500
heated capillary	366
source skimmer cone	359
DC IG 1	352
DC IG 2	279
gate lens	328
IM gate (open)	320
IM gate (closed)	400
IM front	311
IM back	36
TOF skimmer	0
Einzel 1	-39
Einzel 2	-3.8
Einzel 3	-30.2
Einzel 4	-20
TOF push	3.25
TOF liner	0
reflectron back ring	~4000
MCP front	-2600

Table 4. Typical operating voltages for all lens elements in the cryogenic IM-MS instrument.

Parameter, units	Setting
active time (+6.5), μs	55
resolution, ns	16
IM gate frequency, Hz	900
IM pulse width, μs	12
delay from IM gate to first TOF extraction, ms	0
run for #seconds, s	0
TOF extraction frequency, kHz	15
TOF extraction pulse width	2.667
number of TOF extractions/IM gate pulse	13
number of interleaved extractions	20
TDC start delay from extraction pulse, μs	5.07

Table 5. Typical Ionwerks software parameters used for cryogenic IM-MS experiments.

6.3 Results and Discussion

Figure 23 contains mass spectra of protonated water clusters, $H^+(H_2O)_n$ (n = 2 to ~51), acquired at different capillary temperatures. Hydrated cluster ions are formed within the ESI plume and/or by evaporation of larger droplets as they traverse the heated capillary. The relative ion abundances are directly linked to the relative stabilities of the clusters. Under similar conditions, the temperature of nascent cluster ions exiting the capillary has been estimated between 130 and 150 K owing to evaporative cooling.[84] Here, additional cooling of the cluster ions upon entering the drift tube (~80 K) aids in the preservation of the distribution produced by ESI.

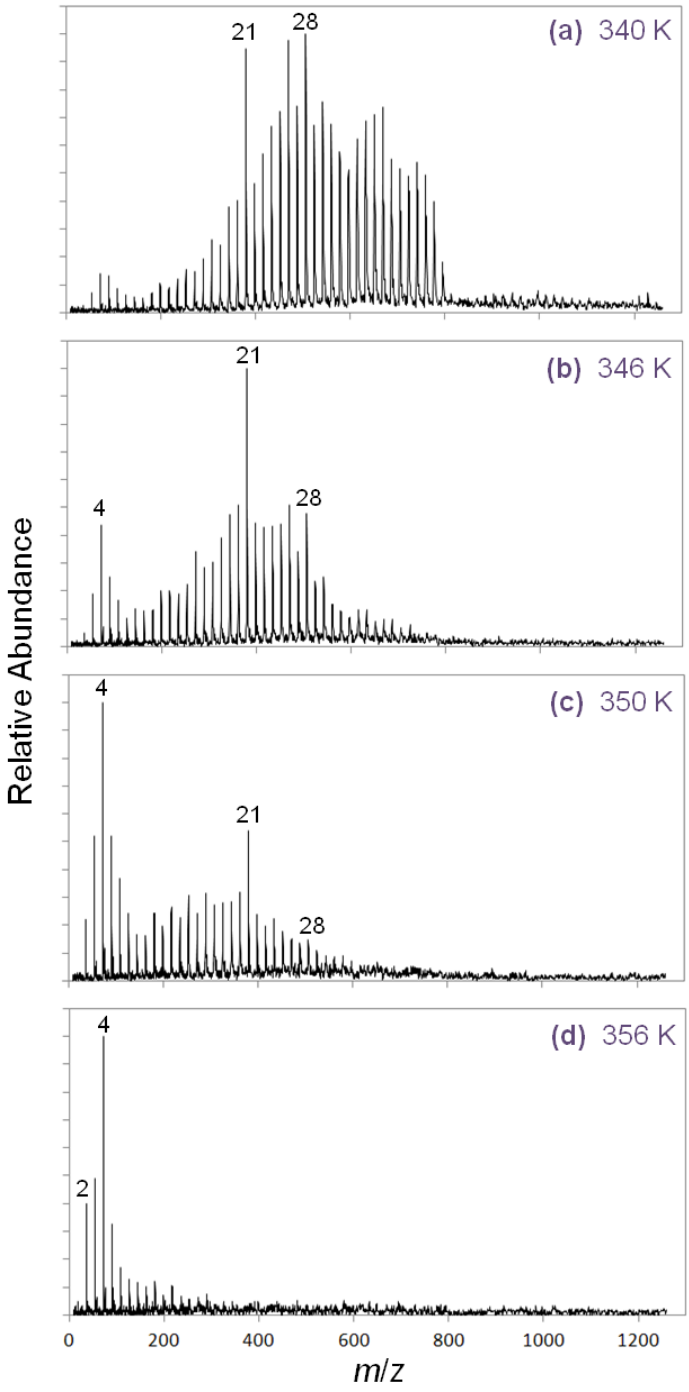

Figure 23. Mass spectra of protonated water clusters produced at different capillary temperatures (340 to 356 K) and constant IM field strength (5.0 Td).

During the evaporative ESI process, magic number clusters are produced and assigned herein on the basis of their enhanced abundance. At capillary temperatures between 340 and 350 K, magic number clusters n = 21 and 28 are clearly generated. These results are in excellent agreement with previous studies on the stability of protonated water clusters where the anomalously high abundances of n = 21[84,98-101] and 28[84] have been explained on the basis of structure, *viz.* magic number clusters can possess enhanced stability owing to the completion of closed clathrate cages (solvation shells).[100-101] Increasing the temperature of the heated capillary facilitates slow desolvation of the hydrated proton and shifts the overall distribution toward smaller n, though magic number clusters are still observed above the otherwise smooth distributions. At capillary temperatures greater than 350 K, only small cluster ions are detected. Under these conditions, persistent clusters indicative of special stability are observed in the small size region, namely, n = 4. Several studies have previously noted the enhanced stability of n = 4 ($H_9O_4^+$)[84,102] and *ab initio* calculations have suggested that this species is likely present as an H_3O^+-centered isomer having one H_2O monomer (H-bond acceptor) attached to each of the central hydrogen atoms.[103]

The detection of abundant magic number clusters over a range of capillary temperatures demonstrates that the low-energy ion-neutral collisions within the drift tube (maintained at 5.0 Td) preserve the cluster ions produced by ESI; however, it is also important to examine the effects of IM field strength on the resulting distribution. For IM measurements, it is imperative that the field strength is below the so-called "low-field limit" where the force exerted by the electric field is weak to ensure that the drift

time is directly proportional to Ω.[29] Here, although extremely weak field strengths are employed, we must consider collision-induced dissociation (CID), which is expected to proceed *via* loss of monomers:[104]

$$H^+(H_2O)_n \rightarrow H^+(H_2O)_{n-1} + H_2O \quad (37)$$

For this study, the heated capillary temperature was maintained at 340 K to produce a broad cluster distribution surrounding the region of interest (n = 21 and 28) while the electric field was increased from 9.1 V cm^{-1} (5.0 Td) to 15 V cm^{-1} (8.4 Td). Generally, the data shown in Figure 24 indicate that at low electric fields, persistent magic number clusters (n = 21 and 28) are indeed present. As the electric field is increased, the abundances of these ions decrease such that the distributions become increasingly smooth while the appearance of small clusters (probable terminal products of dissociation, n = 2 to 4) become increasingly abundant.

The exact onset of CID is more easily observed in Figure 25 which contains a plot of percent ion abundance for n = 20 to 22 versus IM field strength. In the low-field region of the curve (<5.8 Td), the percent abundance of cluster ion species in this size range collectively decreases as E/N increases because ion transmission for higher m/z species improves with increased electric field strength (see Figure 24). At 5.8 Td, the sharp increase in the abundance of n = 20 and concomitant drop-off in the abundance of n = 21 is consistent with the onset of CID. Although we cannot discern the exact terminal products of dissociation for each particular species, the CID process primarily evolves *via* sequential loss of water monomers.[104] This is also supported by the fact that small clusters grow in stepwise, *viz.* n = 4, 3, then 2 become successively more abundant

as the electric field is increased (see Figure 24). It should also be noted that similar dissociative phenomena are produced when the drift tube temperature is increased while maintaining a low electric field (see Figure 26). Collectively, these results emphasize the critical importance of minimizing effective ion temperatures (even when extremely low field strengths are employed, *i.e.* < 10 Td) such that weakly-bound species do not dissociate during the IM measurement.

The previous data have demonstrated that at higher effective ion temperatures, n = 21 is decomposed into n = 20 (as well as smaller clusters) at a higher rate than its repopulation from larger clusters occurs, ultimately resulting in loss of its characteristic enhanced abundance. While the distinct drop-off in the abundance of n = 21 is useful for establishing a dissociative limit, the phenomenon is quite unusual given that larger clusters (that are present) can also dissociate under these conditions and preferentially repopulate magic number abundances; however, Figure 24-26 questionably show that this process does not occur.

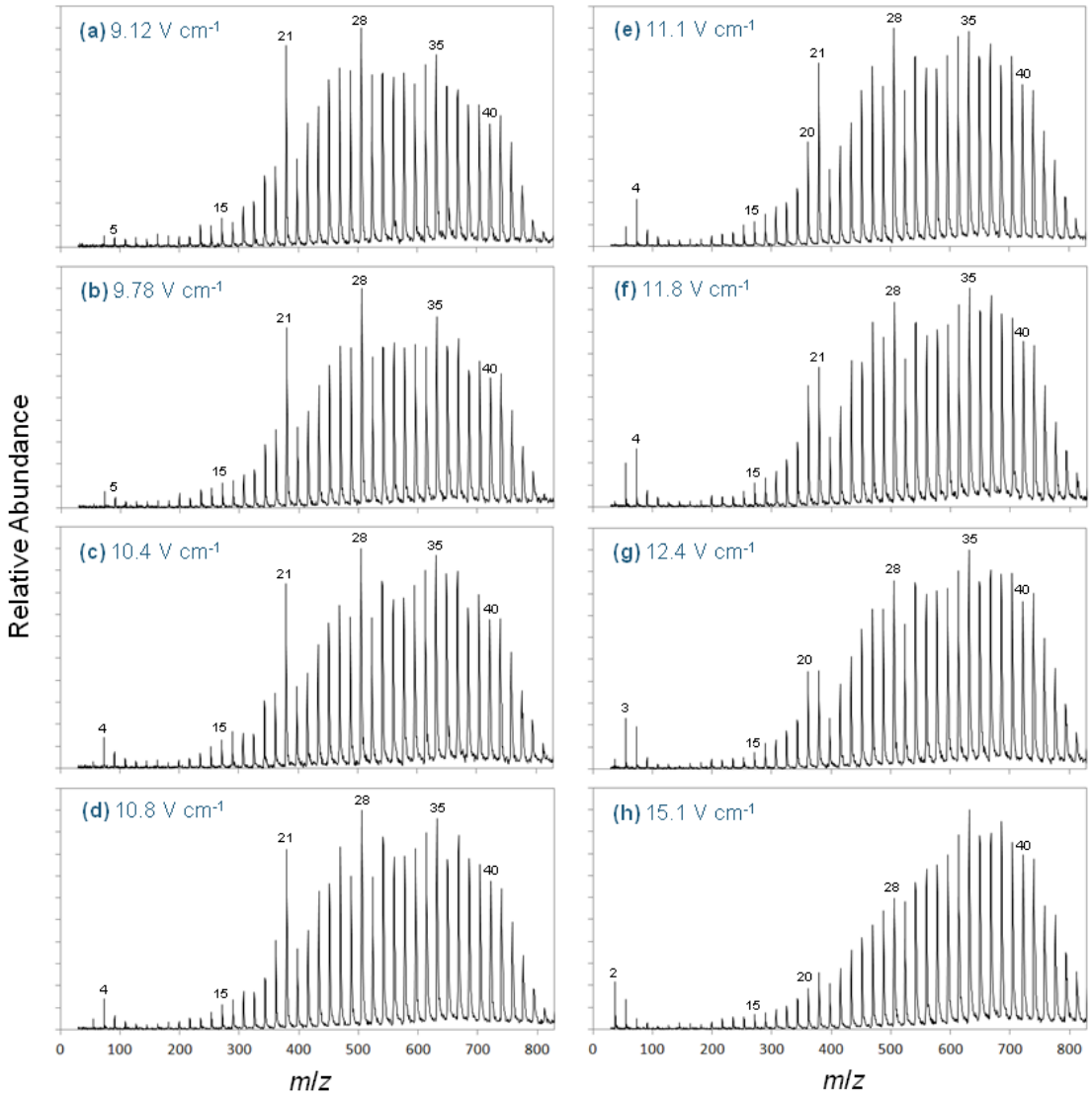

Figure 24. Mass spectra of $H^+(H_2O)_n$ (n = 2 to 45) as a function of electric field (9.1 to 15.1 V cm^{-1}) applied across the IM drift tube. These conditions correspond to field strengths in the range of 5.0 to 8.4 Td. In this cluster size range, magic numbers n = 21 and 28 are clearly observed above the otherwise smooth distribution of ions at lower fields. As the electric field increases, the ion-neutral collisional energy becomes sufficient to result in dissociation of monomers from cluster ions, evidenced by the gradual disappearance of magic numbers and the increase in small clusters (n = 2 to 4).

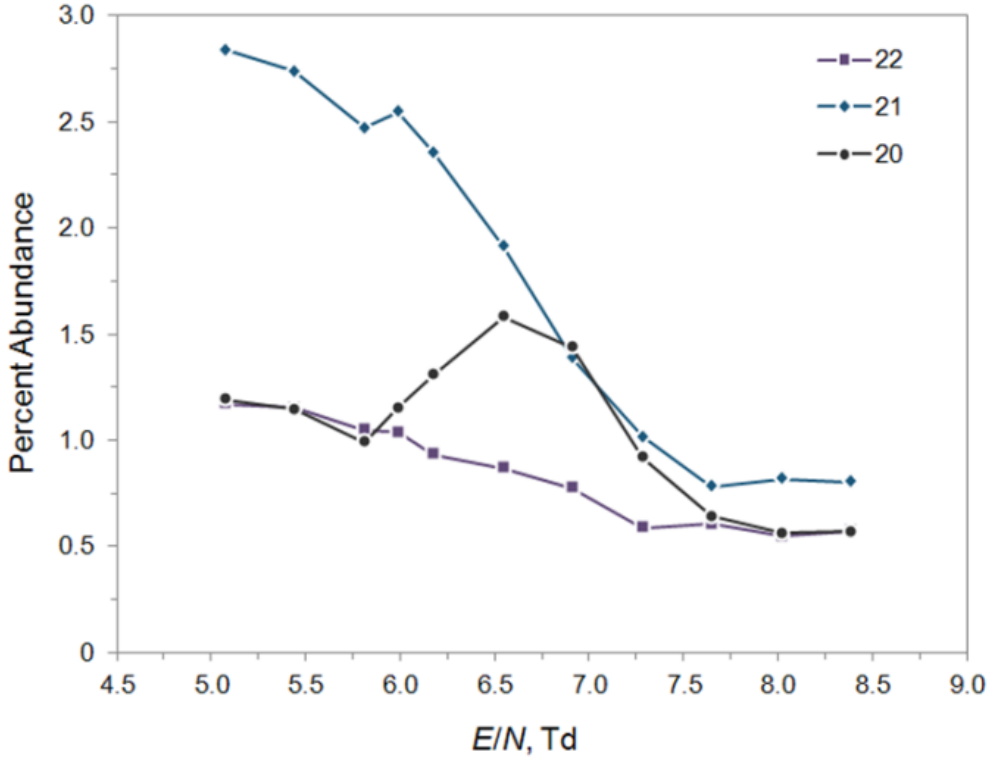

Figure 25. Percent abundance of $H^+(H_2O)_n$ (n = 20 to 22) as a function of the IM field strength.

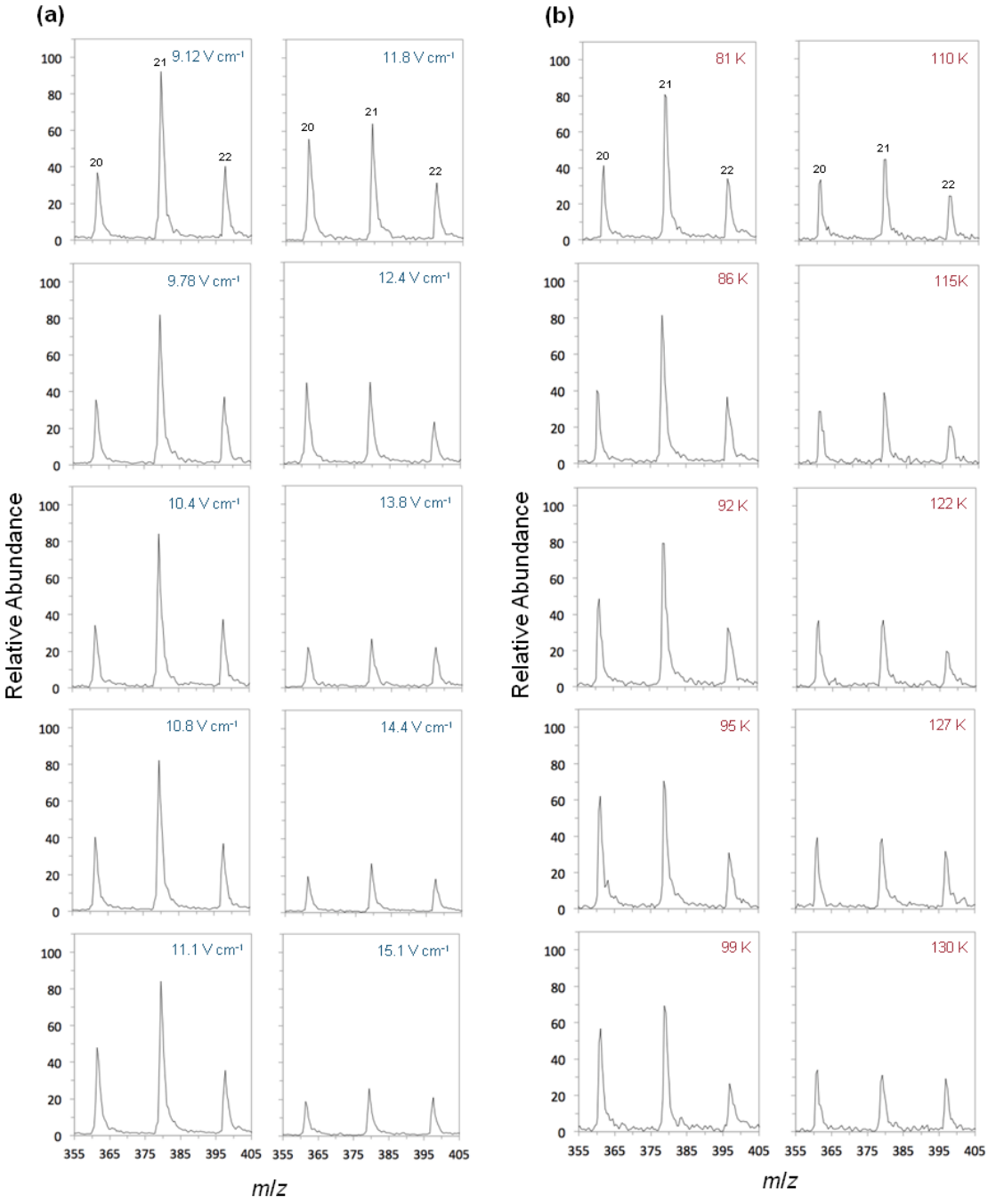

Figure 26. Expanded view of the mass spectra in the size range near n = 21: (a) as a function of electric field across the drift tube with constant $T \approx 80$ K, and (b) as a function of IM drift gas temperature with constant $E = 9.1$ V·cm^{-1}. Both thermal and electric field-induced ion heating result in a decrease in the magic number abundance such that the resulting abundances of n = 20 to 22 become similar.

To gain insight into the structure and isomer distribution of the clusters in the size region surrounding n = 21, the IM arrival time distributions (ATD) were obtained at E/N 4.8 Td—conditions well below the previously established dissociative limit. The plot of ATD versus m/z (see Figure 27(a)) confirms that the cluster ions are stable on the experimental timescale. Though the centroid of most peaks falls along a straight trendline, a unique signature is observed at n = 21. Compared to adjacent clusters, the mass-selected ATD for n = 21 reveals that this ion is comprised of at least two distinct populations (see Figure 27(c-e)). While several nearly isoenergetic structures are possible for the population that falls along the trendline,[105] the more abundant population is shifted toward shorter arrival time and is therefore assigned to a relatively more compact clathrate cage isomer. Singh *et al.* have demonstrated that several structures are possible for n = 21 when effective ion temperatures increase above ~145 K such that the clathrate cage can open to form a variety of isomers with fewer total H-bonds and more dangling H-atoms on the cluster surface.[105]

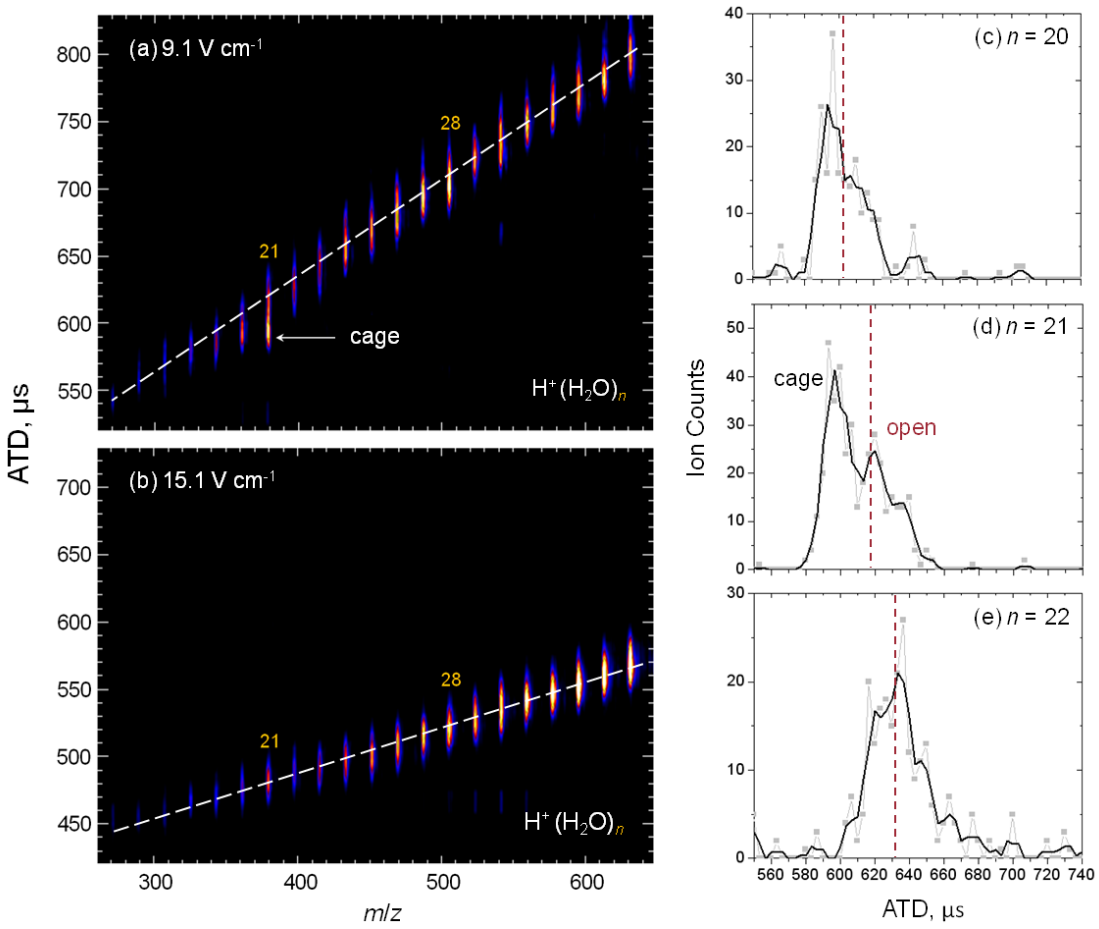

Figure 27. Two dimensional contour plot of ATD versus *m/z* for $H^+(H_2O)_n$ (n = 15 to 35) produced at an electric field of 9.1 V cm^{-1} (a) and 15.1 V cm^{-1} (b) in the drift tube. In both cases, the capillary temperature was 340 K such that the conditions are nearly equivalent to Figure 3(a). Panels (c-e) contain the mass-selected ATDs for (n = 20 to 22) at 9.1 V cm^{-1}. The black line is the result of boxcar averaging of the data points (grey ■). The vertical dashed line was inserted to guide the eye across the centroid of the IM-MS trendlines shown.

Hence, the IM-MS data supports the fact that nascent cluster ion temperatures produced from ESI (~130 to 150 K) are intermediate such that both open and closed cage isomers are produced. Based upon these findings, CID-induced loss of enhanced abundance for n = 21 may occur because dissociation of species n > 21 (having higher

effective ion temperatures) yield n = 21 product ions having open structures that lack special stability. Note the absence of a trendline deviation at n = 21 (cage isomer) for drift tube conditions that induce significant ion heating (Figure 27(b)). Collectively, these results support the temperature-dependent structural basis upon which magic number phenomena has been previously described.

Dehydration of nascent charged droplets formed during ESI can also yield interesting arrangements of water surrounding the charge-carrying groups found in peptide ions. Figure 28(a-f) contains mass spectra of bradykinin (BK) produced at different capillary temperatures. Abundant $[BK + 2H]^{2+}(H_2O)_n$ (n = 0 to ~73) ions are observed at a capillary temperature of 340 K (Figure 28(a)), whereas low abundances of $[BK + 3H]^{3+}$ ions are observed at higher capillary temperatures. Increasing the capillary temperature promotes desolvation of the peptide eventually yielding fully dehydrated $[BK + 2H]^{2+}$ and $[BK + 3H]^{3+}$ ions. The influence of capillary temperature on the $[BK + 3H]^{3+}$ ion yield implies that its formation is critically tied to the desolvation thermodynamics. Preferential formation of highly charged ions by ESI under conditions involving more rapid desolvation and/or ion heating has been noted by Sterling *et al.* and attributed to an electrothermal effect.[106] The experimental conditions used for these studies clearly favor formation of $[M + 2H]^{2+}$ over $[M + 3H]^{3+}$ ions as well as $[BK + 2H]^{2+}(H_2O)_n$ cluster ions, but the inset of Figure 6d shows that low abundances (< 1%) of $[BK + 3H]^{3+}(H_2O)_n$ species are indeed present. It is interesting to note that neither $[BK + 2H]^{2+}(H_2O)_n$ nor $[BK + 3H]^{3+}(H_2O)_n$ display specific solvation (magic number clusters). This result is consistent with studies by Lee *et al.* where the [BK +

$2H]^{2+}(H_2O)_n$ (n = 0 to ~100) distribution did not contain magic number clusters under similar evaporative conditions that facilitated progressive desolvation.[84]

Non-specific solvation of $[BK + 2H]^{2+}(H_2O)_n$ is also indicated by the IM-MS plot that does not contain deviations from the straight trendline produced by the cluster ions (see Figure 28(g)). At the current IM resolution (R ~30), no changes to the completely desolvated $[BK + 2H]^{2+}$ ATD were detected for inlet conditions that facilitated extensive hydration (340 K) and inlet conditions that yielded complete desolvation (386 K). These results are interesting given that the ATD is broad and non-Gaussian suggesting that multiple peptide conformations are present across a wide temperature range.

However, preliminary studies suggest that these phenomena are peptide specific. For example, Figure 29(a-c) contains mass spectra of gramicidin S (GS) produced at different capillary temperatures. Similar to the results presented for BK, $[GS + 2H]^{2+}(H_2O)_n$ species are observed over a range of capillary temperatures. Dehydration of GS differs from BK in that ions corresponding to n = 8, 11 and 14 are detected at greater abundance compared to adjacent cluster ions within the $[GS + 2H]^{2+}(H_2O)_n$ (n = 0 to ~26) distribution (see Figure 29(a)). In this size region, these magic number clusters have been previously reported by several groups.[83-84,91]

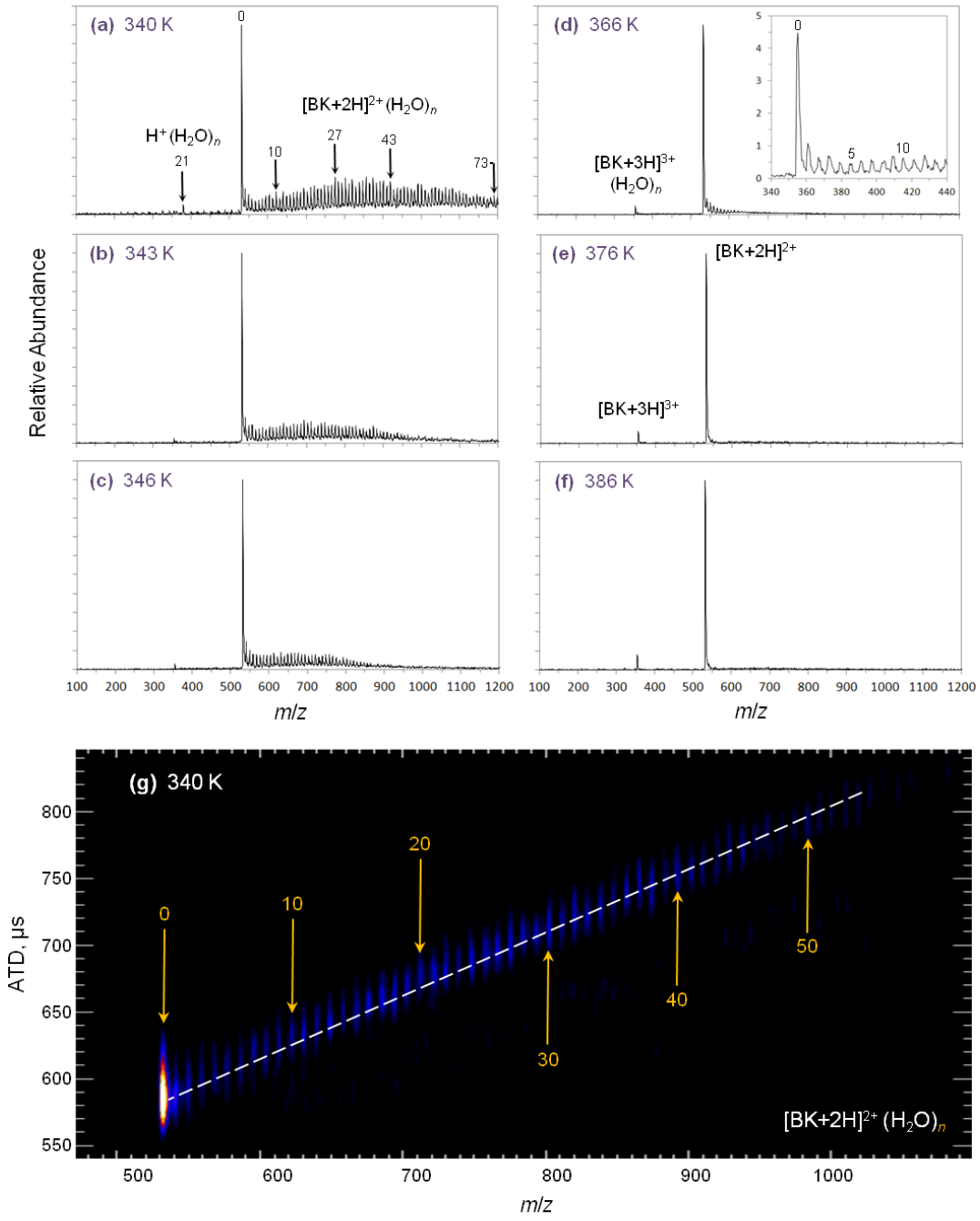

Figure 28. Mass spectra of hydrated bradykinin at varied capillary temperatures (340 to 386 K, a-f). Panel (g) contains a two dimensional plot of ATD versus *m/z* for $[BK + 2H]^{2+}$ $(H_2O)_n$ (n = 0 to ~55) produced at 4.9 Td. The dashed line was inserted to guide the eye across the IM-MS trendline.

The IM-MS plot for $[GS + 2H]^{2+}(H_2O)_n$ (n = 0 to ~24) shown in Figure 29(d) differs significantly from both $[BK + 2H]^{2+}(H_2O)_n$ and $H^+(H_2O)_n$ ions as the ATDs do not fall along a uniform trendline. Particularly evident at n = 8, it is unlikely that this deviation and other irregularities observed are attributed to conformational changes as a function of progressive desolvation. Nagornova *et al.* have recently reported that only the first two water molecules induce a significant conformational change to GS by weakening the NH_3^+-π interaction. Based upon these results, it is likely that irregularities observed in the IM-MS data may be attributed to favorable arrangements of water surrounding the ammonium groups. Liu *et al.* investigated the gas-phase hydration of several small peptides and noted that, under equilibrium conditions used in the study, the maximum number of water adducts correlated strongly with the number of charged functional groups present, ultimately yielding a ratio between 5 and 7 water molecules per unit charge.[79] Hence, $[GS + 2H]^{2+}(H_2O)_n$ (n = 14) likely corresponds to exclusive hydration of the ammonium ion.

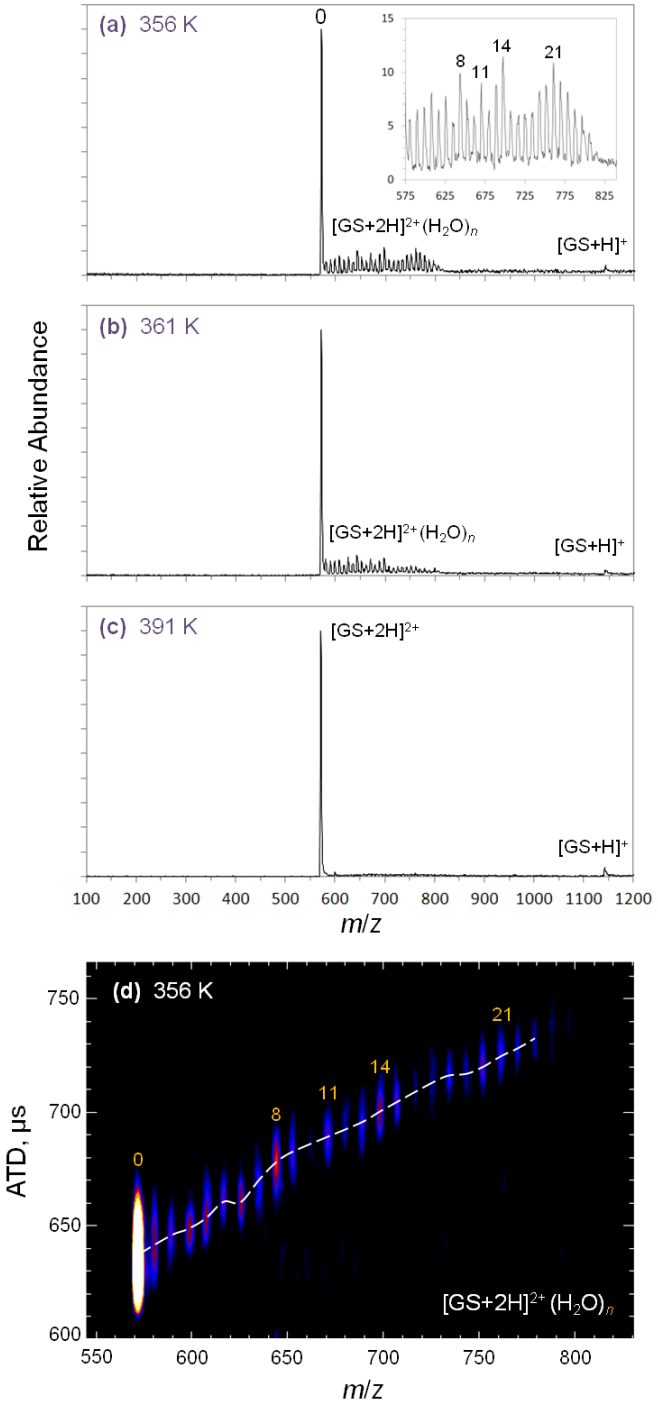

Figure 29. Mass spectra of hydrated gramicidin S at varied capillary temperatures (356 to 391 K, a-c). Panel (d) contains a two dimensional plot of ATD versus *m/z* for [GS + 2H]$^{2+}$ $(H_2O)_n$ (n = 0 to ~24) produced at 4.9 Td. The dashed line was inserted to guide the eye across the IM-MS trendline.

Interestingly, n = 14 also corresponds to the exact number of water molecules required to overcome the Coulombic repulsion of two isolated ammonium groups and fold 1,7-diaminoheptane *via* a solvent bridge.[92] For GS, it remains unclear whether solvent bridging actually occurs in a similar manner; however, sequential loss of the neutral water trimer (or possibly three individual water monomers) from $[GS + 2H]^{2+}(H_2O)_n$ (n = 14) would yield n = 11 and 8. The preference for formation of these species may be the enhanced stability of the cyclic water trimer that contains three intramolecular H-bonds.[107] The terminal magic number cluster, n = 8, can be viewed as having four water monomers bound to each ammonium ion, which may not appear particularly stable unless alternatively considered as an $H_9O_4^+$ adduct that does in fact possess enhanced stability (see Figure 2b-d).[84,91,102]

$$-NH_3{}^+\cdots(H_2O)_7 \longrightarrow -NH_3{}^+\cdots(H_2O)_4 \;\; or \;\; -NH_2\cdots(H_9O_4)^+ + (H_2O)_3 \;\; or \;\; +3(H_2O) \qquad (38)$$

Charge delocalization arising from the similar proton affinities (PA) of the two species may provide additional stabilization to the n = 8 cluster ion (*viz.* ($PA(H_8O_4)$ ~225 kcal mol^{-1} versus PA(Orn) ~233 kcal mol^{-1}).[108-111]

6.4 Conclusions

Stabilization of weak non-covalent interactions during the transition from condensed to gaseous states requires gentle IM-MS instrument conditions. Extensively

hydrated ions are produced by ESI at low inlet temperatures and preserved in the drift tube by employing cryogenic cooling (~80 K) at sufficiently low IM field strength. The results presented herein establish a low field dissociative limit for cluster ions held together by hydrogen bonds. Below this limit, IM is employed as a useful probe of ion structure as IM-MS trendline deviations are observed at magic number cluster species for both hydrated protons and peptides.

Our collective findings indicate that water evaporation from cluster ions is largely dependent upon the particular charge-carrying species within the cluster. Most notably, IM-MS data of protonated water clusters suggest the presence of multiple isomers at the magic number cluster n = 21, including a compact clathrate cage. Generation of this particular isomer appears largely dependent upon the effective ion temperature since distributions collected above the dissociative limit do not contain features with enhanced local stability. These results are consistent with the temperature-dependent structural basis by which magic number phenomena have been described.

It is especially interesting to note that hydrated $[GS + 2H]^{2+}$ ions displayed magic number clusters (n = 8, 11, and 14), but hydrated $[BK + 2H]^{2+}$ ions did not demonstrate specific solvation. These differences may, in part, be attributed to the relative energies of hydration for ammonium (GS) and guanidinium (BK) containing ions. However, for peptides, additional intramolecular interactions such as zwitterion formation and intramolecular charge solvation can influence the hydration process. Future studies aimed at examining the effects of amino acid composition on the products of dehydration will lead to a comprehensive understanding of the evaporative process

captured at ~80 K. Nonetheless, the cryogenic IM-MS instrument platform provides a new approach for investigating important fundamental questions related to the evaporative ESI dynamics, the origin of solution-phase and gas-phase conformers observed by IM, cluster chemistry, and stepwise dehydration of biomolecules.

7. FROM SOLUTION TO THE GAS-PHASE: STEPWISE DESOLVATION AND KINETIC TRAPPING OF SUBSTANCE P REVEALS THE ORIGIN OF PEPTIDE CONFORMATIONS

7.1 Background

Conformer preferences of biomolecules, such as proteins and peptides, are dictated by both inter- and intramolecular interactions. Because of the large number of degrees-of-freedom in bulk solvent networks and the dynamic nature of hydrogen bonds,[101,112-113] the specific interactions of a particular conformational state can be challenging to study in explicit environments (*i.e.* in solution or interacting with/inserted into a lipid membrane). Gas phase studies of solvent-free biomolecules provide a potential solution to this problem because inter- and intramolecular interactions are effectively decoupled.[87-88,91,114] However, a potential concern is that during the transition from solution to gas phase via electrospray ionization (ESI), biomolecules encounter unique environments that can potentially affect their structure.[115-117] A number of studies have demonstrated that upon ESI, peptide and protein ions can retain memory of their solution structures,[62,68,70,72,74-75,118-121] suggesting that gaseous ions can be kinetically trapped in local minima along their potential energy surface owing to evaporative cooling and slow rates of isomerization. Although covalent bonds are preserved upon ESI, the effect of charge state and the extent to which noncovalent interactions are affected remain unresolved.

It is widely accepted that ESI begins with the production of charged droplets that undergo a series of evaporation and fission events under the influence of an electric field at ambient pressure and temperature, ultimately generating ions that are depleted of bulk solvent. Several models describing the generation of gas phase ions from nanodroplets have been proposed. A growing body of literature suggests that ions such as folded proteins are generated by the charge residue model (CRM), originally described by Dole *et al*.,[122-123] whereby small nanodroplets containing a single analyte species evaporate to yield dry ions that can retain native structure in the gas phase. Recent molecular dynamics simulations by Breuker and McLafferty suggest that during the final stages of evaporation, remnant solvent adducts surround the outermost charged residues thereby shielding intramolecular interactions in the partially solvated protein ion.[115] Alternatively, low molecular weight species are thought to be transferred into the gas phase by the ion evaporation model (IEM).[124] Originally proposed by Iribarne and Thompson, the IEM suggests that before charged droplets become sufficiently small such that they contain only a single solute molecule, the surface charge density is sufficient to eject an ion residing near the nanodroplet surface into the gas phase.[125] Consta[126] and Konermann[127-128] have proposed that unfolded/extended macromolecules are ionized via a similar chain ejection mechanism. However, experimental techniques that can directly probe the structure and dynamics of biomolecules at intermediate extents of hydration are limited, and little is known about the final stages of desolvation during ESI. Consequently, the question posed above, “for how long, under what

conditions, and to what extent, can solution structure be retained without solvent?", remains unresolved.[115]

We recently introduced cryogenic ion mobility-mass spectrometry (IM-MS) as a new technique for studying conformations of hydrated gas phase ions produced during the evaporative ESI process.[129] Previous findings suggested that water networks formed upon evaporation are largely dependent upon the particular charge-carrying species present. Specifically, hydrated peptide ions that contain lysine (ammonium ions) display "magic number" clusters that possess enhanced stability, whereas hydrated peptide ions that contain arginine (guanidinium ions) do not exhibit specific solvation behavior. Here, we report a benchmark cryogenic IM-MS study that experimentally captures the evaporative dynamics of an amphipathic undecapeptide, substance P (SP, Arg^{1}—Pro^{2}—Lys^{3}—Pro^{4}—Gln^{5}—Gln^{6}—Phe^{7}—Phe^{8}—Gly^{9}—Leu^{10}—Met^{11}-NH_2), containing both arginine and lysine residues. As demonstrated below, cryogenic cooling of the IM drift tube to 80 K aids in the preservation of hydrated cluster ions formed during ESI such that the multiplicity of conformations that arise from solution and in the gas phase can be distinguished.

7.2 Experimental Methods

The cryogenic IM-MS instrumentation and experimental details have been recently described.[1] Briefly, hydrated ions were generated from a 50 μM solution of SP in water containing 0.1% formic acid by ESI using a home-built cryogenic IM-MS apparatus. The extent of hydration was controlled using a variable temperature heated

capillary inlet operated between 353 and 380 K. Cold cluster ions formed in the source region were transported into a 30.2 cm-long drift tube filled with 1.6 Torr helium (T = 80 ± 2 K). Ion transport through the drift tube was facilitated by a weak electric field (9.1 $V \cdot cm^{-1}$). The eluting cluster ions were pulsed into an orthogonal reflectron time-of-flight (TOF) mass spectrometer for mass-to-charge (m/z) identification.

Collisional activation studies were performed on a 1.38 m-long home-built IM-MS instrument that operates at ambient temperature. Ion activation was carried out in an ion funnel operated between 11 and 43 V cm^{-1} $Torr^{-1}$; the resulting ion populations were gated into the high-resolution periodic focusing drift tube for mobility dispersion. Determination of collision cross section values in a periodic focusing electric field has been previously described.[2] Ion-neutral collision cross sections were also measured using the high resolution uniform field IM-MS instrument in the Clemmer laboratory[3-4] at Indiana University and there is excellent agreement (values agree to within 2% error) between the two data sets.

7.3 Results and Discussion

ESI mass spectra of SP obtained from aqueous solution produce abundant distributions of both $[SP + 2H]^{2+}$ $(H_2O)_n$ (n = 0 to ~50) and $[SP + 3H]^{3+}$ $(H_2O)_n$ (n = 0 to ~30) ions (see Figure 30(a-c)); Beauchamp *et al.* termed the products of this process "freeze-dried biomolecules".[84] Increasing the temperature of the ion inlet facilitates more rapid desolvation and shifts the overall distribution toward smaller cluster sizes, ultimately yielding dehydrated doubly and triply charged SP ions. Note that singly

charged ions are not detected in appreciable abundance. These data not only demonstrate a high degree of control over the range of cluster size, but also show that the hydrated cluster ions detected are indeed the intermediates formed during the final stages of ESI.

The relative abundance of a particular hydrated ion is directly related to the relative stability of the local hydrogen bond network within the cluster. Figure 30(a-c) shows that during the evaporative process, magic number clusters are not evident among the relatively smooth distributions of $[SP + 2H]^{2+}$ $(H_2O)_n$ and $[SP + 3H]^{3+}$ $(H_2O)_n$ ions. En route to forming solvent-free ions, the primary sites of water association are the charged functional groups.[115,130] While magic number clusters (n = 8, 11, 14, 20, and 40) have been previously observed for ammonium-containing peptides and model compounds (alkyl amines), guanidinium-containing peptides are not known to display specific solvation.[83-84,91,129] Here, we hypothesize that because both functional groups are present in SP (Arg^1 and Lys^3), non-specific water clustering likely results from interplay between the charge sites localized near the flexible N-terminus.[131]

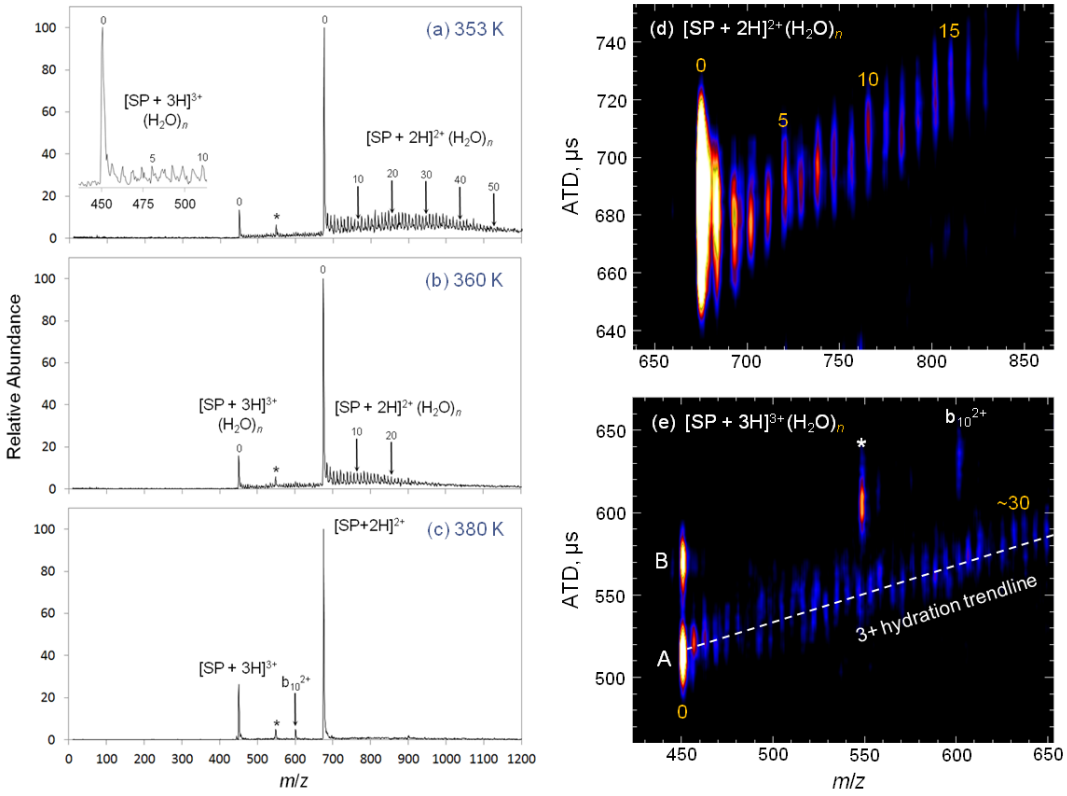

Figure 30. Cryogenic IM and MS results: (a-c) ESI mass spectra of SP ions captured prior to (a and b) and after (c) complete dehydration. The inset of panel (a) contains an expanded view of the region surrounding $[SP + 3H]^{3+}(H_2O)_n$ (n = 0 to 10). The peak labeled with an asterisk is a contaminant ion. (d-e) Two dimensional ATD versus m/z contour plots for $[SP + 2H]^{2+}(H_2O)_n$ (n = 0 to ~15) (d) and $[SP + 3H]^{3+}(H_2O)_n$ (n = 0 to ~30) (e) collected at an inlet temperature of 356 K. The trendline produced from triply charged SP hydrates is shown with a dashed line to guide the eye. $[SP + 3H]^{3+}$ conformer assignments are denoted A and B. In each experiment, the drift tube temperature was kept constant (80 ± 2 K) at a field strength of E/N 4.7 Td.

To gain insight into the structural evolution of SP as a function of cluster size, cryogenic IM-MS was employed under inlet conditions that produce extensively hydrated ions. The data, shown in Figure 30(d-e), reveal that both the doubly and triply charged ion forms of SP are comprised of dehydrated conformers that originated from evaporation of extensively hydrated ions (for $[SP + 3H]^{3+}$ this population is denoted A).

The near- linear decrease in arrival time for successive *n* to *n*-1 cluster ions within each distribution reflects the small decrease in the overall collision cross section upon stepwise desolvation, suggesting that these dehydrated populations contain conformations that largely resemble their solvated counterparts. Consistent with evaporative studies by Beauchamp *et al*., we find no evidence for dissociation of small clusters from these hydrated peptide ions, indicating that water evaporation occurs via sequential loss of monomers.[84] Moreover, fragment ions such as the b_{10}^{2+} species do not show evidence for water adduction, indicating that they are produced after complete desolvation. Interestingly, $[SP + 3H]^{3+}$ ions contain a second population of conformers observed at relatively longer drift times (denoted B) that do not result from the evaporative process. As shown in Figure 31(a), two possible scenarios explain this outcome: (1) conformer B is formed by the IEM, (*i.e*., expulsion from an intact nanodroplet thereby leaving no trace of its origin) or (2) B originates from a conformational change of a fully dehydrated conformer contained in population A.

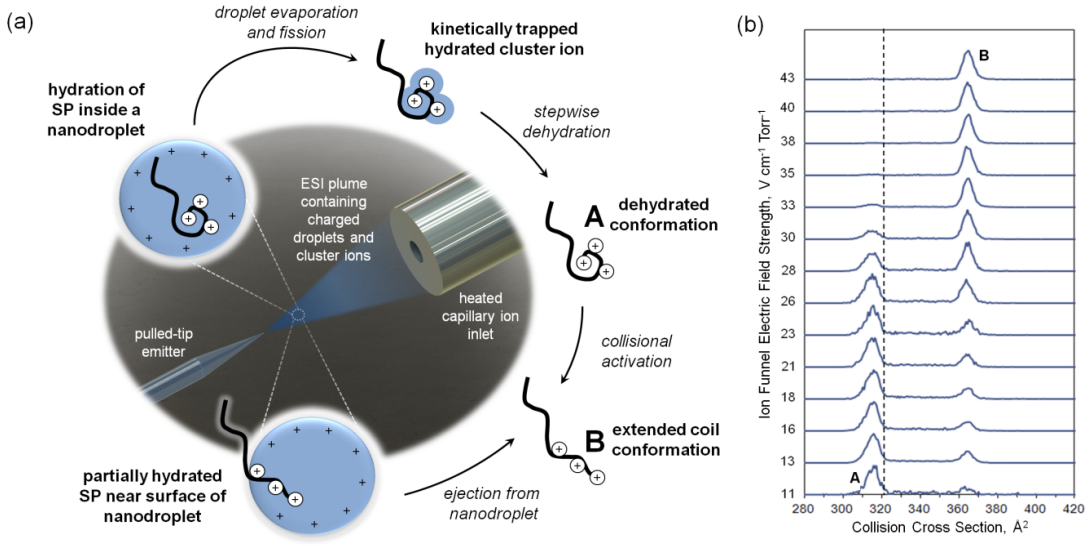

Figure 31. Two potential pathways for dehydration of $[SP + 3H]^{3+}$ ions from bulk solution via ESI. (a) The CRM (top route) describes the production of gas phase ions by evaporation of solvent from $[SP + 3H]^{3+}$ following successive fission of larger droplets. The IEM (bottom route), favored for surface-active molecules, produces ions by a field desorption process. In both cases, charged nanodroplets containing SP are produced in the ESI plume decay to ultimately yield solvent-free gas phase ions. (b) Mass-selected collision cross section profiles for $[SP + 3H]^{3+}$ ions obtained using a range of field strengths in an ion funnel prior to IM analysis. Each panel shows a separate profile where the effective ion temperature is increased by collisional activation with the helium buffer gas. For reference, the theoretical random coil trendline (321 $Å^2$) is shown with a dashed line. The theoretical collision cross section for $[M + 3H]^{3+}$ peptide ions was generated from a tryptic digest of a 10 component protein mixture.[3]

Because the former hypothesis is difficult to unambiguously examine by experiment, we instead tested the latter hypothesis by collisionally activating the nascent population of ions produced upon ESI prior to ambient temperature IM-MS analysis. The results, shown in Figure 31(b), confirm that populations A and B are indeed present at ambient temperature. These data support the latter hypothesis as the depopulation of A (318 $Å^2$) coincides with the subsequent elongation to B (368 $Å^2$). Note that the experimental collision cross section values are in general agreement with previous

studies. Collectively, these evaporative dynamics clearly indicate that SP ions are produced by the CRM. Hence, the transition from bulk solution to the gas phase for SP is described by the following scheme:

$$[\mathrm{SP}+3\mathrm{H}]^{3+}(aq.) \xrightarrow{droplet\ evaporation\ and\ fission} [\mathrm{SP}+3\mathrm{H}]_A^{3+}\,(\mathrm{H_2O})_{n\lesssim 30}$$

$$\xrightarrow{stepwise\ dehydration} [\mathrm{SP}+3\mathrm{H}]_A^{3+} \xrightarrow{activation} [\mathrm{SP}+3\mathrm{H}]_B^{3+} \xrightarrow{activation} fragments \qquad (39)$$

Consistent with the plurality of states produced upon ESI, previous NMR studies of SP in water have revealed that an ensemble of conformers coexist.[132] We note that the peak for A is significantly broader than that for B (see Figure 31(b)), suggesting that the ion population is comprised of multiple conformers that are transferred from solution to the gas phase, but are not resolved under the experimental conditions employed. Moreover, the compact size of conformers contained within A indicates that intramolecular interactions (*i.e.*, π-cation interactions involving Phe^7/Phe^8 and/or hydrogen bonding between Arg^1/Lys^3 and Gln^5/ Gln^6)[91,133-135] are likely responsible for kinetic trapping on the time scale of several milliseconds. The presence of multiple conformations is also consistent with NMR studies that showed SP adopts helical conformations in low-dielectric environments (*i.e.* embedded in a lipid membrane and docked in the receptor active site).[131-132] Here, we observe that conversion to a gas phase elongated coil (B) occurs only for the triply charged ion, which is the expected predominant species at extracellular pH 7.4. Because $[SP + 2H]^{2+}$ does not appear to

convert to an elongated gas phase population, we speculate that the process may be driven by repulsive Coulombic interactions between the multiple sites that are protonated. This outcome is especially interesting given that the ATD for $[SP + 2H]^{2+}$ also shows evidence for multiple conformational states (see Figure 32). Nevertheless, the conformational change for $[SP + 3H]^{3+}$ occurs only after complete dehydration! That is, intermolecular hydrogen bonds between $[SP + 3H]^{3+}$ and water molecules presumably compete with intramolecular hydrogen bonding sites required for conversion to B, ultimately inhibiting this transition.

7.4 Conclusions

Hydrated SP ions, sampled during the final stages of the evaporative ESI process, were analyzed by cryogenic IM-MS. The results provide direct evidence that upon ESI, $[SP + 2H]^{2+} (H_2O)_n$ (n = 0 to ~50) and $[SP + 3H]^{3+} (H_2O)_n$ (n = 0 to ~30) each produce dehydrated conformers originating from stepwise evaporation of extensively hydrated clusters. Evidence for structural changes as a function of variable extents of hydration was not observed in this size range, indicating that the population of dehydrated conformers largely resembles that of the hydrated species.

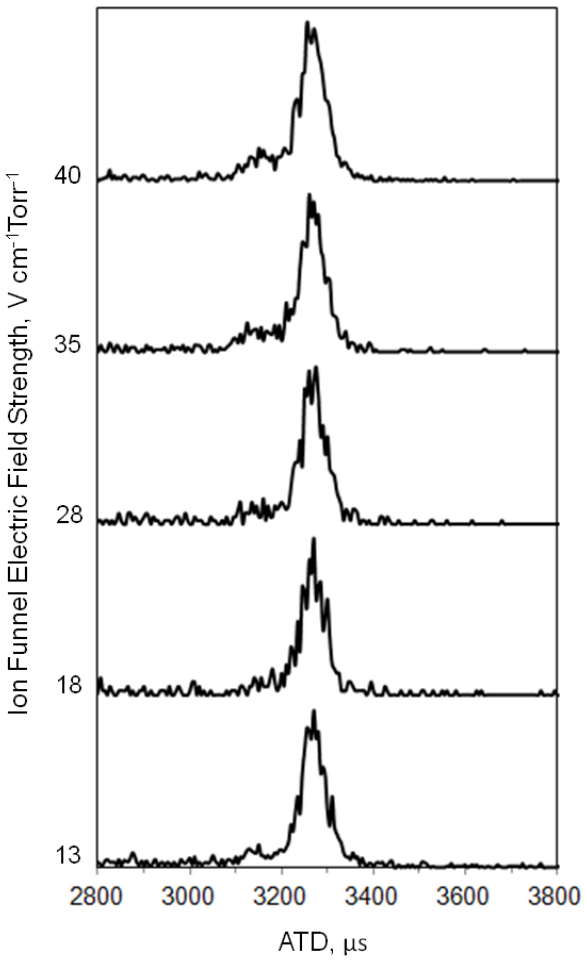

Figure 32. Mass-selected arrival time distributions for the $[SP + 2H]^{2+}$ ion. Ion heating is carried out prior to introduction into the IM drift tube (maintained at constant field strength). Increasing the electric field strength in the ion funnel results in an increase in the effective ion temperature owing to collisional activation.

Moreover, IM-MS hydration trendlines proved useful in assigning the origin of populations observed in the gas phase, especially in the case of $[SP + 3H]^{3+}$, which contains a second, non-hydrated conformer (B) that did not result from the evaporative ESI process. Collisional activation of the nascent population of conformers produced

upon ESI confirms that B originates from gas phase rearrangement of a conformation contained within population A. In the case of $[SP + 3H]^{3+}$, evaporative cooling (freeze-drying)[84] upon ESI kinetically traps a compact population of conformations (A) for several milliseconds, even though an extended conformation (B) is energetically favorable in the gas phase.

In the final stages of dehydration the stabilization afforded by solute-solvent interactions is replaced by stabilization from intramolecular interactions, *i.e.*, formation of salt-bridges and hydrogen bonds. Collectively, these results unambiguously show that upon ESI, doubly and triply charged SP conformers observed in the gas phase are generated by the CRM. The ability to follow the evolution of conformers as ions emerge from differing amounts of solvent in a one-solvent-molecule-at-a-time fashion provides a powerful new approach for understanding how key elements of structure are established in a range of environments.

8. SUMMARY

The fundamental principles of PF IMS have been comprehensively discussed. Radial ion confinement is attributed to a collisionally dampened effective potential that maintains ions near the central drift axis and ultimately results in high ion transmission. Equations of motion were derived that culminated into useful methodology for accurate determination of peptide and protein collision cross section values via inclusion of a mobility dampening coefficient. Though measured PF IMS drift times can be precisely determined by experiment and predicted by SIMION, the major source of error in the methodology stems from deviations in the Ω values reported in the literature.

Additionally, evaporation of water from extensively hydrated protons and peptides formed by ESI was examined using a cryogenic IM-MS instrument platform. In agreement with previous studies, the findings indicated that water evaporation is largely dependent upon the particular charge-carrying species within the cluster. IM-MS results for protonated water clusters suggest that the special stability of the well-known $H^+(H_2O)_n$ (n = 21) "magic number" cluster is attributed to the presence of a compact clathrate cage isomer. Peptide studies are also presented in which specific and nonspecific solvation is observed for gramicidin S $[GS + 2H]^{2+}(H_2O)_n$ (n = 0 to ~26) and bradykinin $[BK + 2H]^{2+}(H_2O)_n$ (n = 0 to ~73), respectively. However in the case of substance P, $[SP + 3H]^{3+}$, the results unambiguously demonstrate that a compact dehydrated conformer population (resulting from the evaporative ESI process) can be

kinetically trapped on the time scale of several milliseconds, even when an extended coil conformation is energetically favorable in the gas phase.

REFERENCES

(1) Ruotolo, B. T.; Gillig, K. J.; Woods, A. S.; Egan, T. F.; Ugarov, M.; Schultz, J. A.; Russell, D. H. Analysis of Phosphorylated Peptides by Ion Mobility-Mass Spectrometry. *Anal. Chem.*, **2004**, *76*, 6727.

(2) Woods, A. S.; Ugarov, M.; Egan, T.; Koomen, J.; Gillig, K. J.; Fuhrer, K.; Gonin, M.; Schultz, J. A. Lipid/Peptide/Nucleotide Separation with MALDI-Ion Mobility-TOF MS. *Anal. Chem.*, **2004**, *76*, 2187.

(3) McLean, J. A.; Ruotolo, B. T.; Gillig, K. J.; Russell, D. H. Ion Mobility-Mass Spectrometry: A New Paradigm for Proteomics. *Int. J. Mass Spectrom.*, **2005**, *240*, 301.

(4) Flagan, R. C. History of Electrical Aerosol Measurements. *Aeorosol. Sci. and Technol.*, **1998**, *28*, 301.

(5) Knutson, E. O.; Whitby, K. T. Aerosol Classification by Electric Mobility: Apparatus, Theory and Applications. *J. Aerosol. Sci.*, **1975**, *6*, 443.

(6) von Helden, G.; Hsu, M.-T.; Kemper, P. R.; Bowers, M. T. Structure of Carbon Cluster Ions from 3 to 60 Atoms: Linears to Rings to Fullerenes. *J. Chem. Phys.*, **1991**, *95*, 3835.

(7) von Helden, G.; Kemper, P. R.; Gotts, N. G.; Bowers, M. T. Isomers of Small Carbon Cluster Anions: Linear Chains with up to 20 Atoms. *Science*, **1993**, *259*, 1300.

(8) Shvartsburg, A. A.; Jarrold, M. F. Transition from Covalent to Metallic Behavious in Group-14 Clusters. *Chem. Phys. Lett.*, **2000**, *317*, 615.

(9) Fernandez-Lima, F. A.; Becker, C.; Gillig, K.; Russell, W. K.; Nascimento, M. A. C.; Russell, D. H. Experimental and Theoretical Studies of $(CsI)_nCs+$ Cluster Ions Produced by 355 nm Laser Desorption Ionization. *J. Phys. Chem. A*, **2008**, *112*, 11061.

(10) Cottingham, K. Ion Mobility Spectrometry Rediscovered. *Anal. Chem.*, **2003**, *75*, 435A.

(11) Eiceman, G. A.; Stone, J. A. New Uses of Previously Unheralded Analytical Instruments. *Anal. Chem.*, **2004**, 390A.

(12) Verbeck, G. F.; Gillig, K. J.; Russell, D. H. Variable-Temperature Ion Mobility Time-of-Flight Mass Spectrometry Studies of Electronic Isomers of Kr^{2+} and CH_3OH^{*+} Radical Cations. *Eur. J. Mass Spectrom.*, **2003**, *9*, 579.

(13) May, J.; Russell, D. A Mass-Selective Variable-Temperature Drift Tube Ion Mobility-Mass Spectrometer for Temperature Dependent Ion Mobility Studies. *J. Am. Soc. Mass Spectrom.*, **2011**, *22*, 1134.

(14) May, J. C.; Russell, D. H. In *Ion Mobility Spectrometry-Mass Spectrometry*; Wilkins, C. L., Trimpin, S., Eds.; CRC Press: Boca Raton, FL, 2011, p 137.

(15) May, J. C. Development of a Cryogenic Drift Cell Spectrometer and Methods for Improving the Analytical Figures of Merit for Ion Mobility-Mass Spectrometry Analysis. *Dissertation*, **2009**, *Texas A&M University, College Station*.

(16) Becker, C.; Fernandez-Lima, F. A.; Russell, D. H. Ion Mobility-Mass Spectrometry: A Tool for Characterizing the Petroleome. *Spectros.*, **2009**, *24*, 38.

(17) Fernandez-Lima, F. A.; Becker, C.; McKenna, A. M.; Rodgers, R. P.; Marshall, A. G.; Russell, D. H. Petroleum Crude Oil Characterization by IMS-MS and FTICR MS. *Anal. Chem.*, **2009**, *81*, 9941.

(18) Fernandez-Lima, F. A.; Blase, R. C.; Russell, D. H. A Study of Ion-Neutral Collision Cross-Section Values for Low Charge States of Peptides, Proteins, and Peptide/Protein Complexes. *Int. J. Mass Spectrom.*, **2010**, *298,* 111.

(19) Tao, L.; Dahl, D. B.; Pérez, L. M.; Russell, D. H. The Contributions of Molecular Framework to IMS Collision Cross-Sections of Gas-Phase Peptide Ions. *J. Am. Soc. Mass Spectrom.*, **2009**, *20*, 1593.

(20) Valentine, S. J.; Plasencia, M. D.; Liu, X.; Krishnan, M.; Naylor, S.; Udseth, H. R.; Smith, R. D.; Clemmer, D. E. Toward Plasma Proteome Profiling with Ion Mobility-Mass Spectrometry. *J. Prot. Res.*, **2006**, *5*, 2977.

(21) Hoaglund, C. S.; Valentine, S. J.; Clemmer, D. E. An Ion Trap Interface for ESI-Ion Mobility Experiments. *Anal. Chem.*, **1997**, *69*, 4156.

(22) Zaia, J. Mass Spectrometry and the Emerging Field of Glycomics. *Chem. and Biol.*, **2008**, *15*, 881.

(23) Dwivedi, P.; Wu, P.; Klopsch, S. J.; Puzon, G. F.; Xun, L.; Hill, H. H., Jr. Metabolic Profiling by Ion Mobility Mass Spectrometry (IMMS). *Metabol.*, **2007**, *In Press*.

(24) Dugourd, P.; Hudgins, R. R.; Clemmer, D. E.; Jarrold, M. F. High-Resolution Ion Mobility Measurements. *Rev. Sci. Instrum.*, **1997**, *68*, 1122.

(25) Wu, C.; Siems, W. F.; Asbury, G. R.; Hill, H. H., Jr. Electrospray Ionization High-Resolution Ion Mobility Spectrometry-Mass Spectrometry. *Anal. Chem.*, **1998**, *70*, 4929.

(26) Kemper, P. R.; Dupuis, N. F.; Bowers, M. T. A New, Higher Resolution, Ion Mobility Mass Spectrometer. *Int. J. Mass Spectrom.*, **2009**, *287*, 46.

(27) Rokushika, S.; Hatano, H.; Baim, M. A.; Hill, H. H. Resolution Measurement for Ion Mobility Spectrometry. *Anal. Chem.*, **1985**, *57*, 1902.

(28) Merenbloom, S. I.; Glaskin, R. S.; Henson, Z. B.; Clemmer, D. E. High-Resolution Ion Cyclotron Mobility Spectrometry. *Anal. Chem.*, **2009**, *81*, 1482.

(29) Mason, E. A.; McDaniel, E. W. Transport Properties of Ions in Gases. *John Wiley & Sons, Inc.,* New York, NY, **1988**.

(30) Wyttenbach, T.; von Helden, G.; Bowers, M. T. Gas-Phase Conformation of Biological Molecules: Bradykinin. *J. Am. Chem. Soc*, **1996**, *118*, 8355.

(31) McDaniel, E. W.; Viehland, L. A. The Transport of Slow Ions in Gasses: Experiment, Theory, and Applications. *Phys. Rep.*, **1984**, *110*, 333.

(32) Ruotolo, B. T.; McLean, J. A.; Gillig, K. J.; Russell, D. H. The Influence and Utility of Varying Field Strength for the Separation of Tryptic Peptides by Ion Mobility-Mass Spectrometry. *J. Am. Soc. Mass Spectrom.*, **2005**, *16*, 158.

(33) Shvartsburg, A. A. Differential Ion Mobility Spectrometry, Nonlinear Ion Transport and Fundamentals of FAIMS. *CRC Press,* Boca Raton, FL, **2009**.

(34) Revercomb, H. E.; Mason, E. A. Theory of Plasma Chromatrography/Gaseous Electrophoresis - A Review. *Anal. Chem.*, **1975**, *47*, 970.

(35) Viehland, L. A.; Mason, E. A. Gaseous Ion Mobility in Electric Fields of Arbitrary Strength. *Ann. Phys.*, **1975**, *91*, 499.

(36) Ruotolo, B. T.; Benesch, J. L. P.; Sandercock, A. M.; Hyung, S.-J.; Robinson, C. V. Ion Mobility-Mass Spectrometry Analysis of Large Protein Complexes. *Nat. Protocols*, **2008**, *3*, 1139.

(37) Morsa, D.; Gabelica, V. R.; De Pauw, E. Effective Temperature of Ions in Traveling Wave Ion Mobility Spectrometry. *Anal. Chem.*, **2011**, *83*, 5775.

(38) Giles, K.; Wildgoose, J. L.; Langridge, D. J.; Campuzano, I. A Method for Direct Measurement of Ion Mobilities using a Travelling Wave Ion Guide. *Int. J. Mass Spectrom.*, **2010**, *298*, 10.

(39) Guo, Y.; Wang, J.; Javahery, G.; Thomson, B. A.; Siu, K. W. M. Ion Mobility Spectrometer with Radial Collisional Focusing. *Anal. Chem.*, **2004**, *77*, 266.

(40) Bluhm, B. K.; Gillig, K. J.; Russell, D. H. Development of a Fourier-Transform Ion Cyclotron Resonance Mass Spectrometer-Ion Mobility Spectrometer. *Rev.Sci. Instrum.*, **2000**, *71*, 4078.

(41) Gillig, K. J.; Russell, D. H. The Periodic Focusing Ion Mobility Spectrometer, **2001**, *US Patent 0032930 A1*.

(42) Gillig, K. J.; Ruotolo, B. T.; Stone, E. G.; Russell, D. H. An Electrostatic Focusing Ion Guide for Ion Mobility-Mass Spectrometry. *Int. J. Mass Spectrom.*, **2004**, *239*, 43.

(43) Blase, R. C.; Silveira, J. A.; Gillig, K. J.; Gamage, C. M.; Russell, D. H. Increased Ion Transmission in IMS: A High Resolution, Periodic-Focusing DC Ion Guide Ion Mobility Spectrometer. *Int. J. Mass Spectrom.*, **2011**, *301*, 166.

(44) Gillig, K. J.; Russell, D. H. Periodic Field Focusing Ion Mobility Spectrometer. **2003**, *US Patent 6639213*.

(45) McLean, J. A.; Russell, D. H. Multiplex Data Acquisition Based on Analyte Dispersion in Two Dimensions: More Signal More of the Time. *Int. J. Ion Mobility Spectrom.*, **2005**, *8*, 66.

(46) McLean, J. A.; Russell, D. H.; Egan, T. F.; Ugarov, M. V.; Schultz, J. A. Multiplex Data Acquisition Modes for Ion Mobility-Mass Spectrometry. **2009**, *US Patent 7745780*.

(47) Guan, S.; Marshall, A. G. Stacked-Ring Electrostatic Ion Guide. *J. Am. Soc. Mass Spectrom.*, **1996**, *7*, 101.

(48) Silveira, J. A.; Gamage, C. M.; May, J. C.; Russell, D. H. Conference Proceedings from *ASMS,* Philadelphia, PA, **2010**.

(49) March, R. E.; Todd, J. F. J. Quadrupole Ion Trap Mass Spectrometry*, Second Edition*, *John Wiley & Sons, Inc.,* Malden, MA*,* **2005**.

(50) Silveira, J. A.; Gamage, C. M.; Blase, R. C.; Russell, D. H. Gas-Phase Ion Dynamics in a Periodic-Focusing DC Ion Guide. *Int. J. of Mass Spectrom.*, **2010**, *296*, 36.

(51) Gerlich, D. Inhomogeneous RF Fields: A Versatile Tool for the Study of Processes with Slow Ions*., John Wiley & Sons, Inc.*, Malden, MA, **1992**.

(52) Tolmachev, A. V.; Kim, T.; Udseth, H. R.; Smith, R. D.; Bailey, T. H.; Futrell, J. H. Simulation-Based Optimization of the Electrodynamic Ion Funnel for High Sensitivity Electrospray Ionization Mass Spectrometry. *Int. J. Mass Spectrom.*, **2000**, *203*, 31.

(53) Blase, R. C.; Silveira, J. A.; Gillig, K. J.; Gamage, C. M.; Russell, D. H. Increased Ion Transmission in IMS: A High Resolution, Periodic-FocusingDC Ion Guide Ion Mobility Spectrometer. *Int. J. Mass Spectrom.*, **2010**, *301*, 166.

(54) Danell, R. M.; Danell, A. S.; Glish, G. L.; Vachet, R. W. The Use of Static Pressures of Heavy Gases Within a Quadrupole Ion Trap. *J. Am. Soc. Mass Spectrom.*, **2003**, *14*, 1099.

(55) Giles, K.; Pringle, S. D.; Worthington, K. R.; Little, D.; Wildgoose, J. L.; Bateman, R. H. Applications of a Travelling Wave-Based Radio-Frequency-Only Stacked Ring Ion Guide. *Rapid Commun. Mass Spectrom.*, **2004**, *18*, 2401.

(56) Gamage, C. M.; Silveira, J. A.; Blase, R. C.; Russell, D. H. Gas-Phase Ion Dynamics in a Periodic-Focusing DC Ion Guide (Part II): Discrete Transport Modes. *Int. J. Mass Spectrom.*, **2011**, *303*, 154.

(57) Bush, M. F.; Hall, Z.; Giles, K.; Hoyes, J.; Robinson, C. V.; Ruotolo, B. T. Collision Cross Sections of Proteins and Their Complexes: A Calibration Framework and Database for Gas-Phase Structural Biology. *Anal. Chem.*, **2010**, *82*, 9557.

(58) Jeon, J.; Blase, R. C.; Gamage, C. M.; Russell, D. H. Conference Proceedings from *ASMS,* Denver, CO, **2011**.

(59) Brooijmans, N.; Sharp, K. A.; Kuntz, I. D. Stability of Macromolecular Complexes. *Proteins Struct. Funct. Bioinformat.*, **2002**, *48*, 645.

(60) Sundarapandian, S.; May, J. C.; McLean, J. A. Dual Source Ion Mobility-Mass Spectrometer for Direct Comparison of Electrospray Ionization and MALDI Collision Cross Section Measurements. *Anal. Chem.*, **2010**, *82*, 3247.

(61) Shvartsburg, A. A.; Li, F.; Tang, K.; Smith, R. D. High-Resolution Field Asymmetric Waveform Ion Mobility Spectrometry Using New Planar Geometry Analyzers. *Anal. Chem.*, **2006**, *78*, 3706.

(62) Pierson, N. A.; Valentine, S. J.; Clemmer, D. E. Evidence for a Quasi-Equilibrium Distribution of States for Bradykinin $[M + 3H]^{3+}$ Ions in the Gas Phase. *J. Phys. Chem. B*, **2010**, *114*, 7777.

(63) Cross Section Datatbase. http://www.indiana.edu/~clemmer/Research/Cross%20Section%20Database/cs_database.php (accessed October 12, 2013).

(64) Baker, E. S.; Clowers, B. H.; Li, F.; Tang, K.; Tolmachev, A. V.; Prior, D. C.; Belov, M. E.; Smith, R. D. Ion Mobility Spectrometry–Mass Spectrometry Performance Using Electrodynamic Ion Funnels and Elevated Drift Gas Pressures. *J. Am. Soc. Mass Spectrom.*, **2007**, *18*, 1176.

(65) Poully, J.-C.; Grégoire, G.; Ballivian, R.; Dugourd, P.; Schermann, J. P. Coupling Infrared Multiphoton Dissociation Spectroscopy, Mass-Spectrometry and Ion Mobility Spectrometry for the Determination of Structures of Angiotensin II Cations. *Vib. Spectros.*, **2011**, *56*, 105.

(66) Florance, H. V.; Stopford, A. P.; Kalapothakis, J. M.; McCullough, B. J.; Bretherick, A.; Barran, P. E. Evidence for Small Alpha-Helices in the Gas Phase: A Case Study using Melittin from Honey Bee Venom. *Analyst*, **2011**, *136*, 3446.

(67) Fernandez-Lima, F. A.; Becker, C.; Gillig, K. J.; Russell, W. K.; Tichy, S. E.; Russell, D. H. Ion Mobility-Mass Spectrometer Interface for Collisional Activation of Mobility Separated Ions. *Anal. Chem.*, **2009**, *81*, 618.

(68) Pierson, N. A.; Chen, L.; Valentine, S. J.; Russell, D. H.; Clemmer, D. E. Number of Solution States of Bradykinin from Ion Mobility and Mass Spectrometry Measurements. *J. Am. Chem. Soc.*, **2011**, *133*, 13810.

(69) Wyttenbach, T.; von Helden, G.; Batka, J.; Carlat, D.; Bowers, M. Effect of the Long-Range Potential on Ion Mobility Measurements. *J. Am. Soc. Mass Spectrom.*, **1997**, *8*, 275.

(70) Wyttenbach, T.; Bowers, M. T. Structural Stability from Solution to the Gas Phase: Native Solution Structure of Ubiquitin Survives Analysis in a Solvent-Free Ion Mobility–Mass Spectrometry Environment. *J. Phys. Chem. B*, **2011**, *115*, 12266.

(71) Bernstein, S. L.; Wyttenbach, T.; Baumketner, A.; Shea, J.-E.; Bitan, G.; Teplow, D. B.; Bowers, M. T. Amyloid β-Protein: Monomer Structure and Early

Aggregation States of Aβ42 and Its Pro19 Alloform. *J. Am. Chem. Soc.*, **2005**, *127*, 2075.

(72) Ruotolo, B. T.; Giles, K.; Campuzano, I.; Sandercock, A. M.; Bateman, R. H.; Robinson, C. V. Evidence for Macromolecular Protein Rings in the Absence of Bulk Water. *Science*, **2005**, *310*, 1658.

(73) Ruotolo, B. T.; Robinson, C. V. Aspects of Native Proteins are Retained in Vacuum. *Curr. Opin. Chem. Biol.*, **2006**, *10*, 402.

(74) Breuker, K.; Brüschweiler, S.; Tollinger, M. Electrostatic Stabilization of a Native Protein Structure in the Gas Phase. *Angew. Chem. Int. Ed.*, **2011**, *50*, 873.

(75) van der Spoel, D.; Marklund, E. G.; Larsson, D. S. D.; Caleman, C. Proteins, Lipids, and Water in the Gas Phase. *Macromol. Biosci.*, **2011**, *11*, 50.

(76) Hilton, G. R.; Benesch, J. L. P. Two Decades of Studying Non-Covalent Biomolecular Assemblies by Means of Electrospray Ionization Mass Spectrometry. *J. R. Soc. Interface*, **2012**, *9*, 801.

(77) Hall, Z.; Politis, A.; Bush, M. F.; Smith, L. J.; Robinson, C. V. Charge-State Dependent Compaction and Dissociation of Protein Complexes: Insights from Ion Mobility and Molecular Dynamics. *J. Am. Chem. Soc.*, **2012**, *134*, 3429.

(78) Jarrold, M. F. Unfolding, Refolding, and Hydration of Proteins in the Gas Phase. *Acc. Chem. Res.*, **1999**, *32*, 360.

(79) Liu, D.; Wyttenbach, T.; Barran, P. E.; Bowers, M. T. Sequential Hydration of Small Protonated Peptides. *J. Am. Chem. Soc.*, **2003**, *125*, 8458.

(80) Kohtani, M.; Breaux, G. A.; Jarrold, M. F. Water Molecule Adsorption on Protonated Dipeptides. *J. Am. Chem. Soc.*, **2004**, *126*, 1206.

(81) Liu, D.; Wyttenbach, T.; Bowers, M. T. Hydration of Mononucleotides. *J. Am. Chem. Soc.*, **2006**, *128*, 15155.

(82) Wyttenbach, T.; Bowers, M. T. Hydration of Biomolecules. *Chem. Phys. Lett.*, **2009**, *480*, 1.

(83) Rodriguez-Cruz, S. E.; Klassen, J. S.; Williams, E. R. Hydration of Gas-Phase Gramicidin S $[M + 2H]^{2+}$ Ions Formed by Electrospray: The Transition From Solution to Gas-Phase Structure. *J. Am. Soc. Mass Spectrom.*, **1997**, *8*, 565.

(84) Lee, S.-W.; Freivogel, P.; Schindler, T.; Beauchamp, J. L. Freeze-Dried Biomolecules: FT-ICR Studies of the Specific Solvation of Functional Groups and Clathrate Formation Observed by the Slow Evaporation of Water from Hydrated Peptides and Model Compounds in the Gas Phase. *J. Am. Chem. Soc.*, **1998**, *120*, 11758.

(85) Bush, M. F.; Prell, J. S.; Saykally, R. J.; Williams, E. R. One Water Molecule Stabilizes the Cationized Arginine Zwitterion. *J. Am. Chem. Soc.*, **2007**, *129*, 13544.

(86) Muraoka, A.; Inokuchi, Y.; Hammer, N. I.; Shin, J.-W.; Johnson, M. A.; Nagata, T. Structural Evolution of the $[(CO_2)_n(H_2O)]^-$ Cluster Anions: Quantifying the Effect of Hydration on the Excess Charge Accommodation Motif. *J. Phys. Chem. A*, **2009**, *113*, 8942.

(87) Prell, J. S.; Chang, T. M.; O'Brien, J. T.; Williams, E. R. Hydration Isomers of Protonated Phenylalanine and Derivatives: Relative Stabilities from Infrared Photodissociation. *J. Am. Chem. Soc.*, **2010**, *132*, 7811.

(88) Prell, J. S.; Correra, T. C.; Chang, T. M.; Biles, J. A.; Williams, E. R. Entropy Drives an Attached Water Molecule from the C- to N-Terminus on Protonated Proline. *J. Am. Chem. Soc.*, **2010**, *132*, 14733.

(89) Breen, K. J.; DeBlase, A. F.; Guasco, T. L.; Voora, V. K.; Jordan, K. D.; Nagata, T.; Johnson, M. A. Bottom-Up View of Water Network-Mediated CO_2 Reduction Using Cryogenic Cluster Ion Spectroscopy and Direct Dynamics Simulations. *J. Phys. Chem. A*, **2011**, *116*, 903.

(90) Prell, J. S.; O'Brien, J. T.; Williams, E. R. Structural and Electric Field Effects of Ions in Aqueous Nanodrops. *J. Am. Chem. Soc.*, **2011**, *133*, 4810.

(91) Nagornova, N. S.; Rizzo, T. R.; Boyarkin, O. V. Interplay of Intra- and Intermolecular H-Bonding in a Progressively Solvated Macrocyclic Peptide. *Science*, **2012**, *336*, 320.

(92) Demireva, M.; O'Brien, J. T.; Williams, E. R. Water-Induced Folding of 1,7-Diammoniumheptane. *J. Am. Chem. Soc.*, **2012**, *134*, 11216.

(93) Zamith, S.; Labastie, P.; L'Hermite, J.-M. Fragmentation Cross Sections of Protonated Water Clusters. *J. Chem. Phys.*, **2012**, *136*, 214301.

(94) Gidden, J.; Bushnell, J. E.; Bowers, M. T. Gas-Phase Conformations and Folding Energetics of Oligonucleotides: dTG- and dGT. *J. Am. Chem. Soc.*, **2001**, *123*, 5610.

(95) Silveira, J. A.; Jeon, J.; Gamage, C. M.; Pai, P.-J.; Fort, K. L.; Russell, D. H. Damping Factor Links Periodic Focusing and Uniform Field Ion Mobility for Accurate Determination of Collision Cross Sections. *Anal. Chem.*, **2012**, *84*, 2818.

(96) Silveira, J. A.; Gamage, C. M.; Russell, D. H. In *Conference Proceedings from ASMS,* Denver, CO, **2011**.

(97) Sun, W. J. Development of a MALDI Ion Mobility Surface Induced Dissociation Time-of-Flight Mass Spectrometer with Novel Collision Source Configurations for High Throughput Peptide Sequencing, *Dissertation*, **2007**, *Texas A&M University, College Station*.

(98) Searcy, J. Q.; Fenn, J. B. Clustering of Water on Hydrated Protons in a Supersonic Free Jet Expansion. *J. Chem. Phys.*, **1974**, *61*, 5282.

(99) Shi, Z.; Ford, J. V.; Wei, S.; Castleman, A. W. Water Clusters: Contributions of Binding Energy and Entropy to Stability. *J. Chem. Phys.*, **1993**, *1993*, 8009.

(100) Miyazaki, M.; Fujii, A.; Ebata, T.; Mikami, N. Infrared Spectroscopic Evidence for Protonated Water Clusters Forming Nanoscale Cages. *Science*, **2004**, *304*, 1134.

(101) Shin, J.-W.; Hammer, N. I.; Diken, E. G.; Johnson, M. A.; Walters, R. S.; Jaeger, T. D.; Duncan, M. A.; Christie, R. A.; Jordan, K. D. Infrared Signature of Structures Associated with the $H^+(H_2O)_n$ (n = 6 to 27) Clusters. *Science*, **2004**, *304*, 1137.

(102) Lau, Y. K.; Ikuta, S.; Kebarle, P. Thermodynamics and Kinetics of the Gas-Phase Reactions $H3O^+(H_2O)_{n-1}{}^+$ water = $H_3O^+(H_2O)_n$. *J. Am. Chem. Soc.*, **1982**, *104*, 1462.

(103) Jiang, J.-C.; Wang, Y.-S.; Chang, H.-C.; Lin, S. H.; Lee, Y. T.; Niedner-Schatteburg, G.; Chang, H.-C. Infrared Spectra of $H^+(H_2O)_{5-8}$ Clusters: Evidence for Symmetric Proton Hydration. *J. Am. Chem. Soc.*, **2000**, *122*, 1398.

(104) König, S.; Fales, H. M. Formation and Decomposition of Water Clusters as Observed in a Triple Quadrupole Mass Spectrometer. *J. Am. Soc. Mass Spectrom.*, **1998**, *9*, 814.

(105) Singh, N. J.; Park, M.; Min, S. K.; Suh, S. B.; Kim, K. S. Magic and Antimagic Protonated Water Clusters: Exotic Structures with Unusual Dynamic Effects. *Angew. Chem. Int. Ed.*, **2006**, *45*, 3795.

(106) Sterling, H. J.; Cassou, C. A.; Susa, A. C.; Williams, E. R. Electrothermal Supercharging of Proteins in Native Electrospray Ionization. *Anal. Chem.*, **2012**, *84*, 3795.

(107) Liu, K.; Loeser, J. G.; Elrod, M. J.; Host, B. C.; Rzepiela, J. A.; Pugliano, N.; Saykally, R. J. Dynamics of Structural Rearrangements in the Water Trimer. *J. Am. Chem. Soc.*, **1994**, *116*, 3507.

(108) Cheng, H.-P. Water Clusters: Fascinating Hydrogen-Bonding Networks, Solvation Shell Structures, and Proton Motion. *J. Phys. Chem. A*, **1998**, *102*, 6201.

(109) Kawai, Y.; Yamaguchi, S.; Okada, Y.; Takeuchi, K.; Yamauchi, Y.; Ozawa, S.; Nakai, H. Reactions of Protonated Water Clusters $H^+(H_2O)_n$ (n=1–6) with Dimethylsulfoxide in a Guided Ion Beam Apparatus. *Chem. Phys. Lett.*, **2003**, *377*, 69.

(110) Schroeder, O. E.; Andriole, E. J.; Carver, K. L.; Colyer, K. E.; Poutsma, J. C. Proton Affinity of Lysine Homologues from the Extended Kinetic Method. *J. Phys. Chem. A*, **2003**, *108*, 326.

(111) Wròblewski, T.; Ziemczonek, L.; Karwasz, G. Proton Transfer Reactions for Ionized Water Clusters. *Czech. J. Phys.*, **2004**, *54*, C747.

(112) de Grotthuss, C. J. T. Sur la décomposition de l'eau et des corps qu'elle tient en dissolution à l'aide de l'électricité galvanique. *Ann. Chim.*, **1806**, *LVIII*, 54.

(113) Marx, D.; Tuckerman, M. E.; Hutter, J.; Parrinello, M. The Nature of the Hydrated Excess Proton in Water. *Nature*, **1999**, *397*, 601.

(114) Garand, E.; Kamrath, M. Z.; Jordan, P. A.; Wolk, A. B.; Leavitt, C. M.; McCoy, A. B.; Miller, S. J.; Johnson, M. A. Determination of Noncovalent Docking by Infrared Spectroscopy of Cold Gas-Phase Complexes. *Science*, **2012**, *335*, 694.

(115) Breuker, K.; McLafferty, F. W. Stepwise Evolution of Protein Native Structure with Electrospray into the Gas Phase, 10^{-12} to 10^{2} s. *Proc. Natl. Acad. Sci. U.S.A.*, **2008**, *105*, 18145.

(116) Skinner, O.; McLafferty, F.; Breuker, K. How Ubiquitin Unfolds after Transfer into the Gas Phase. *J. Am. Soc. Mass Spectrom.*, **2012**, *23*, 1011.

(117) Hall, Z.; Robinson, C. Do Charge State Signatures Guarantee Protein Conformations? *J. Am. Soc. Mass Spectrom.*, **2012**, *23*, 1161.

(118) Heuvel, R. H. H. v. d.; Heck, A. J. R. Native Protein Mass Spectrometry: from Intact Oligomers to Functional Machineries. *Curr. Opin. Chem. Biol.*, **2004**, *8*, 519.

(119) Barrera, N. P.; Di Bartolo, N.; Booth, P. J.; Robinson, C. V. Micelles Protect Membrane Complexes from Solution to Vacuum. *Science*, **2008**, *321*, 243.

(120) Papadopoulos, G.; Svendsen, A.; Boyarkin, O.; Rizzo, T. Conformational Distribution of Bradykinin $[BK + 2\,H]^{2+}$ Revealed by Cold Ion Spectroscopy Coupled with FAIMS. *J. Am. Soc. Mass Spectrom.*, **2012**, *23*, 1173.

(121) Deng, Z.; Thontasen, N.; Malinowski, N.; Rinke, G.; Harnau, L.; Rauschenbach, S.; Kern, K. A Close Look at Proteins: Submolecular Resolution of Two- and Three-Dimensionally Folded Cytochrome C at Surfaces. *Nano Lett.*, **2012**, *12*, 2452.

(122) Dole, M.; Mack, M. M.; Hines, R. L.; Mobley, R. C.; Ferguson, L. D.; Alice, M. B. Molecular Beams of Macroions *J. Chem. Phys.*, **1968**, *49*, 2240.

(123) Mack, L. L.; Kralik, P.; Rheude, A.; Dole, M. Molecular Beams of Macroions. II *J. Chem. Phys.*, **1970**, *52*, 4977.

(124) Nguyen, S.; Fenn, J. B. Gas-phase Ions of Solute Species from Charged Droplets of Solutions. *Proc. Natl. Acad. Sci. U.S.A.*, **2007**, *104*, 1111.

(125) Iribarne, J. V.; Thompson, B. A. On the Evaporation of Small Ions from Charged Droplets. *J. Chem. Phys.*, **1976**, *64*, 2287.

(126) Consta, S.; Malevanets, A. Manifestations of Charge Induced Instability in Droplets Effected by Charged Macromolecules. *Phys. Rev. Lett.*, **2012**, *109*, 148301.

(127) Konermann, L.; Ahadi, E.; Rodriguez, A. D.; Vahidi, S. Unraveling the Mechanism of Electrospray Ionization. *Anal. Chem.*, **2012**, *85*, 2.

(128) Ahadi, E.; Konermann, L. Ejection of Solvated Ions from Electrosprayed Methanol/Water Nanodroplets Studied by Molecular Dynamics Simulations. *J. Am. Chem. Soc.*, **2011**, *133*, 9354.

(129) Silveira, J. A.; Servage, K. A.; Gamage, C. M.; Russell, D. H. Cryogenic Ion Mobility-Mass Spectrometry Captures Hydrated Ions Produced During Electrospray Ionization. *J. Phys. Chem. A*, **2013**, *117*, 953.

(130) Wyttenbach, T.; Liu, D.; Bowers, M. T. Hydration of Small Peptides. *Int. J. Mass Spectrom.*, **2005**, *240*, 221.

(131) Augé, S.; Bersch, B.; Tropis, M.; Milon, A. Characterization of Substance P–Membrane Interaction by Transferred Nuclear Overhauser Effect. *Biopolymers*, **2000**, *54*, 297.

(132) Gayen, A.; Goswami, S. K.; Mukhopadhyay, C. NMR Evidence of GM1-Induced Conformational Change of Substance P using Isotropic Bicelles. *Biochim. Biophys. Acta*, **2011**, *1808*, 127.

(133) Gill, A. C.; Jennings, K. R.; Wyttenbach, T.; Bowers, M. T. Conformations of Biopolymers in the Gas Ghase: a New Mass Spectrometric Method. *Int. J. Mass Spectrom.*, **2000**, *195*, 685.

(134) Addario, V.; Guo, Y.; Chu, I. K.; Ling, Y.; Ruggerio, G.; Rodriquez, C. F.; Hopkinson, A. C.; Siu, K. W. M. ProtonAaffinities of Methyl Esters of N-Acetylated Amino Acids. *Int. J. Mass Spectrom.*, **2002**, *219*, 101.

(135) Mihalca, R.; Kleinnijenhuis, A.; McDonnell, L.; Heck, A. R.; Heeren, R. A. Electron Capture Dissociation at Low Temperatures Reveals Selective Dissociations. *J. Am. Soc. Mass Spectrom.*, **2004**, *15*, 1869.

APPENDIX

Figure 33. Photographs of the initial (top) and final (bottom) cryogenic IM-MS instrument apparatus.

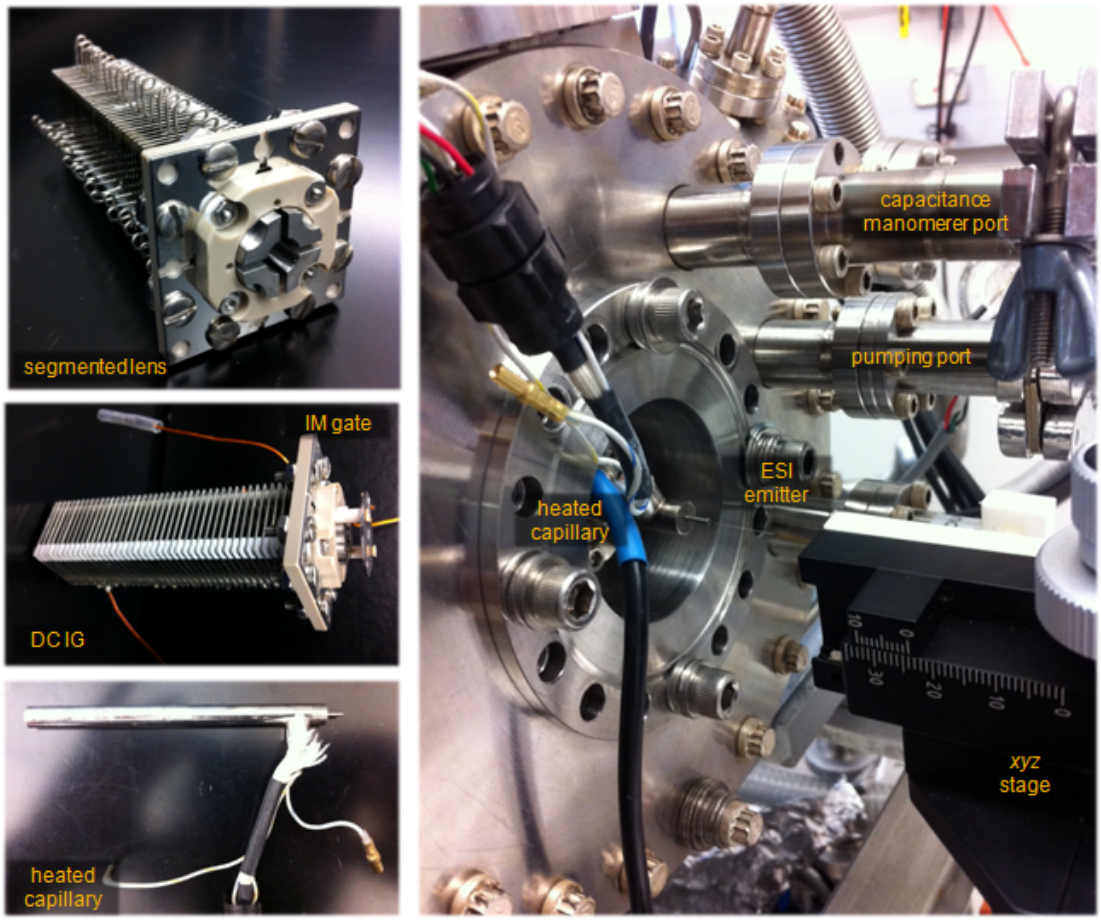

Figure 34. Photographs of the ESI source and DC IG regions. Note that the segmented lens was designed to replace the gate lens described in Table 4.

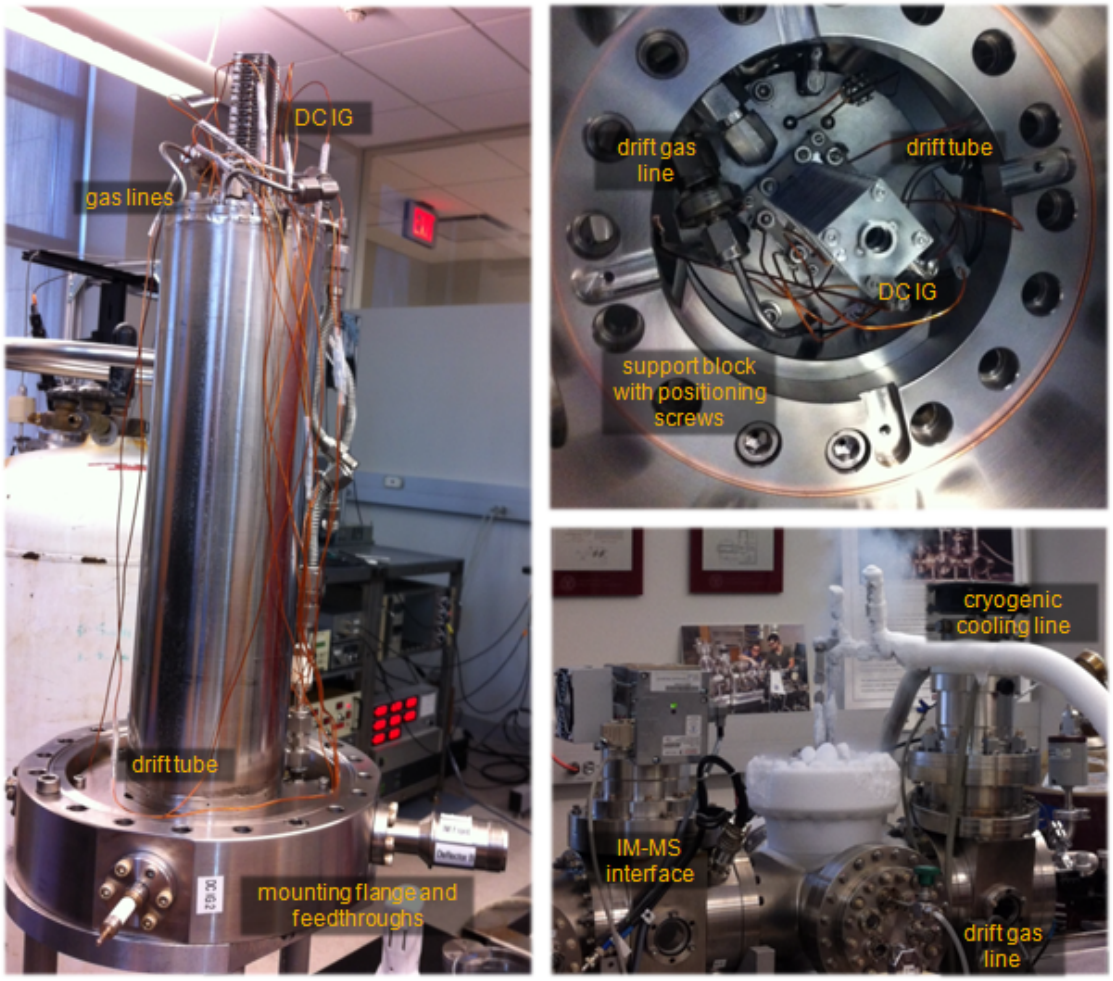

Figure 35. Photographs of the IM drift tube region.

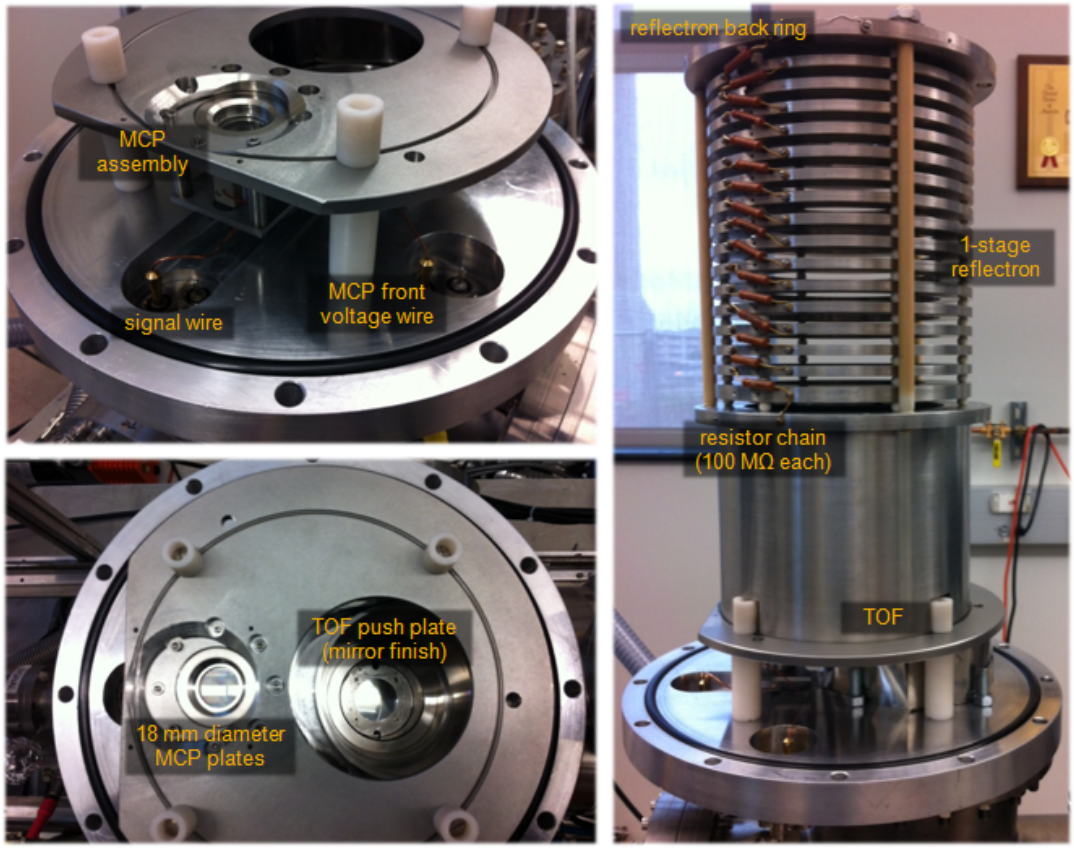

Figure 36. Photographs of the reflectron TOF mass analyzer.